Monolithically integrated coherent comb de-multiplexer using facetless semiconductor ring lasers

Mohamad Dernaika
PhD

Thesis submitted for the degree of Doctor of Philosophy

NATIONAL UNIVERSITY OF IRELAND, CORK

School of Engineering

Department of Electrical and Electronic Engineering

2019

Head of Department: Prof. Liam Marnane

Supervisor: Prof. Frank H. Peters

Research supported by Science Foundation Ireland (SFI)

Contents

Abstract . . . iv
Acknowledgements . . . v
List of Publications . . . vi
List of Acronyms . . . x

1 Introduction **1**
1.1 WDM . . . 1
1.2 Coherent optical comb and Co-WDM . . . 2
1.3 Photonic integrated circuit (PIC) . . . 3
1.4 Coherent Comb de-multiplexing . . . 4
1.5 Integrated laser filters (ILF) . . . 7
1.6 Thesis structure . . . 8

2 Fabrication **10**
2.1 Material . . . 10
2.2 Mask design . . . 12
2.3 Standard Process . . . 13
2.3.1 Ridge Lithography . . . 14
2.3.2 Deep lithography . . . 17
2.3.3 Oxide opening lithography . . . 23
2.3.4 Metal Lift off lithography . . . 24
2.4 Metal first Process . . . 27

3 Semiconductor lasers **29**
3.1 Semiconductor lasers . . . 29
3.1.1 Slotted Fabry Perot lasers . . . 30
3.1.1.1 SFP for integration . . . 32
3.1.2 Pit lasers . . . 34
3.1.2.1 Single facet pit laser . . . 43
3.1.3 V-notch . . . 51
3.1.3.1 single facet V-notch lasers . . . 55
3.1.4 Comb de-multiplexing and linear cavities Q-factor . . . 58
3.1.4.1 Filtering performance analysis and Q-factor . . . 62

4 Active rings **64**
4.1 Ring resonators . . . 64
4.1.1 Bends . . . 65
4.1.2 Ring couplers . . . 66
4.1.2.1 MMI couplers . . . 67
4.1.2.2 Half wave couplers (HWC) . . . 68
4.1.2.3 Directional couplers . . . 70
4.1.3 Coherent comb filtering and selective amplification via injection locking . . . 77

5 Conclusion and Future Work **82**
5.1 Future Work . . . 83

A Mach Zehnder interfermeter laser **85**

B Single mode laser based on coupled cavities of an active ring laser and Fabry Perot **91**

I, Mohamad Dernaika, certify that this thesis is my own work and has not been submitted for another degree at University College Cork or elsewhere.

Mohamad Dernaika

Abstract

Due to the growing demand for faster Internet connections and the growth of services requiring high bandwidths, the migration of the networks to higher and higher bit rates is inevitable. The surge in data usage due to real time application in the entertainment, business and medical sector has placed tremendous pressure on the current infrastructure and its ability to keep up with the constant traffic increase. Wavelength division multiplexing (WDM) systems, which currently dominate long-haul optical transmission links employ guard bands between channels to avoid interference. This leads to inefficient use of the system bandwidth, which is limited by the erbium doped fibre amplifier (EDFA). A solution to this problem is to use coherent WDM (Co-WDM), or called optical orthogonal frequency division multiplexing (OFDM) to increase the bandwidth efficiency. In Co-WDM or optical OFDM, the interference from adjacent orthogonal channels can be eliminated at the receiver end. Therefore, the spacing between adjacent channels can be reduced without using guard bands. Moreover, the series of individual lasers used in WDM networks can be replaced with a single coherent comb source. However, Co-WDM still requires the use of discrete bulky components, such as narrow band filters to operate as a comb demultiplexer, modulators and multiplexer. To justify the potential move from WDM to Co-WDM a significant reduction in cost, size and production time is necessary. The photonic integrated circuit (PIC) offers an attractive solution to integrate all components on a single chip. The vision of the larger research project was to design and fabricate a fully integrated Co-WDM transceiver. The initial demonstration PIC will comprise an integrated coherent comb generator, a comb filter and an integrated electro-absorption modulator (EAM). However, this work mainly focused on the filter aspect of the PIC to demultiplex the narrowly spaced comb lines (<25 GHz). The filter has two functions: to demultiplex the comb lines, and to selectively amplify the individual comb line through injection locking. The filter is designed to be facet-less so that it can be suitable for integration with other devices. The fabrication process of the PIC employs Standard UV lithography and a regrowth-free process to further reduce the time, cost and complexity making it suitable for mass production. The process of optimizing the facet-less lasers in term of fabrication yield, consistency and filtering performance will be presented.

Acknowledgements

First and foremost, I would like to thank God, whose many blessings have made me who I am today. Also, for giving me the strength, knowledge, ability and opportunity to undertake this PhD.

I would like to express my special appreciation and thanks to my supervisor Professor Frank H. Peters.
Prof. Frank I sincerely would like to thank you for all the help and support you provided. I also would like to thank you for allowing me to innovate and for helping me to grow as a researcher and an engineer.

Special thanks to my colleague Dr. Ludovic Caro for the support and friendship, and for sharing with me the pain and suffering when something goes wrong in the clean room. Also, I would like to thank the whole integrated photonics group (IPG) team for the support.

Last but not the least, I would like to thank my parents for supporting me emotionally and for believing in me. My love and gratitude for them can hardly be expressed in words. Also, I would like to thank my sister Ghina for supporting me spiritually throughout writing this thesis and in my life in general, and to my brother Haissam for his support.

I gratefully acknowledge the funding received towards my PhD from Science foundation of Ireland (SFI). And many thanks go to the people of Tyndall National Institute and University College Cork (UCC) for making my PhD a pleasant experience.

List of Publications

Journal Articles

1. **M. Dernaika**, L. Caro, N. P. Kelly, J. K. Alexander, F. Dubois, P. E. Morrissey, and F. H. Peters, "Deeply Etched Inner Cavity Pit Reflector," *IEEE Photonics Journal*, vol. 9, no. 1, pp. 1 - 8, 2017.

2. **M. Dernaika**, L. Caro, N. P. Kelly, and F. H. Peters, "Single Facet Semiconductor Laser with Deep Etched V-notch Reflectors Integrated with an Active Multimode Interference Reflector," *Journal of Modern Optics*, vol. 64, no. 19, pp. 1941 - 1946, 2017.

3. **M. Dernaika**, N. P. Kelly, L. Caro, K. Shortiss and F. H. Peters, "Regrowth-free Single-mode Semiconductor Laser Suitable for Monolithic Integration based on Pits Mirror," *Optical Engineering*, vol. 65, no. 8, 2017.

4. **M. Dernaika**, L. Caro, N. P. Kelly, M. Shayesteh and F. H. Peters, "Tunable L-band semiconductor laser based on Mach-Zehnder interferometer," *Optics Communications*, vol. 402, pp. 56 - 59, 2017.

5. **M. Dernaika**, N. P. Kelly, L. Caro and F. H. Peters, "Single mode semiconductor laser based on coupled cavities of an activering laser and Fabry Perot," *IET Optoelectronics*, vol. 12, no. 3, pp. 118 - 121, 2017.

6. K. Shortiss, **M. Dernaika**, L. Caro, M. Seifikar and F. H. Peters, "Inverse Scattering Method Design of Regrowth-free Single-mode Semiconductor Lasers Using Pit Perturbations for Monolithic Integration," *IEEE Photonics Journal*, 2018.

7. L. Caro, **M. Dernaika**, N. P. Kelly, P. E. Morrissey, J. K. Alexander, and F. H. Peters, "An Integration-Friendly Regrowth-Free Tunable Laser," *IEEE Photonics Technology Letters*, vol. 30, pp. 270 - 272, 2018.

8. N. P. Kelly, **M. Dernaika**, L. Caro, P. E. Morrissey, A. H. Perrott, J. K. Alexander, and F. H. Peters, "Regrowth-free Single Mode Laser based on Dual Port Multimode Interference Reflector," *IEEE Photonics Technology Letters*, vol. 29, no. 3, pp. 279 - 282, 2017.

9. N. P. Kelly, **M. Dernaika**, L. Caro, P. E. Morrissey, and F. H. Peters, "Monolithic Integration of Photonic Devices for use in a Regrowth-free

CoWDM Transmitter," *IEEE Photonics Technology Letters*, vol. 29, no. 12, pp. 941 - 944, 2017.

10. L. Caro, N. P. Kelly, **M. Dernaika**, M. Shayesteh, P. E. Morrissey, J. K. Alexander, and F. H. Peters, "A Facetless Regrowth-free Single Mode Laser based on MMI Couplers," *Optics & Laser Technology*, vol. 94, pp. 159 - 164, 2017.
11. N. P. Kelly, L. Caro, **M. Dernaika**, and F. H. Peters, "Regrowth-free Integration of Injection Locked Slotted Laser with an Electroabsorption Modulator," *Optics Express*, vol. 25, no. 4, pp. 4054 - 4060, 2017.
12. P. E. Morrissey, N. Kelly, **M. Dernaika**, L. Caro, H. Yang, and F. H. Peters, "Coupled Cavity Single-mode Laser Based on Regrowth-free Integrated MMI Reflectors," *IEEE Photonics Technology Letters*, vol. 28, no. 12, pp. 1313 - 1316, 2016.
13. J. K. Alexander, P. E. Morrissey, L. Caro, **M. Dernaika**, N. P. Kelly, and F. H. Peters, "On-chip Investigation of Phase Noise in Monolithically Integrated Gain-switched Lasers," *IEEE Photonics Technology Letters*, vol. 29, no. 9, pp. 731 - 734, 2017.
14. S. P. Duggan, H. Yang, N. P. Kelly, L. Caro, **M. Dernaika**, M. Shayesteh, A. Gocalinska, K. Thomas, E. Pelucchi, B. Corbett and F. H. Peters, "P substrate InP based 1.5 μm lasers using an internal carbon doped layer to block p dopant diffusion," *Microwave and Optical Technology Letters*, vol. 60, no. 10, pp. 2363 - 2367, 2018.

Conference Proceedings

1. **M. Dernaika**, N. P. Kelly, P. E. Morrissey, L. Caro, H. Yang and F. H. Peters, "Single Mode Semiconductor Lasers Based on Offset Waveguides", *Photon16*, Leeds, United Kingdom, 2016.
2. **M. Dernaika**, L. Caro, N. P. Kelly, M. Shayesteh, and F. H. Peters, "Tunable Deeply Etched V-notch Reflectors," *European Conference on Integrated Optics 2017*, Eindhoven, the Netherlands, 2017.
3. **M. Dernaika**, L. Caro, H. Yang, and F. H. Peters, "A Regrowth-free, Facetless Multiple Quantum Wells AlInGaAs Semiconductor Laser Suitable for Photonic Integration," *Advanced Photonics Congress*, Zurich, Switzerland, 2018.

4. L. Caro, **M. Dernaika** and F. H. Peters, "An MMI-based Tunable Laser for Integrated Photonic Circuits", *Conference on Lasers and Electro-Optics*, San Jose, California, United States of America, 2018.
5. L. Caro, **M. Dernaika**, N. P. Kelly, P. Morrissey, H. Yang and F. Peters, "A Facetless Regrowth-free Single Mode Laser Based on Multimode Interference Couplers and Reflectors", *Photon16*, Leeds, United Kingdom, 2016.
6. N. P. Kelly, **M. Dernaika**, L. Caro and F. H. Peters, "Monolithic CoWDM Transmitter Via Integration of Injection Locked Slotted Laser With Electro-absorption Modulator", *European Conference on Lasers and Electro-Optics 2017*, Munich, Germany, 2017.
7. K. Shortiss, **M. Dernaika**, L. Caro, M. Seifikar, and F. H. Peters, "Inverse Scattering Method Design of Regrowth-Free Single-mode Semiconductor Laser for Monolithic Integration," *Advanced Photonics Congress*, Zurich, Switzerland, 2018.
8. L. Caro, N. P. Kelly, **M. Dernaika**, J. K. Alexander, P. E. Morrissey and F. H. Peters, "Widely Tunable Facetless Regrowth-free Semiconductor Laser", *European Conference on Lasers and Electro-Optics*, Munich, Germany, 2017.
9. A. H. Perrott, L. Caro, **M. Dernaika**, N. P. Kelly, P. E. Morrissey, and F. H. Peters, "Mutual Injection Locking of Lasers in a Photonic Integrated Circuit," *European Conference on Integrated Optics 2017*, Eindhoven, The Netherlands, 2017.
10. J. K. Alexander, P. E. Morrissey, L. Caro, **M. Dernaika**, N. P. Kelly, and F. H. Peters, "Integratable Optical Comb Source for Coherent Communications Systems," *Conference on Lasers and Electro-Optics*, San Jose, California, United States of America, 2017.
11. S. P. Duggan, N. P. Kelly, L. Caro, **M. Dernaika**, M. Shayesteh, J. K. Alexander, H. Yang, P. E. Morrissey, A. Gocalinska, K. K. Thomas, E. Pelucchi, and F. H. Peters, "Development of Inverted P-Substrate InP/AlGaInAs Lasers for Vertical Integration with Multiple Passive or Active Intrinsic Regions," *European Conference on Integrated Optics 2017*, Eindhoven, The Netherlands, 2017.
12. A. Perrott, P. Morrissey, F. Dubois, **M. Dernaika**, L. Caro, N. Kelly and F.

Peters, "Injection Locking Behaviour of Mutually Coupled Slotted Fabry-Perot Lasers Integrated onto a Single Growth Monolithic Photonic Integrated Circuit", *Photon16*, Leeds, United Kingdom, 2016.

List of Acronyms

WDM ..... Wavelength Division Multiplexing

EDFA ..... Erbium Doped Fiber Amplifier

OFDM ..... Orthogonal Frequency Division Multiplexing

Co-WDM ..... Coherent Wavelength Division Multiplexing

COCs ..... Coherent Optical Combs

Optical-OFDM Optical Orthogonal Frequency Division Multiplexing

RF ..... Radio Frequency

ITU ..... International Telecommunication Union

AWG ..... Arrayed Waveguide Grating

PIC ..... Photonic Integrated Circuit

SMSR ..... Side Mode Suppression Ratio

MMI ..... Multi Mode Interference

ILF ..... Integrated Laser Filter

SFP ..... slotted Fabry Pérot

IPG ..... Integrated Photonics group

EAM ..... Electro Absorption Modulators

TCCS ..... Tunable Coherent Comb Source

UV ..... Ultra-Violet

e-beam ..... electron beam

Q-factor ..... Quality Factor

IQE ..... International Quantum Epitaxy

PECVD ..... Plasma-Enhanced Chemical Vapor Deposition

HMDS ..... Hexamethyldisilizane

RPM ..... Revolutions Per Minute

ICP ..... Inductively Coupled Plasma

STS ..... Surface Technology Systems

BOE ..... Buffered Oxide Etch

SEM ..... Scanning Electronics Microscope

PMGI ..... Polydimethylglutarimide

Titanium ..... Ti

Au ..... Gold

EME ..... Eigenmode expansion

FP ..... Fabry Pérot

FSR ..... Free Spectral Range

FIBE ..... Focus Ion Beam Etching

L-I ..... Light-Intensity

DUT ..... Device Under Test

FFT ..... Fast Fourier Transform

FWHM ..... Full Width at Half Maximum

HR ..... High Reflection

AR ..... Anti Reflection

MIR ..... Multimode Interference Reflectors

TMM ..... Transfer Matrix Method

TEC ..... Thermal Electric Cooler

TLS ..... Tunable Laser Source

MZM ..... Mach-Zehnder Modulator

ASE ..... Amplified Spontaneous Emission

PC ..... Polarisation Controller

OSA ..... Optical Spectrum Analyzer

ESA ..... Electrical Spectrum Analyzer

PD ..... Photo-Diode

HWC ..... Half Wave Coupler

Chapter 1

Introduction

1.1 WDM

Wavelength division multiplexing (WDM) systems dominate the transmission technology for long haul optical links [1, 2]. In a WDM network, a series of independent lasers are used as the optical channels. Each laser is individually modulated, then combined with the other modulated signals into a single mode fibre. In order for the modern WDM network to cope with the significant increase in bandwidth demands, it must use a larger number of the available optical channels (within the erbium doped fibre amplifiers (EDFA) bandwidth) and implement advanced or multi-level modulation formats to increase the channel capacity [3, 4]. However, increasing the number of optical channels means an increase in the number of individual lasers, which dramatically escalates the cost and the size of the system. Moreover, to make use of the bandwidth efficiently, the channel spacing has to be reduced while avoiding interference between neighbouring channels. WDM systems use independent incoherent sources, which means that they have random relative phase and frequency relations that causes interference between adjacent channels. When the interference falls within the receiver bandwidth (because of the reduced spacing) it can significantly degrade the eye diagram [5]. This problem can be solved by using optical orthogonal frequency division multiplexing (OFDM), or coherent WDM (co-WDM).

1.2 Coherent optical comb and Co-WDM

Coherent optical combs (COCs) have a broad range of applications that covers metrology, spectroscopy, tomography and many other applications [6, 7, 8, 9].

Coherent wavelength division multiplexing (Co-WDM) also known as optical orthogonal frequency division multiplexing (optical-OFDM) exploits the COC to transfer terabits of data on the sum of the individual comb lines [10]. Co-WDM uses COC sources as an alternative to individual lasers to generate a number of coherent subcarriers. A narrow spacing between the adjacent channels can be used compared with standard WDM without causing interference at the receiver end, due to the known phase relationship between the comb lines [11, 12]. This feature is of great interest since the bandwidth of the EDFA following the international telecommunication union (ITU) grid standard, which has already been filled, can be utilised more efficiently.

COCs can be generated using various methods such as mode locked lasers or resonators [13, 14]. Comb lines can also be generated by using injection locked gain switched lasers that can produce narrow line width subcarriers in the order of few hundred kHz or less to be used for advanced modulation formats [15].

In Co-WDM the coherent comb lines are de-multiplexed and then separately modulated while keeping their relative phase relation intact [16]. Using this approach, it was possible to successfully transmit 298.2 Gb/s over 80 km [17] and 1.5 Tbit/s using the multiband Co-WDM technique [18]. Nevertheless, these systems need to be further optimized to make them practical and cost effective.

One of the largest challenges in implementing Co-WDM is the de-multiplexing of the comb lines. Although the COC lines are coherent and have a reliable and stable spacing, it is challenging to de-multiplex the narrow spaced individual lines to use them as separate channels. Different filtering techniques have been demonstrated for filtering the COC lines such as Bragg grating and interference filters [19, 20, 21, 22]. Although these filters work to a certain level, another issue that should be addressed is that the selected comb line will potentially have a low power, which makes it unsuitable to be used as an independent source [23], and they are designed for wider spacings. In typical WDM systems, an arrayed waveguide grating (AWG) is used as a de-multiplexer for a channel spacing of 50 GHz or more. For 25GHz channel

spacings, a set of 25 GHz optical interleavers are used with 50 GHz AWGs, since AWGs significantly increase in size with reduced channel spacing [24]. This WDM solution using AWGs and interleavers cannot be used to generate a Co-WDM signal since the phase cannot be sufficiently well controlled through the AWG and interleavers at the transmitter. Consequently, the carriers will lose their relative orthogonality, which then leads to random interference at the receiver end. Therefore, AWGs and interleavers are not an acceptable solution for generating Co-WDM signals. After de-multiplexing, each subcarrier is modulated using a separate external modulator, which further increases the size and cost of the overall system. Therefore, minimizing the cost, size, and number of photonic components by integrating all the devices on a single photonic integration circuit (PIC) is an attractive alternative and is of keen interest.

1.3 Photonic integrated circuit (PIC)

Photonic integrated circuits (PICs) based on active InP based materials with emission in the low propagation loss telecommunication bands (C and L bands) covering from 1530 nm to 1625 nm [25] provide a variety of photonic building blocks that cannot be implemented in passive material. Currently, devices such as lasers, amplifiers, modulators, and tunable filters can all be integrated on a single chip [26, 27, 28]. However, InP PICs lack the leverage of the existing micro-electronic infrastructure and silicon photonics industry. Thus, their commercial use is limited by economic factors, such as effective mass production, lead time and fabrication complexity. As a result, a generic InP integration technology initiative to share the cost between interested parties has been developed in order to push the industry forward [29, 30]. At this stage, further cost reduction, shorter processing times, and simplified fabrication processes are still necessary to extend the industry to the next level to encourage more commercial use. Laser cavities that can be fabricated with contact lithography and regrowth-free processes drastically reduce the overall time and cost of the fabrication process [31, 32]. Using this relatively simple fabrication approach tunable single mode lasers with high side mode suppression ratio (SMSR) [33, 34, 35], large tuning range [36, 37], facetless operation [38, 34] and low linewidth [39, 40, 41] were successfully demonstrated. These lasers have attracted considerable interest due to their relatively simple fabrication process and have demonstrated great potential as

cost effective tunable laser sources for telecommunication applications.

As mentioned in the previous section, for optical OFDM, integrating an AWG is not a practical solution due to two main reasons: firstly, the size of the AWG grows dramatically with small channel spacing such as 25 GHz or less. Secondly, for InP material a 25GHz AWG is not reliable due to fabrication limitations. On the other hand, injection locked lasers provide a promising alternative for de-multiplexing coherent signals, with a significant improvement regarding size, cost and fabrication simplicity. The injection locking mechanism is an efficient method to phase lock two lasers without the need of external electronics control [42]. It has a broad range of applications [43, 44, 45], and it has been used in optical filters for WDM and dense WDM systems [46, 47].

1.4 Coherent Comb de-multiplexing

In this research, the proposed first generation comb de-multiplexer PIC is based on active InP materials and consists of an multimode interference (MMI) coupler [48] and injection locked laser cavities to be used as tunable filters [49, 50]. An illustration of the PIC is shown in Fig.1.1.

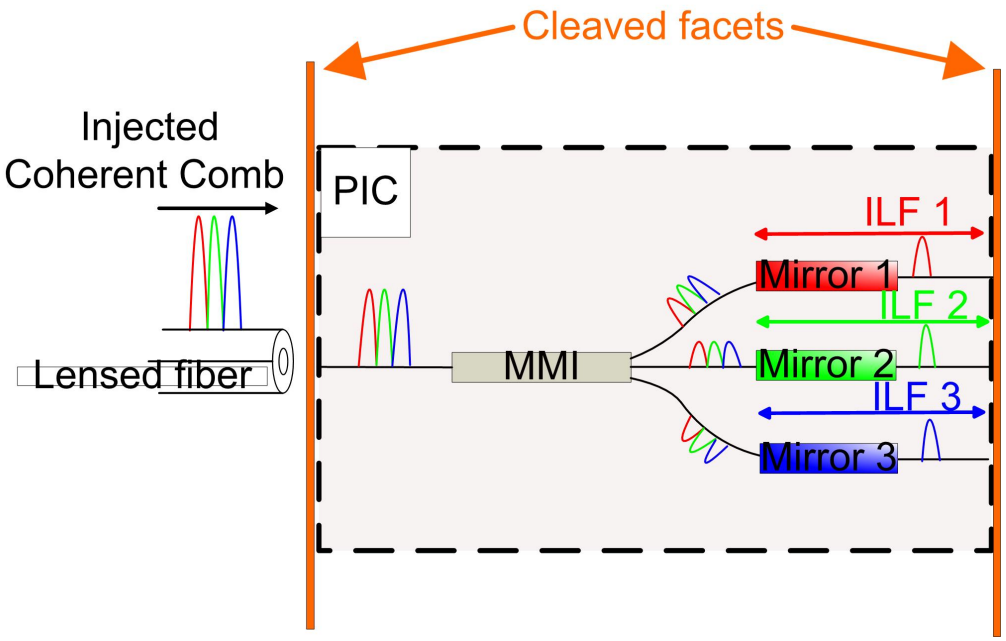


Figure 1.1: First generation comb de-multiplexer PIC. A comb is injected into the PIC through a lensed fiber. The comb is splitted into 3 arms using multimode interference coupler (MMI), each arm is then coupled to an integrated laser filter (ILF) cavities which perform filtering through injection locking

Firstly a 3 line coherent comb was injected into a 1x3 multimode interference (MMI) splitter. Each branch of the MMI is connected to an integrated laser filter (ILF) cavity. At this stage, the ILFs will act as filter by being injection locked to a single comb line originating from the comb source. The ILFs used in this design consist of 2 sections: a slotted Fabry Pérot (SFP) mirror and a gain section. The gain section relies on the cleaved facet to provide optical feedback. The SFP mirror is used to replace a cleaved facet and to provide the single mode operation. Fig.1.2 show an illustration of the ILF.

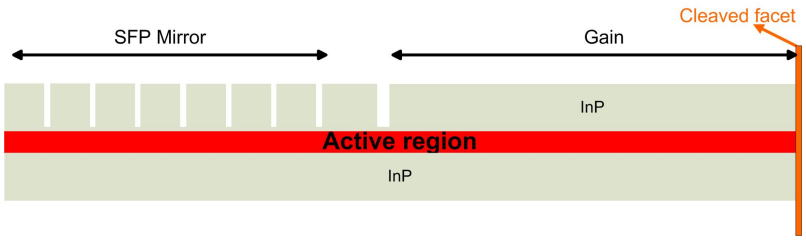


Figure 1.2: Single facet SFP cavity. The SFP laser comprises of a mirror section that consists of multiple slots to provide optical feedback, and a gain section terminating with a cleaved facet

More details about the SFP mode of operation and characteristics will be

discussed in Chapter 3. The vision of the research is having a fully integrated stand-alone Co-WDM PIC. The first potential design of the PIC based on what the Integrated photonics group (IPG) has developed so far is shown in Fig.1.3

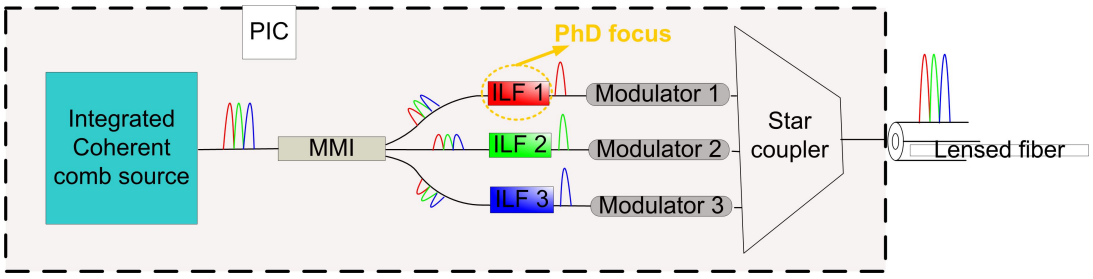


Figure 1.3: Potential design of a Co-WDM PIC. The PIC consist of a integrated comb generator, a multimode interference coupler (MMI) and electro-absorption modulators (EAMs) after the integrated laser filters (ILFs), at the end a star coupler is used to combine the branches before the modulated channel are coupled to a lensed fiber

Fig.1.3 shows the envisioned Co-WDM PIC design. First an integrated on-chip tunable coherent comb source (TCCS) will be used to generate 3 comb lines. The TCCS has already been developed and is reported in [15]. Next the filtering section consist of a 1x3 MMI splitter and 3 ILFs, the ILFs developed are the SFP lasers shown in Fig.1.2 and are placed on the chip as presented in Fig.1.1 . The reported results from the current demultiplexer design are reported in [49] and [50]. Finally, each filtered line is modulated using an electro-absorption modulator (EAM). A characterization study of the EAMs can be found in [51]. The PIC will emphasize designs using devices with a relatively simple fabrication process and with the potential of reducing the fabrication and packaging costs by adding all discrete components into a single power efficient chip. Therefore, the ILF laser design will focus on grating-free cavities that use a standard ultraviolet (UV) lithography process. The design above is necessary to avoid a costly and time consuming practice of epitaxial regrowth or the need to use high resolution lithography such as electron beam (e-beam). The main focal point is the development of a compact integrated facetless laser that operates as a single mode filter when injected by a coherent comb source. The output of the ILF should exhibit a side mode suppression ratio (SMSR) of around 30 dB, where here the SMSR is defined in terms of the desired and unwanted comb lines. There are several aspects of the proposed PIC that can be considered novel, such as tunable channels, de-multiplexing,

selective amplification and full integration. It also have a very promising industrial application in the telecommunication infrastructure. Furthermore, the PIC will present a significant improvement in terms of size compared with the AWG, since the PIC size does not depend on the channel spacing as shown in Fig.1.4. Moreover, it offers tunable channel de-multiplexing and selective amplification which the AWG does not offer.

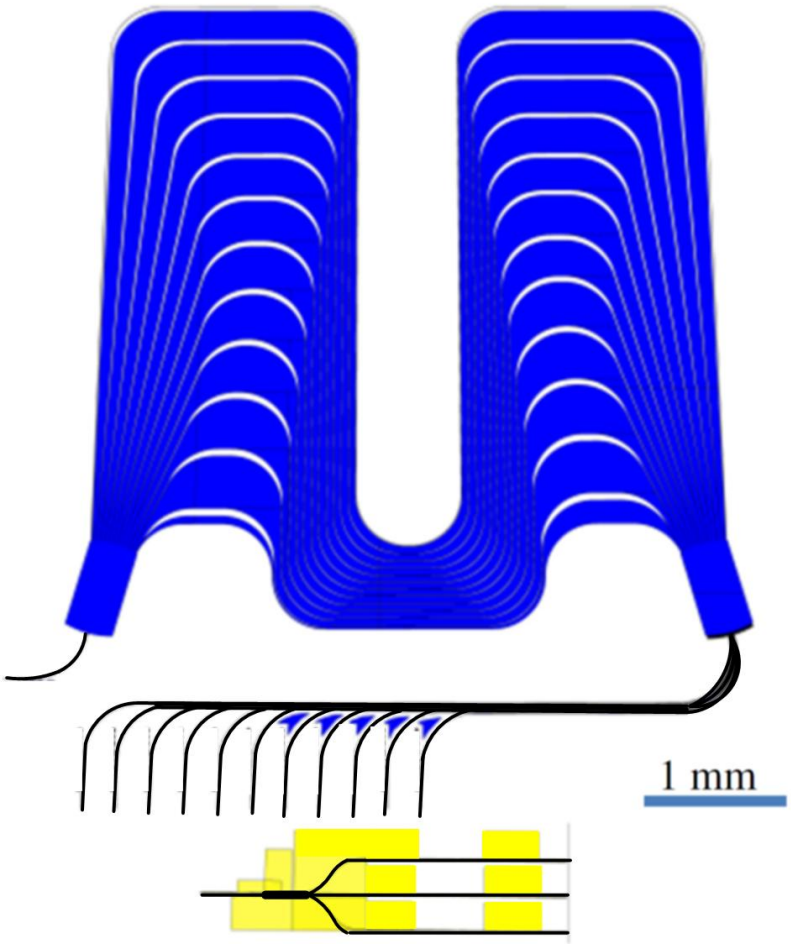


Figure 1.4: Size comparison between 25 GHz AWG (top) and the proposed PIC (bottom).The PIC present a significant improvement in term of compactness

1.5 Integrated laser filters (ILF)

The single facet SFP laser is the original ILF used for comb de-multiplexing. However, the SFP lasers have several limitations that restrict the overall PIC performance. The aim of this PhD work is to find solutions to the current limitations of the SFP laser, and develop a better optimized ILF solution. The solutions could be in the form of improving the current ILF design or finding

an alternate cavity design. the limitation of the SFP and the PhD goals are presented below.

Limitations of the current ILF design

- The ILF based on SFP lasers suffers from low fabrication yield and inconsistent laser performance. The achieved SMSR was limited to 22 dB with poor laser repeatability.

- The current design relies on a cleaved facet, which prevents full integration

- The SMSR of the de-multiplexed coherent comb is limited to around 21 dB

PhD goals

- Improve the current laser design or investigate alternate designs in order to increase the yield and consistency of the lasers

- Eliminate the need for a cleaved facet by designing facetless lasers

- Improve the SMSR of the de-multiplexed comb lines when the laser is used as an ILF.

The thesis will highlight the two approaches taken to solve the problems:

1) Investigating deeply etched reflection structures similar to the slot in term of mode of operation but with better fabrication yield. This approach successfully solved the fabrication yield issue of the SFP but did not improve the comb de-multiplexing performance.

2) Developing a completely different type of integrated laser based on active rings with high quality factors (Q-factor). This approach successfully improved the SMSR of the filtered comb and made the ILF facetless with integration capabilities.

1.6 Thesis structure

This thesis consists of 5 chapters including the introduction and the conclusion. The first chapter (Introduction) highlights the motivation of this work, the challenges and PhD goals.

Chapter 2 (Fabrication) will discuss in detail the regrowth-free fabrication process that uses standard contact lithography and the metal first fabrication process, which further optimized the process.

Chapter 3 (Semiconductor Laser) will first discuss the mode of operation of the existing ILF, the SFP lasers and their limitations. Afterwards, the novel structures designed to replace the slots, increase the fabrication yield and ensure a consistent laser performance will be presented. Finally, the SMSR limitation of using such lasers as coherent comb de-multiplexers will be discussed. Moreover, a brief discussion about the cavities Q-factor and its relation with the filtering performance will follow.

Chapter 4 (Ring Lasers) will present active ring resonators as a solution to overcome the SMSR limitation of the linear cavities and demonstrate a fully facetless ILF. The steps taken to optimize the ring cavities by reducing the bend loss and choosing the appropriate couplers will also be presented. Finally, the results of de-multiplexing a coherent comb with spacing of 10 GHz and 20 GHz with SMSR improvement will be presented.

Chapter 5 (Conclusion and Future Work) will summarize the thesis findings by emphasizing the contributions and the novelty of this work. Moreover, the last subsection in this chapter will discuss the expected future work.

Chapter 2

Fabrication

The core of this research is to develop facetless lasers suitable for integration using a regrowth-free process and contact lithography. By eliminating the need for having multiple growth steps, the process complexity is significantly reduced, which results in faster device turnover and cutting costs from using more or the same equipment multiple times. Moreover, the implementation of contact lithography instead of high resolution lithography such as electron-beam further reduces the process time and makes it more suitable for mass production. This approach has the advantage of significantly reducing the overall cost and process time of the fabrication. The next section will discuss the commercial material used in the fabrication of the devices in this project.

2.1 Material

In this research, the epitaxial material used in the fabrication of the lasers was commercially available off the shelf material purchased from International Quantum Epitaxy (IQE). The epitaxial structure of the wafer is shown in Table 2.1.

Table 2.1: Epitaxial structure of the wafer used in the fabrication.

Layer	Material	Thickness (µm)	Dopant	C-V Doping (cm^{-3})
16	$GaIn_{(0.53)}As$	0.2	Zinc	>1.50e19
15	$GaIn_{(0.71)}As_{(0.62)}P$	0.05	Zinc	>3.00e18
14	InP	0.1	Zinc	>1.50e18
13	InP	1.5	Zinc	1.00e18
12	$GaIn_{(0.85)}As_{(0.33)}P$	0.02	Zinc	1.00e18
11	InP	0.05	Zinc	7.00e17
10	$[Al_{(0.9)}Ga]In_{(0.53)}As$	0.06	Zinc	4.00e17
9	$[Al_{(0.72\ to\ 0.9)}Ga]In_{(0.53)}As$	0.06	Undoped	
8	$[Al_{(0.440)}Ga]In_{(0.49)}As$	0.01	Undoped	
7	$([Al_{(0.24)}Ga]In_{(0.71)}As) * 5$	0.006	Undoped	
6	$([Al_{(0.440)}Ga]In_{(0.49)}As) * 5$	0.01	Undoped	
5	$[Al_{(0.9\ to\ 0.72)}Ga]In_{(0.53)}As$	0.06	Undoped	
4	$[Al_{(0.9)}Ga]In_{(0.53)}As$	0.06	Silicon	1.00e18
3	$[Al_{(0.86\ to\ 0.9)}Ga]In_{(0.53)}As$	0.01	Silicon	1.00e18
2	InP		Silicon	1.00e18
1	InP		Silicon	3.00e18
Substrate				

The IQE epitaxy consists of a N-doped substrate with 5 AlInGaAs strained quantum wells sandwiched between 6 barriers. A 20 nm In(0.85)GaAs(0.33)P layer just above the active region is used as an etch stop layer for chemical wet etching when needed (layer 12). The 2 top layers: GaIn(53)As and In(0.71)GaAs(0.62)P are the metal contact layers (layer 16 and 15). The layers from top to bottom form a PIN junction, with the zinc and silicon used as P and N dopants respectively. The refractive index profile of the epitaxial is shown in Fig.2.1

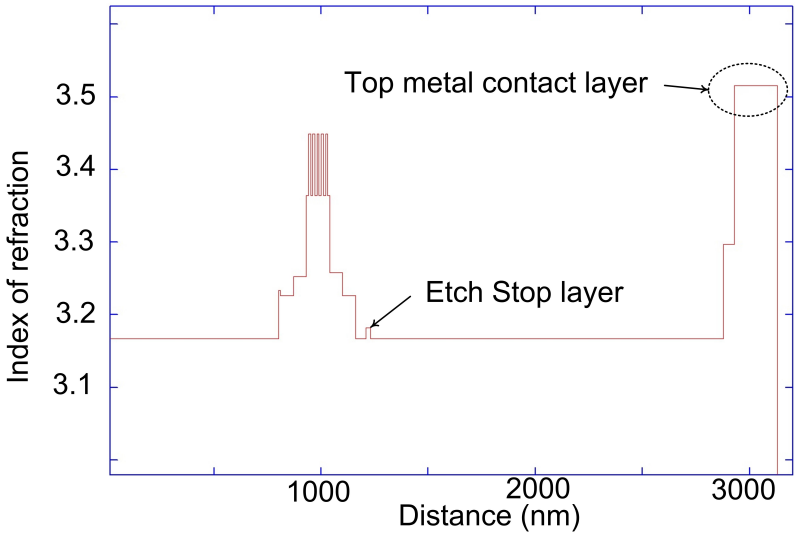


Figure 2.1: Refractive index pattern of the epitaxial wafer, clearly showing the top metal and etch stop layer

From right to left the plot shows the refractive index of the metal contact layers, top InP cladding, etch stop layer, active region and bottom InP cladding.

2.2 Mask design

The integrated photonic group runs a direct current (DC) multi-project wafer fabrication process; this process allows various parties from different projects to share the same mask following the same set of fabrication process and rules. The aforementioned process, combines multiple projects on a single wafer in the same fabrication run. By using only one fabrication run on a single wafer instead of multiple runs with multiple wafers. This leads to a significant cut in overall process cost. However, the down side of this approach is each project will have less devices per run. In term of fabrication time, the typical processing time of the chips is between 4 to 8 days. This section will discuss the mask design and layers.

The mask layers are designed using in-house developed C++ based software called PICDraw. The software contains basic building blocks for PICs such as ridges, bends and MMIs. The software was created and developed by Prof. Frank H. Peters and licenced to Tyndall National institute, it allows a flexible design control which facilitate complex device design. A typical process with 2 different etch depths requires a mask with at least 4 layers. For the process developed as part of this research, the first layer is used to define ridges,

electrical isolation slots, reflection slots and any other structures that are ridge related. The second layer defines the deep etch layer. The third layer is the oxide open layer. In this step the oxide is opened on the top of the ridge for metal contact. The fourth and last layer is used for contact metal lift-off. Fig.2.2 (a) shows the layout of the mask at the design stage in which all 4 layers overlap. The quarter wafer contains devices that spread across 4 different research projects. Fig.2.2 (b) show the final mask design, that will be send to Compugraphics-Photomasks, the manufacturer of the mask plate.

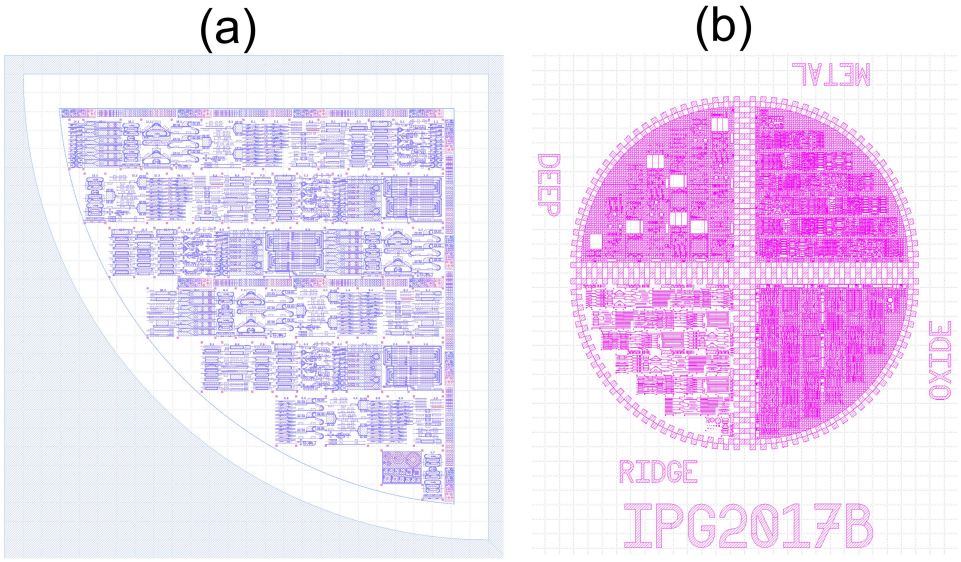


Figure 2.2: (a) Quarter wafer design taken from PICDraw with overlapping layers (b) Quad mask design showing the 4 lithography layers

2.3 Standard Process

A quarter wafer is used in the fabrication process. The initial wafer size was 2 inch. 4 quarters were cleaved and each was used for a different process as shown in Fig.2.3

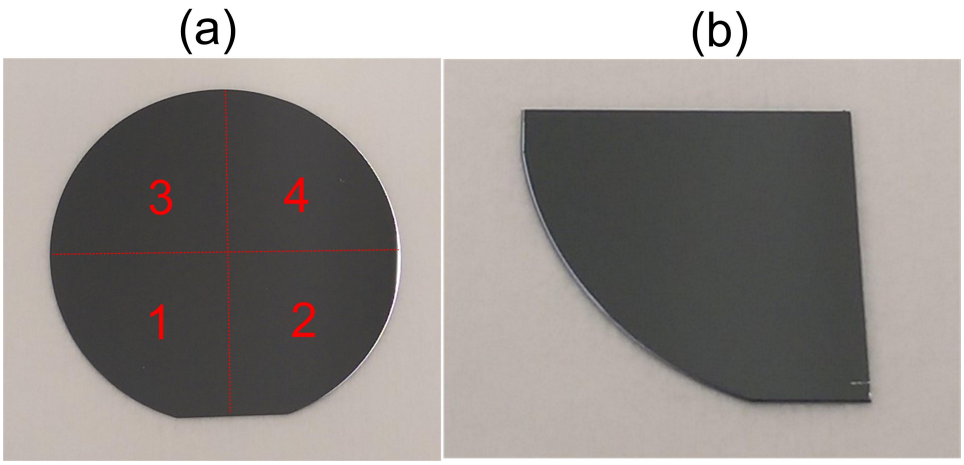


Figure 2.3: (a) 2 inch full wafer before cleaving showing the 4 quarter outline (b) quarter inch wafer used for fabrication

Fig.2.3 (a) shows the full 2 inch wafer, the numbers 1 to 4 represent the cleaved quarter, that will be used in the process as shown in Fig.2.3 (b). The number of the quarter is important in case the process uses chemical etching which is sensitive to the crystal orientation.

In this chapter, Illustrations will be used to describe the fabrication process. It is important to note, that the dielectrics and photoresist are not planarized, they are shown flat and uniform for illustration purposes, and to make the drawing clearer.

2.3.1 Ridge Lithography

The first step in the fabrication is to deposit around 600 nm of silicon dioxide (SiO_2) on the epitaxial (EPI) quarter as shown in Fig.2.4

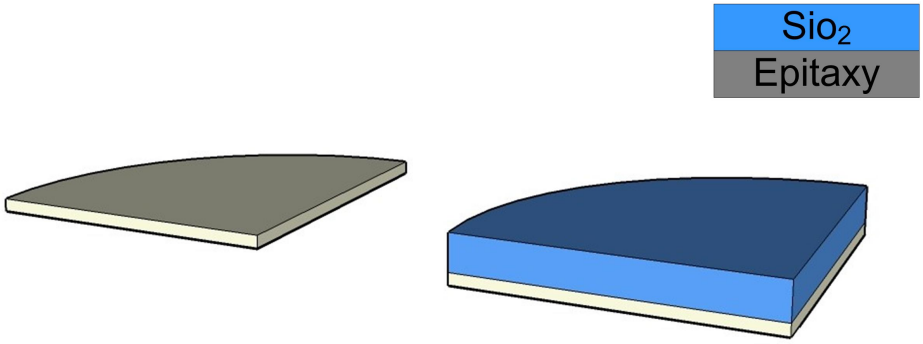


Figure 2.4: Quarter wafer with no oxide (left), quarter after oxide deposition (right)

The SiO_2 is deposited using plasma-enhanced chemical vapor deposition (PECVD), which has a deposition rate that varies between 25-32 nm/minute for SiO_2. After the deposition, the SiO_2 film thickness is measured using a tool named NanoSpec from Nanometrics that uses reflectometry to determine film thickness based on interference effects.

The next step involves preparing the sample for the ridge lithography by depositing hexamethyldisilizane (HMDS) and S1813 photoresist. The HMDS is used as photoresist adhesion promoter with the epitaxy, and a thin layer is deposited using evaporation. The S1813 is a positive photoresist from SHIPLEY and is deposited by spinning the sample at 4000 revolutions per minute (RPM) for 50 seconds. The spinning speed results in a photoresist thicknesses of around 1.3 μm. Afterwards, the sample is baked for 2 minutes at a temperature of 115 °C on a hot plate, to harden the photoresist. Fig.2.5 shows the sample structure after the deposition.

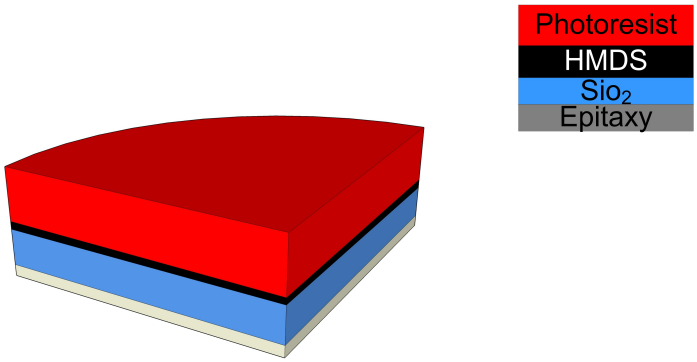


Figure 2.5: The quarter after HMDS and photoresist deposition

At this stage the sample is aligned and exposed for around 6 seconds using a UV contact lithography mask aligner. Next the sample is developed using MF319 developer. The time of development varies between 25 to 30 seconds, which is determined by checking the sample under the microscope after the development to make sure that the intended resolution is attained. Fig.2.6 (a) and (b) shows a microscope image and an illustration of the ridge at this process level.

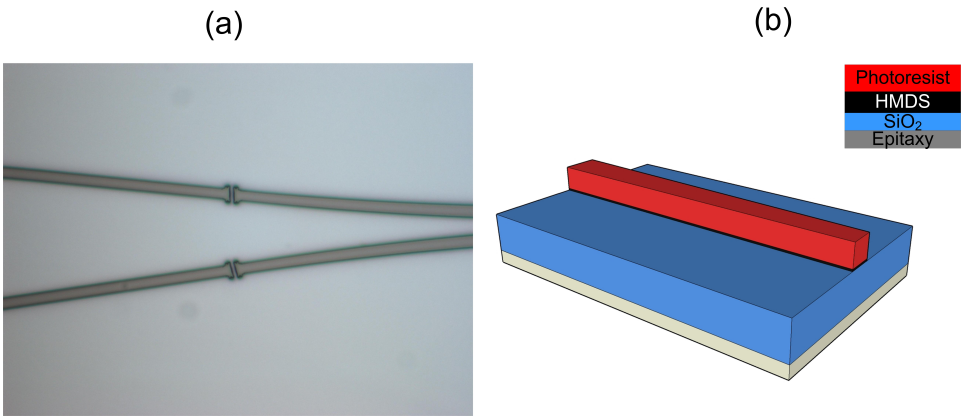


Figure 2.6: (a) Microscope image of the photoresist ridge, (b) illustration of the Patterned ridge using HMDS and photoresist

The next step is to define the ridge shape using an SiO_2 hard mask. The SiO_2 is etched using a inductively coupled plasma (ICP) tool from surface technology systems STS . The equipment is referred to as an STS-ICP. The etch rate for SiO_2 is around 280 nm/minute. The etching recipe consists of a mix of Fluoroform (CHF_3) and Tetrafluoromethane (CF_4) with a ratio of 7:3 respectively at platen power of 74 W . This recipe is selective to SiO_2 and does not interact with the InGaAs that forms the top layer of the EPI. After the etch, the sample is soaked in the photoresist remover 1165 to remove any remaining photoresist. Fig.2.7 shows the progress of the sample. Fig.2.7 (a) shows the oxide ridge and Fig.2.7 (b) show the illustation of the ridge shape

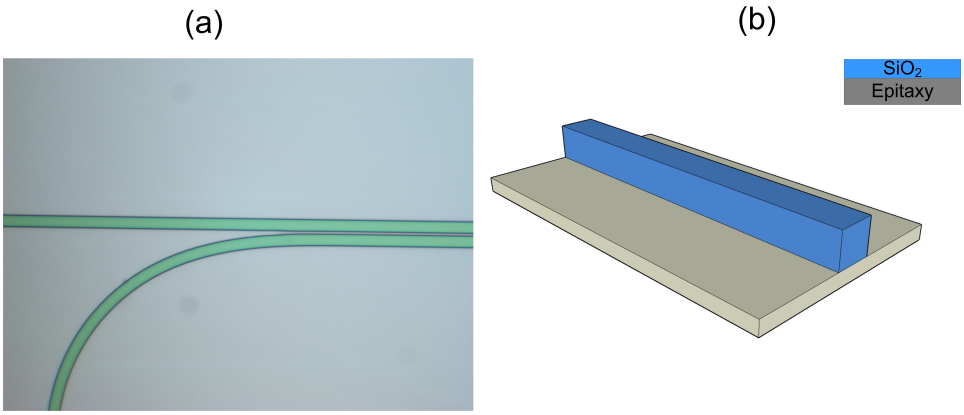


Figure 2.7: (a) microscope image of the oxide ridge after removing the photoresist, (b) illustration of the ridge shape

At this stage the oxide ridges are fully defined, the sample is ready to go through the next lithography step preparation.

2.3.2 Deep lithography

Sharp bends, deep etched slots, and other reflective structures require a deep etch in order increase the light confinement in the waveguide by introducing a higher index contrast. On the other hand, most ridges and other structures are designed with a low loss shallow etch. Therefore, in order to achieve two etch depths, the deep lithography step was introduced. Firstly, the whole sample is covered with silicon nitride Si_3N_4 as shown in Fig.2.8

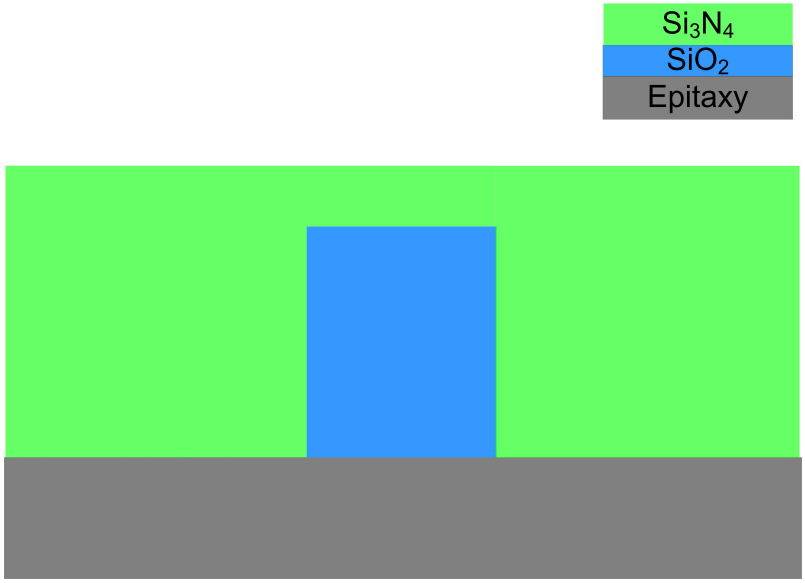


Figure 2.8: Si_3N_4 deposition across the wafer

Fig.2.8 shows how all the oxide ridges on the quarter are covered with Si_3N_4. The Si_3N_4 was deposited using PECVD similar to the SiO_2. Afterwards HMDS and S1813 are deposited on the sample, and using the mask aligner, the sample is aligned to the deep etch layer and exposed and then developed using MF319. The shallow etch area will remain covered with photoresist as shown in Fig.2.9

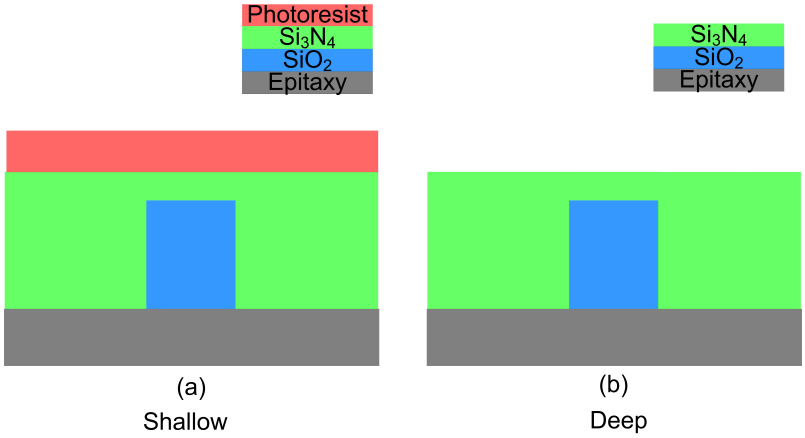


Figure 2.9: (a) shallow area with Si_3N_4 covered with photoresist, (b) deep etch area with exposed Si_3N_4

Using the STS-ICP etcher the Si_3N_4 is removed from the exposed area which will to be the deep etch region. This is shown in Fig.2.10.

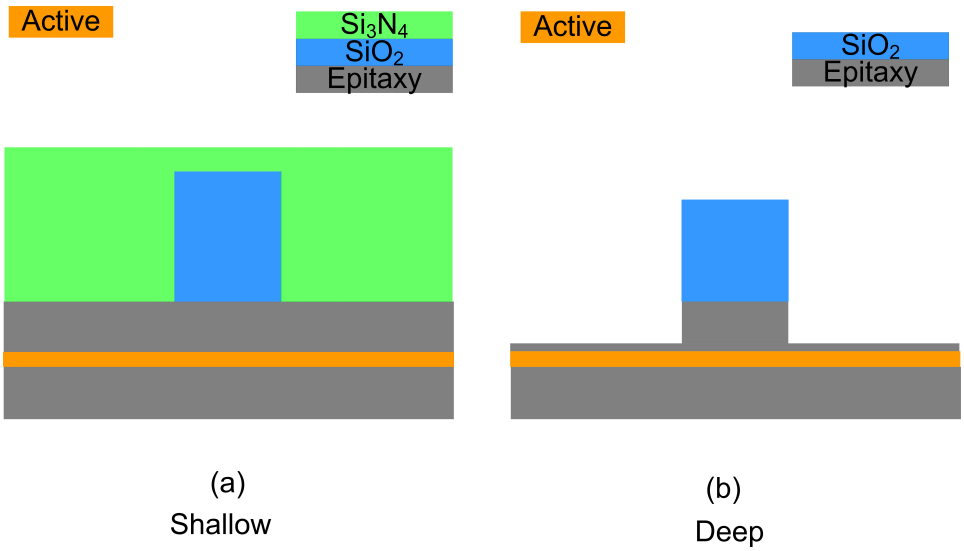


Figure 2.10: (a) shallow ridge still covered with Si_3N_4 and photoresist, (b) deep ridges area with exposed semiconductor and no Si_3N_4

The dry etch recipe used to remove the Si_3N_4 uses sulfur hexafluoride SF_6, which is highly selective to the SiO_2 ridge with selectivity exceeding 1:10. Fig.2.11 shows a microscope image of the deep and shallow areas after removing the Si_3N_4 from the deep area and the left over photoresist on the shallow areas.

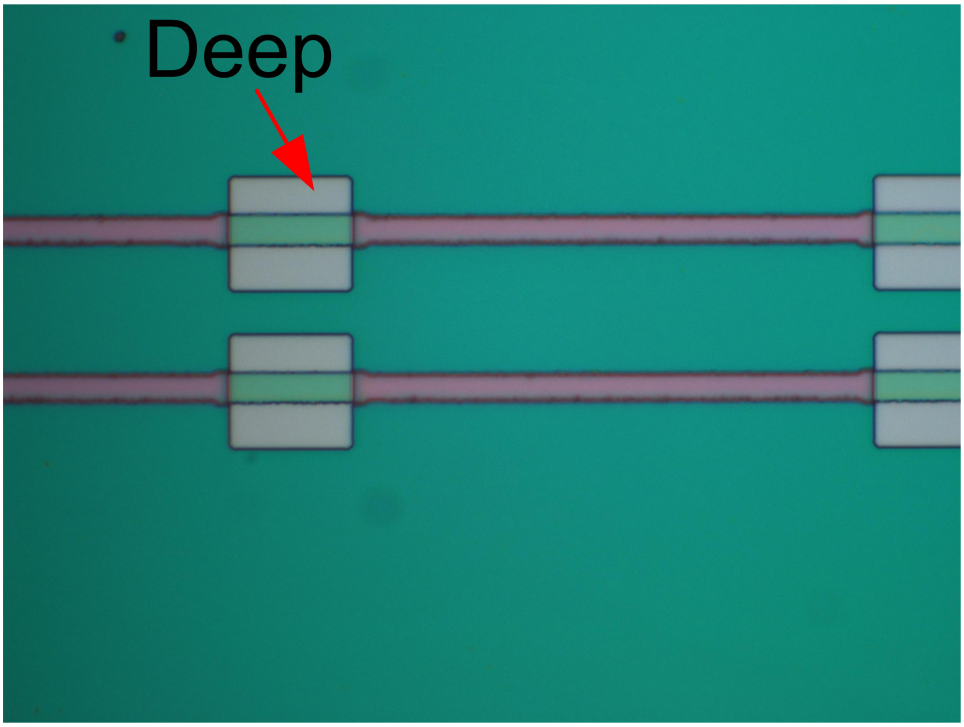


Figure 2.11: miscroscope image showing the deep and shallow areas. Deep area showed in the white rectangle

The white rectangles in Fig.2.11 represents the deep region parts, where the oxide ridges are exposed. whereas all the green areas are for the shallow etch and still covered in Si_3N_4.

The next step is to etch into the epitaxy for the deep region using the plasma dry etch. The three gases used in the etch are chlorine, methane and hydrogen ($CL_2/CH_4/H_2$) with a ratio of 5:4:2 respectively at 20 °C. Fig.2.12 shows the sample progress after the first etch. It's important to note, that the Si_3N_4 thickness is chosen to be at least 350 nm in order to withstand the first semiconductor etch, InP to Si_3N_4 semiconductor etch seletivity is 10:1 respectively.

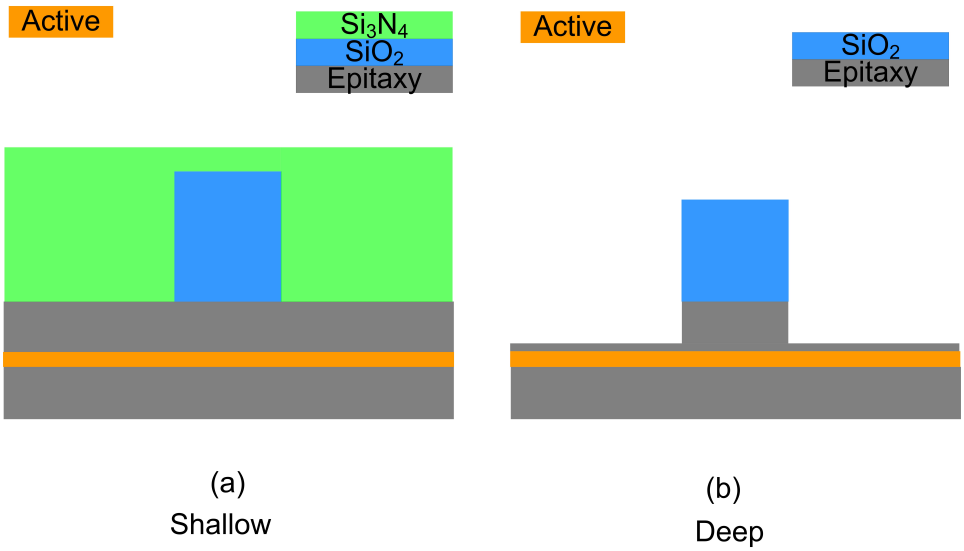


Figure 2.12: (a) shallow area protected with Si_3N_4 (b) deep area etched into the semiconductor material

The first etching process etched down to just above the active region (orange). In this step, an accurate depth control is not necessary as long as the depth is more than 1 μm deep. It is important to note that the plasma etch recipe used to etch the semiconductor also etches SiO_2 and Si_3N_4. However, there is enough film thickness to protect the intended areas during the full etch process. Next the Si_3N_4 is removed from the shallow area and then the second semiconductor etch takes place in order to define the shallow ridge depth. Fig.2.13 shows the shallow and deep ridges after removing the left over SiO_2 hard mask. In both shallow and deep areas. The SiO_2 was removed using a wet chemical etch employing buffered oxide etch (BOE).

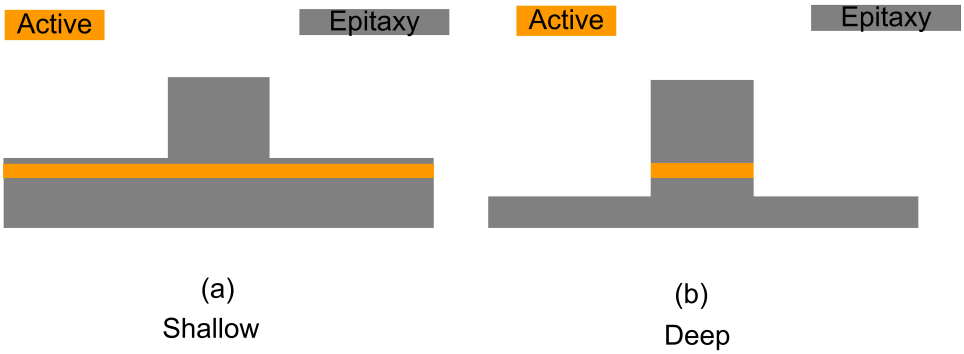


Figure 2.13: (a) shallow ridge after completely removing the Si_3N_4 and etching through the semiconductor material to ajust above the active region, (b) deep ridge etched through the active region

The active region is approximately 1.85 μm deep, so ideally the shallow depth area should stop just above it. In our process the typical shallow ridge depth is around 1.8 μm and the deep ridge is well below the active region with a depth of 2.8 to 3 μm. Fig.2.14 show a scanning electronics microscope (SEM) image with both shallow and deep regions.

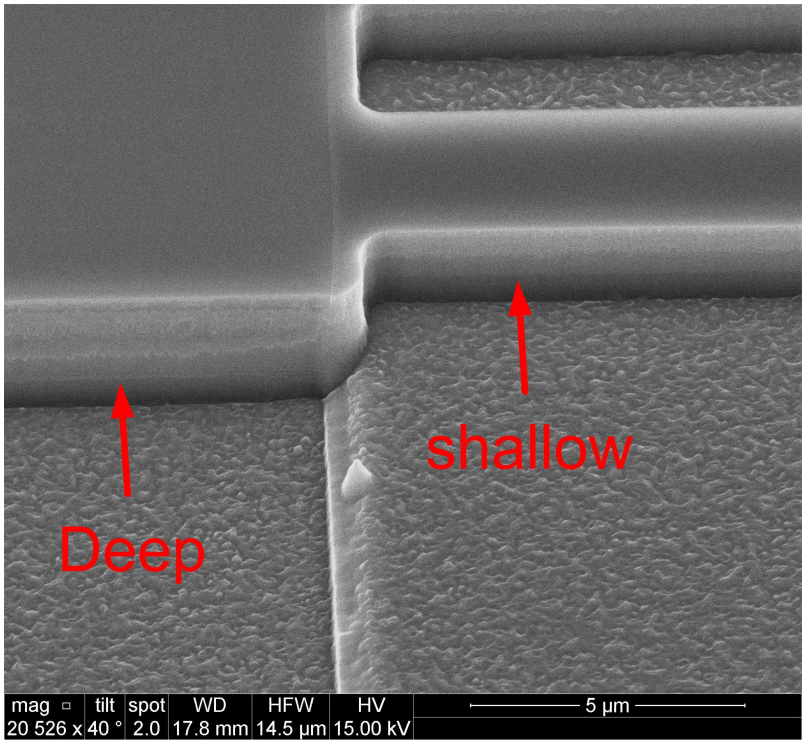


Figure 2.14: SEM showing the shallow and deep ridges with the interface in between

The SEM in Fig.2.14 shows the interface between shallow and deep with smooth side walls on both areas. As mentioned above, the etch depth in the deep area is not critical and can be over etched as long as it goes though the quantum wells. On the other hand, the shallow ridge should be etched as close to the active region as possible without going through it. Moreover, in this process no wet chemical etching is used, so an etch based on plasma dry etching had to be implemented. The depth control accuracy is achieved by using the state of the art LEP500 etch depth monitor from Intellemetrics. The etch monitor provides real-time, in-situ plasma etch depth monitoring and end point detection plus a wafer vision system.

Using a custom simulation software (Vertical), the simulated reflectance data for the etch was generated and compared with experimental data. Fig.2.15 shows the simulated reflectance of the material aligned with the refractive

index profile of the epitaxy.

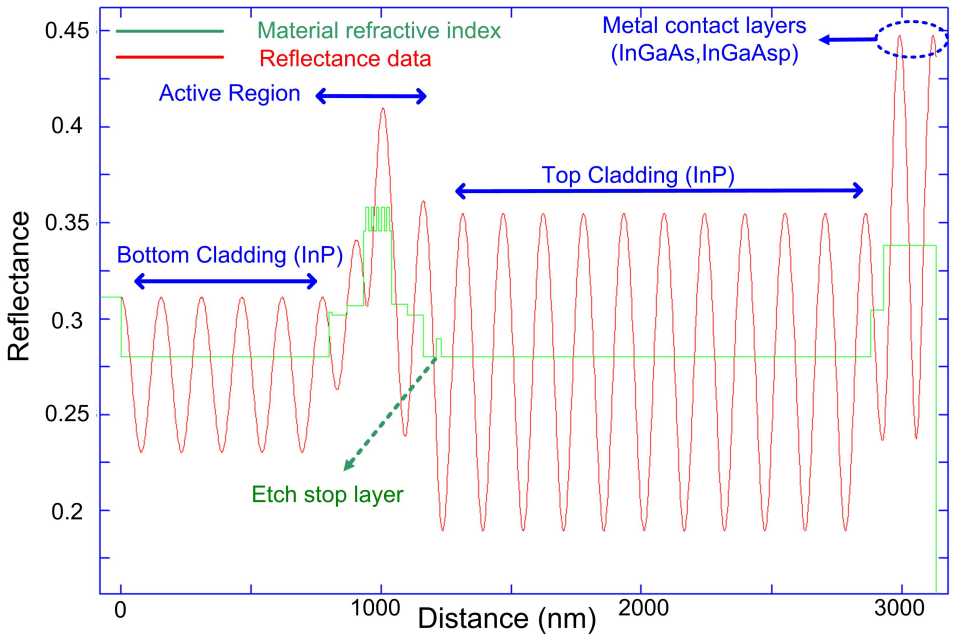


Figure 2.15: Simulated data of the material reflectance overlapped with refractive index profile. The graph shows all the levels of the epitaxy reflectance profile and refractive index

The data in Fig.2.15 shows the expected reflectance at each material level. Based on the simulation the active region starts at the peak number 14 (counting from right to left). Therefore, the shallow etch should stop at peak 13 in order to stop just before the active region. Fig.2.16 shows a comparison between the simulation and experimental reflectance.

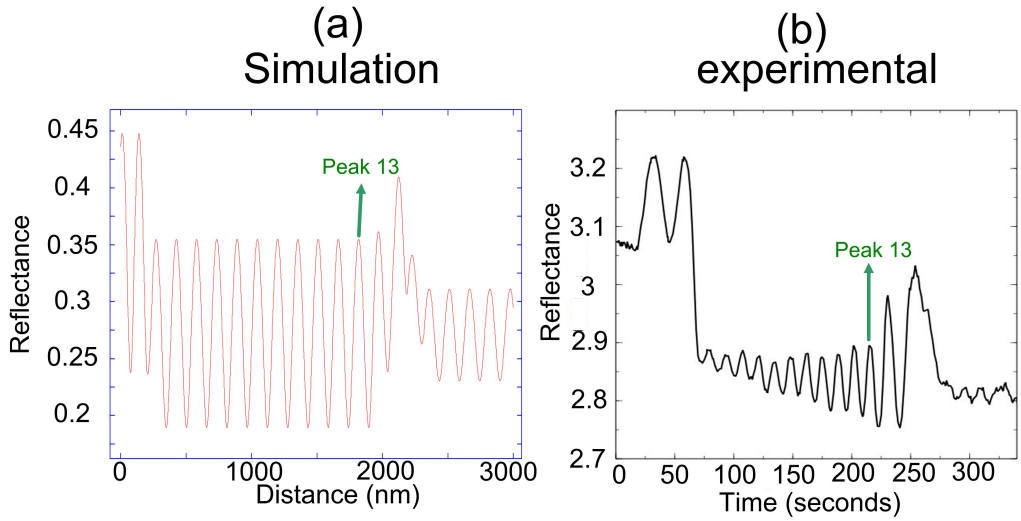


Figure 2.16: (a) simulated reflectance showing the border of the shallow etch at peak 13, (b) experimental reflectance also showing peak 13 that will be used to define shallow etched ridges

A strong agreement exists between the simulation and experimental data in terms of general shape and number of peaks. As highlighted in Fig.2.16 (a) and (b) the peak number 13 shows where the shallow etch should stop. By using this technique it was possible to accurately control the depth of the shallow areas on the wafer.

It is important to note that before the use of the depth etch monitor and the simulation software (Vertical), the shallow etch was highly inconsistent between various fabrication runs. There was often a risk of under-etching or over-etching, which affects the quality of laser performance. The slotted Fabry Pérot lasers are particularly depth sensitive. To overcome this problem, wet chemical etching was used. However, chemical wet etching is directional in relation of the crystal orientation of the material. Therefore, it affect ridges with various orientation differently. This will cause some ridges to have mesa shapes while other ridges will have undercuts. Therefore the optimization of the process that comprises the etch depth monitor and the simulation software improved the fabrication yield, depth accuracy, and overall complexity.

2.3.3 Oxide opening lithography

The third lithography step is used for the oxide opening. The main goal of this step is to create a oxide opening on top of the ridges for the P-metal contact. A fresh film of SiO_2 is deposited with a thickness of 400 nm. This oxide layer is

used to passivate the side walls of the ridge to reduce current leakage and additional optical losses. The sample preparation for the lithography is similar to the previous lithography steps using HMDS and S1813. However, the oxide open layer has an alignment tolerance of 500 nm on the X and the Y axis, for a 2.5 μm ridge the opening is 1.5 μm. Fig.2.17 (a) shows an illustration showing the oxide opening shape on top of the ridge, and Fig.2.17 (b) shows a microscope image of a ridge with an opening.

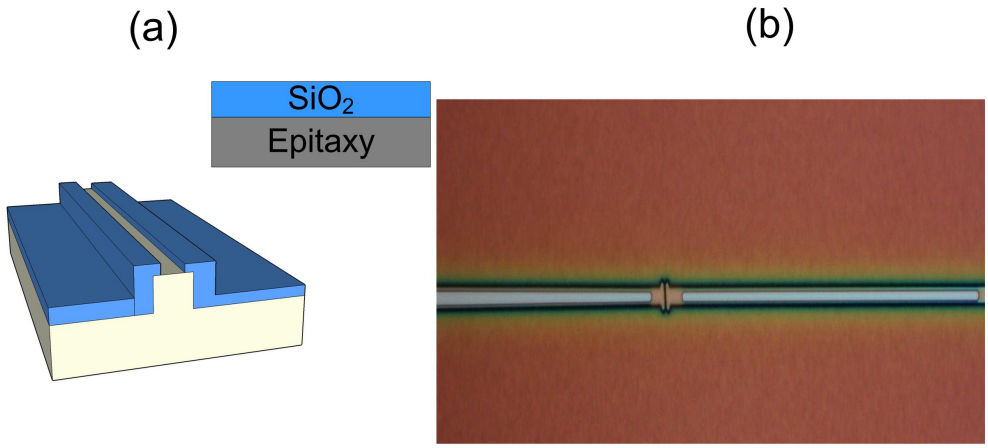


Figure 2.17: (a) illustration of a ridge with oxide opening (b) microscope image of a ridge with oxide opening

2.3.4 Metal Lift off lithography

The fourth and last lithography step is used for the metal lift off. This step is performed just before depositing the P-metal. Two resists are used: LOR 10A (from Micro Chemicals) and S1813. The LOR 10A is based on polydimethylglutarimide (PMGI) and is used as an undercut layer to assist with the lift off. The LOR 10A is baked at 150 °C for 3 minutes after spinning at 4000 RPM. Afterwards, the photoresist S1813 is deposited and baked for 2 min at 115 °C. After exposure, the sample is developed using MF319 until a clear undercut is observed on the microscope as shown in Fig.2.18.

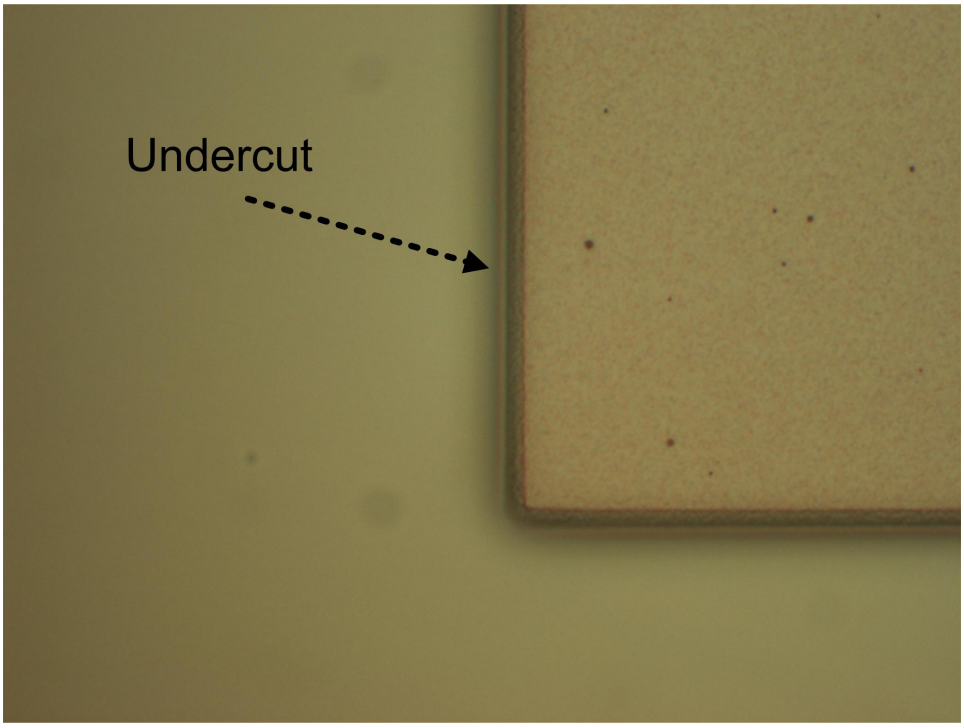


Figure 2.18: Microscope image of the photoresist undercut necessary for metal lift off

A deep undercut is important to ensure a successful lift off. The P-metal consists of 25 nm titanium (Ti) and 600 nm gold (Au). The Ti is used as an adhesion layer between the semiconductor and Au, as it prevents the Au from peeling off the semiconductor surface. An illustration in Fig.2.19 shows a metal covered ridge.

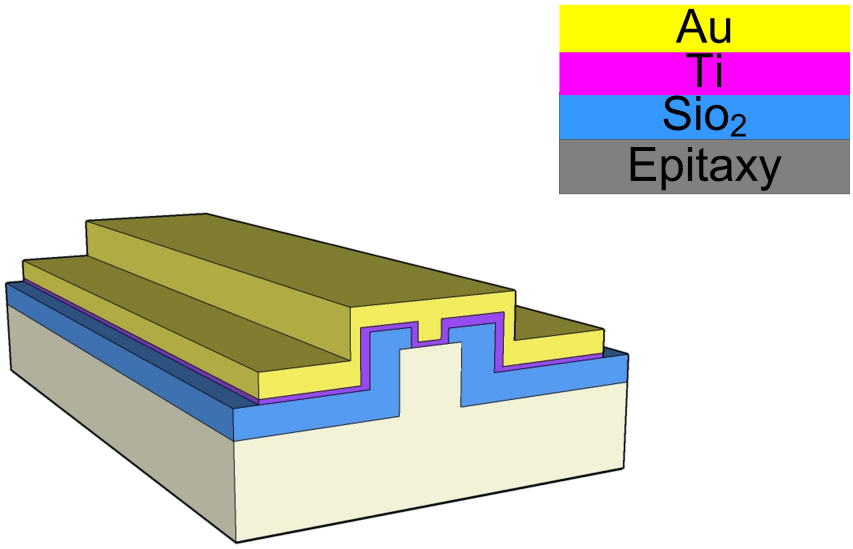


Figure 2.19: Illustration of a metal covered ridge, showing the Ti and Au contact with semiconductor through the oxide open

Fig.2.20 shows before and after lift off images after metal deposition.

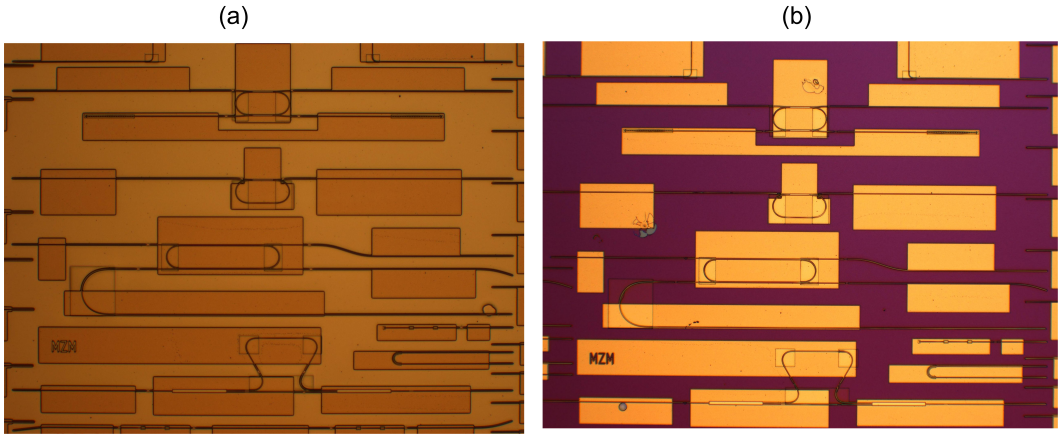


Figure 2.20: (a) devices after top metal deposition (b) devices after top metal lift off

Fig.2.20 (a) shows devices after Ti:Au deposition and Fig.2.20 (b) shows the same area after a successful metal lift off. The sample is usually left overnight soaked in the photoresist remover 1165 to ensure small areas around the isolation slots are lifted off effectively. In some cases an ultrasonic bath is used to removed left over patches across the chip.

After the metal lift off, the substrate is thinned using a bromine solution from 350 μm to around 100 μm. The next steps consist of depositing 20 nm Ti and 300 nm Au on the back side of the wafer for N-metal contact. Finally the chip is annealed at 400 °C for 5 min and cleaved into bars.

2.4 Metal first Process

The previous section (Standard Process) discussed the standard fabrication process used in the group. Recently, a new process was developed, which involves depositing metal first in order to improve the top metal contact and increase the fabrication yield.

In the standard process, top metal is deposited in the oxide window opening on the top of the ridge, as shown in Fig.2.19. It has been observed that in certain cases where the oxide opening is not wide enough or not fully open, the devices suffers from high contact resistance which eventually led to electrical damage. Moreover, a number of fabrication runs were unsuccessful due to the poor metal contact quality. In order to overcome this issue, the metal first process was developed.

Most of the process steps are the same as the standard process, however in this refined process a Ti:Au:Ti layer is deposited before the 600 nm SiO_2 layer at the start of the process. The thickness of the Ti:Au:Ti layers are 25:50:25 respectively. The last Ti layer is used after the Au to improve adhesion between Au and SiO_2. Fig.2.21 show a comparison between the standard and the metal first process at the start of the process.

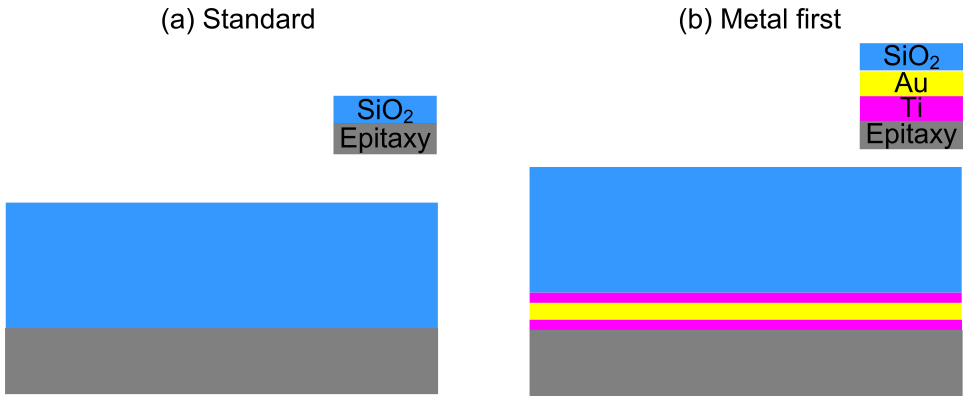


Figure 2.21: (a) standard process first step with only SiO_2 deposited, (b) Metal first process with Ti:Au:Ti deposited under SiO_2 layer

By depositing the metal first a wider metal contact covers the ridges, which is protected from any damage through the remainder of the process. Moreover, due to low tolerance of the oxide opening step, the metal process ensures a good contact even if the opening is small, which increases the overall reliability and reproducibility of the process. The same recipe of etching SiO_2 is used to etch the Ti and Au, resulting in no additional processing steps or extra etching recipes. Fig.2.22 show an illustration of the ridges structure in both standard and metal first processes

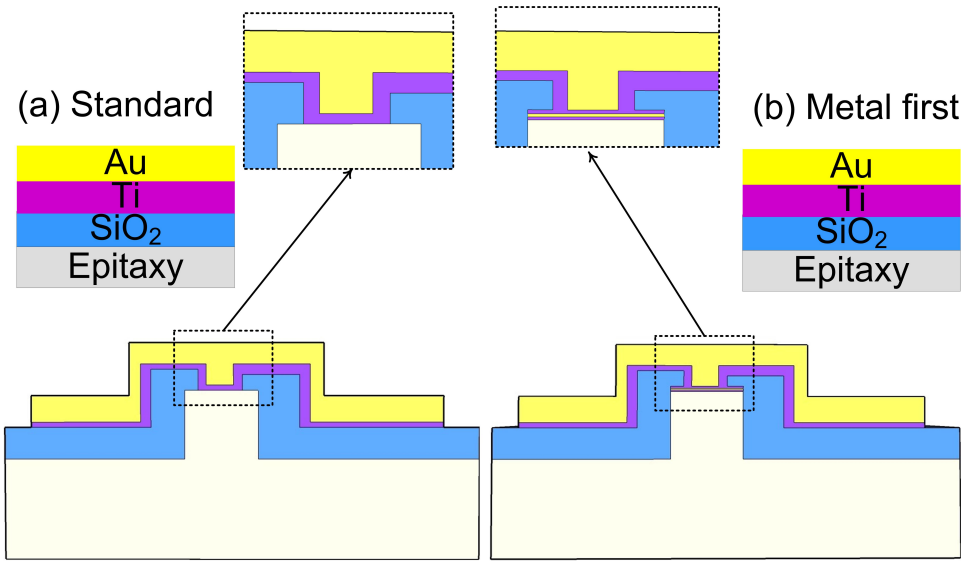


Figure 2.22: (a) standard process ridge, (b) Metal first process ridge

Fig.2.22 (a) shows the ridge with oxide window open that is narrower than the ridge leading to a smaller semiconductor/ metal contact area. Fig.2.22 (b) show the metal first process with metal covering the full ridge width and ensuring a better metal contact.

Chapter 3

Semiconductor lasers

3.1 Semiconductor lasers

The first stage of the project employed slotted Fabry Pérot lasers (SFP) lasers to perform the comb de-multiplexing through injection locking [50]. However, two main problems were found with the SFP: 1) The SFP performance proved to be inconsistent over various fabrication runs and in some cases across the same chip, and 2) the SMSR of the filtered comb was limited to 21 dB. This chapter will present the various reflection structures (Pit and V-notch) developed to optimize the consistency and the fabrication yield of the existing single mode lasers based on slots. In the first section, the SFP lasers mode of operation will be discussed. This section will also highlight the slot limitation that motivated the development of the pit and the V-notch. The next two sub-sections will introduce the Pit and V-notch reflection structures developed to overcome the depth sensitivity of the slot. Moreover, the aforementioned sections will also present laser cavities fabricated using these novel structures and how they can be used to replace a cleaved facet. The last 2 sections will discuss the comb de-multiplexing using the SFP and lasers based on the new reflection structures, based on the measured SMSR of the filtered comb. Finally, a theoretical analysis shows the relation between the SMSR and the Q-factor of the cavity and the possible ways to overcome the poor SMSR of the unwanted comb lines.

3.1.1 Slotted Fabry Perot lasers

The main, single mode and tunable semiconductor laser used in the group is the SFP laser. SFP lasers rely on shallow etched slots to introduce index perturbations along the ridge. These perturbations lead to small reflections that create sub-cavities, which results in longitudinal mode selectivity based on the coupled resonances of the various cavities [52]. Fig.3.1 (a) shows an illustration of a slot and Fig.3.1 (b) shows an SEM image of the slot.

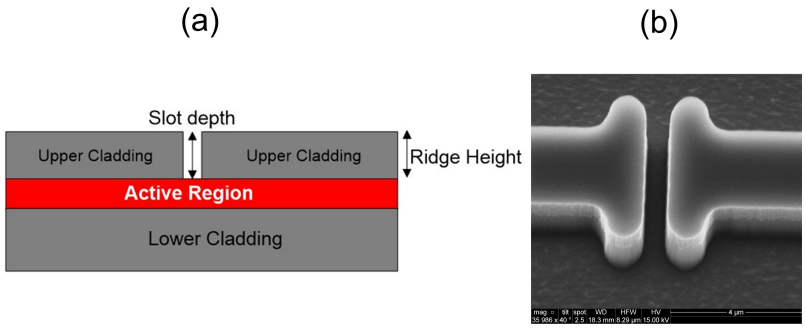


Figure 3.1: (a) Illustration of a shallow slot showing the etch depth of the slot (b) SEM image of the slot

As shown in Fig.3.1 (a) the slot depth stops above the active region. The shallow depth provides small reflections between 1% to 3%, depending on the depth of the etch. The stubs in the SEM image in Fig.3.1 (b) are used to prevent rounding on the etched facet of the slot. Due to its intrinsic nature, the reflection strength of the slot is governed by the depth of the slot. This is because the tail of the mode propagates in the ridge area and the deeper the slot is, the higher the introduced index contrast. Fig.3.2 show a simulation of the reflection, loss and transmission of a slot as a function of the slot depth. Slot sensitivity to depth was also reported in [53].

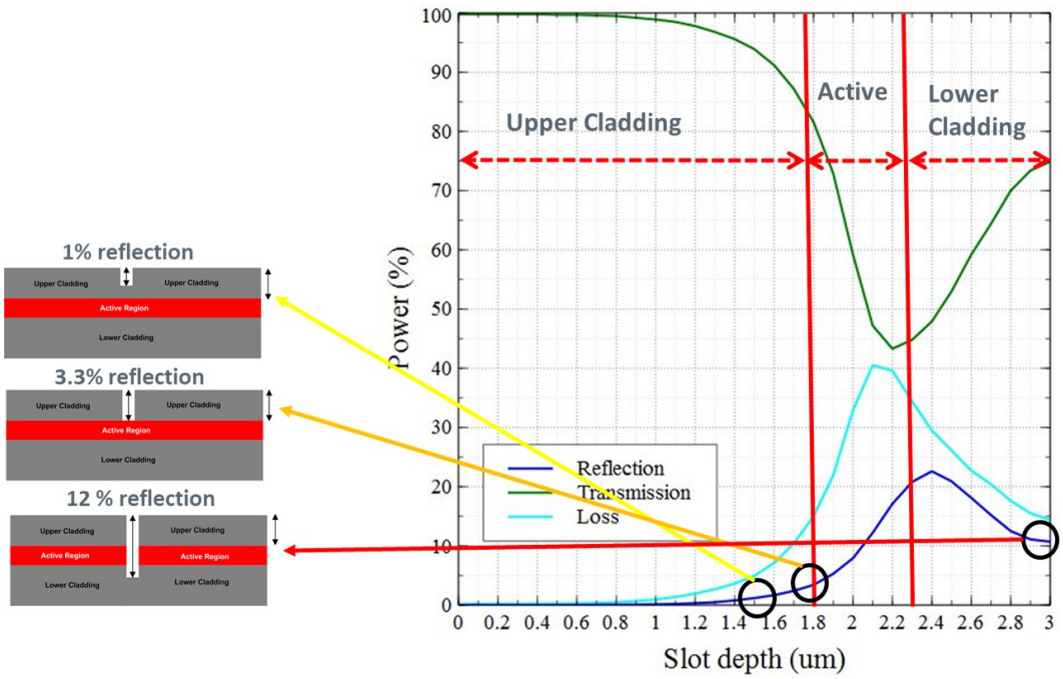


Figure 3.2: Simulation showing reflection, transmission and loss of in function of slot depth

The simulations in Fig.3.2 were obtained using ModePROP from RSoft, a simulation software that employs the Eigenmode expansion (EME) method. This technique is bi-directional in that it takes transmission and reflection into account. As shown in Fig.3.2, the slot reflection and loss show high sensitivity to the etch depth.

An example of possible scenarios is also presented Fig.3.2. Obtaining a 1 % reflection requires and etch depth of around 1.55μm, while reaching 3.3% reflection requires a depth of 1.8 μm. The high sensitivity of the loss and reflection to depth requires an accurate depth control in order for to obtain consistent performance across the chip and therefore to increase the yield.

It is important to note that, although the use of the etch monitor reported in chapter 2 improved the etch depth accuracy, a consistent etch depth across the full chip was still an issue. Depth differences of more that 50 nm were measured between the centre and the edge of the quarter wafer. This depth difference is enough to effect the slot reflection and thus the device performance.

3.1.1.1 SFP for integration

SFP lasers are fabricated by simply introducing slots into a Fabry Pérot (FP) cavity as shown in Fig.3.3



Figure 3.3: cavity with 2 cleaved facets and 3 slots

The SFP laser cavity posses two cleaved facets to provide optical feedback which can limit applications that require monolithic integration. In order to facilitate integration, one of the cleaved facets can be replaced by a slotted mirror made of multiple slots as shown in Fig.3.4.

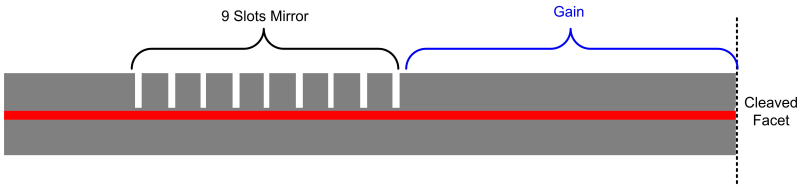


Figure 3.4: single Facet SFP showing the mirror and gain sections

Fig.3.4. show a single facet design with 2 sections. The mirror section which consists of 9 slots is used to replace the cleaved facet and provide optical feedback. The gain section is used to compensate the losses in the cavity, and an example of the single facet SFP optical spectrum is shown in Fig.3.5.

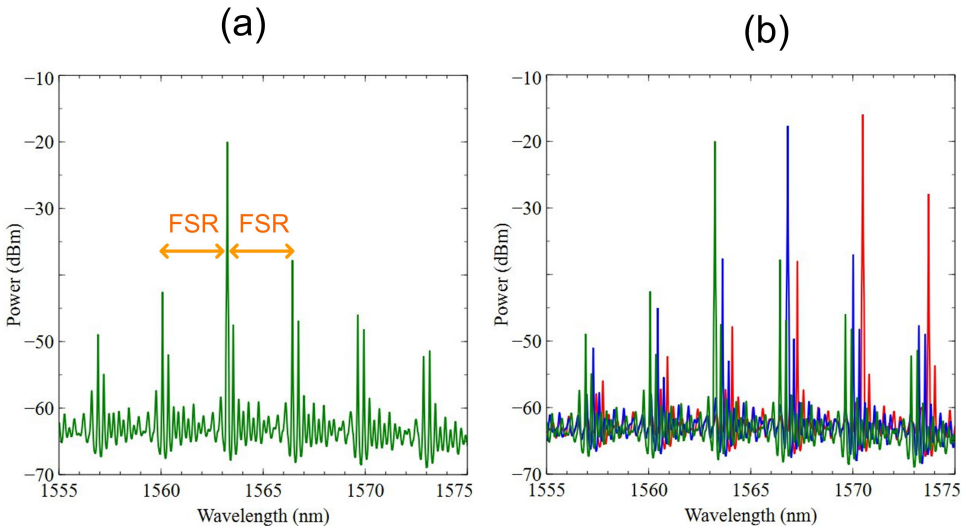


Figure 3.5: (a) spectrum of the single facet SFP showing the FSR that corresponds to the slots spacing, (b) overlapping spectrum showing the SFP tunabiltiy

The free spectral range (FSR) shown between the main cavity modes is determined by the spacing between the slots. The resonance between the slots creates sub-cavities with an FSR that correspond to their spacing, which also provide extra feedback leading to a lower threshold gain at these wavelengths. In this case the slots are spaced at 107 μm to provide a tuning of 400 GHz following the ITU grid standard. The laser can be tuned by increasing the injected current, which alters the temperature of the active region, shifting the location of the gain peak and leading to mode hopping as shown in Fig.3.5 (b). The SMSR can also be optimized by finely changing the injection current to suppress the side modes.

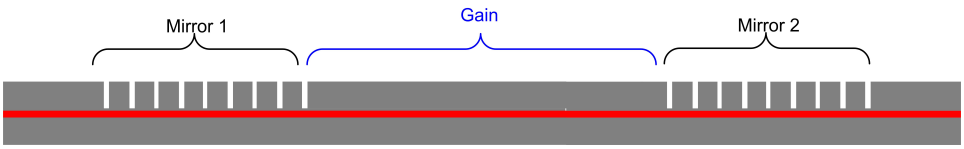


Figure 3.6: Three section facetless SFP design the comprise two mirrors and a gain section

The SFP can be made fully facetless as shown in Fig.3.6. Both cleaved facets are replaced by mirrors, and the gain section between the 2 mirrors provides enough gain to create a lasing cavity.

The advantages of using slots to create tunable single mode lasers is that they exhibit low loss, enable tunable output and relatively high SMSR that can

exceed 40 dB in certain cases, and they can replace cleaved facets to allow further integration. Moreover, the SFP lasers do not require high resolution lithography or epitaxial regrowth which leads to a reduction in the process cost and time. On the other hand, the slot sensitivity to depth means the either there is a limitation in term of having consistent laser performance across the chip, or there is an additional process requirement to ensure an accurate etch depth. This issue can be resolved by using a wet chemical etch used in conjunction with an etch stop layer in the material, however chemical etching introduces yet another limitation, a nonuniform side wall etch profile. The next section will discuss in detail the design of a new reflector (the pit) to overcome the slot limitations in order to have a higher yield single mode lasers.

3.1.2 Pit lasers

The pit is a reflection structure that introduces an index perturbation into the cavity. It has a similar method of operation as the slot, however it is not depth sensitive as long as the etch depth goes through the active region. The main motivation for the development of the pits was to overcome the slots sensitivity to depth.

As mentioned in the previous section, the most significant limitation of the slot is that the reflection, loss, and transmission of the slot are exponentially dependent on the slot depth, as previously shown in Fig.3.2, whereas the slot width has little effect [53]. Achieving the same slot depth at each fabrication run, or even across the same chip is not always attainable using plasma etching. Moreover, due to the high sensitivity to depth, inconsistencies in an otherwise identical laser's performance can occur across a wafer. Further more, to better understand the slot sensitivity to depth, a close up images of the slot reflection and loss as a function of depth from the previous simulation in Fig.3.2 are shown in Fig.3.7

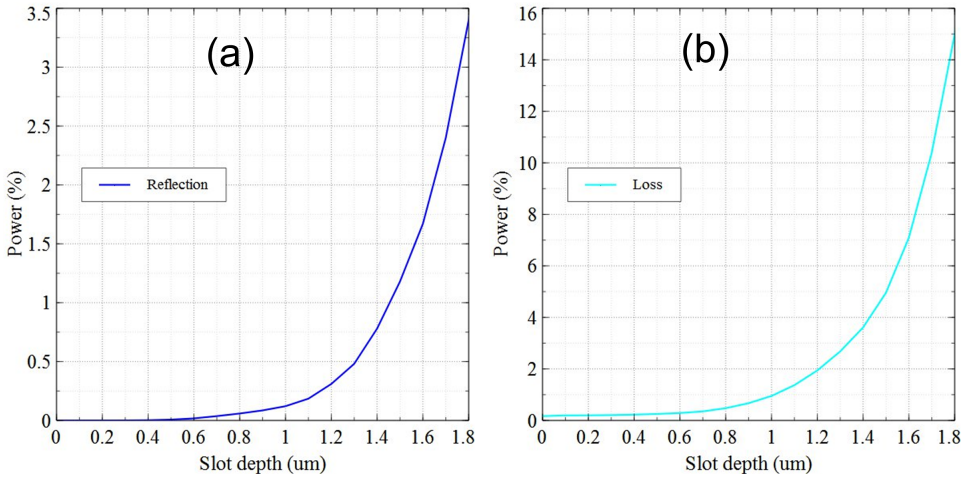


Figure 3.7: Simulation results showing (a) reflection percentage as a function of depth (b) loss percentage as a function of depth

The plot in Fig.3.7 displays reflection and loss as a function of the slot depth with a ridge height of 1.8 μm. Fig.3.7(a) shows the rapid increase of the reflection with varying slot depth, where a slight depth difference as small as 50-100 nm can have a significant effect on the reflection. Fig.3.7(b) shows the loss curve as a function of the etch depth. The power loss is much higher than the reflected power due to scattering losses introduced by the slot, which agrees well with both analytical model presented in [53] and experimental data [54].

This etch depth issue can be addressed by adding an etch stop layer just above the active region and using a wet chemical etch in combination with the dry etch [55, 40]. Although, this method will ensure a consistent depth across the chip with various fabrication runs, it will add complexity to the fabrication process, and restrict the cavity designs on the chip due to the influence of crystal orientation on the chemical etching of InP [56, 57, 58, 59, 60]. The wet etch effects can be seen in the SEM images of Fig.3.8. Fig.3.8(a) shows how the etch outcome can be different for 2 ridges with various orientations. Fig.3.8(b) shows another situation where the chemical etchant creates a non-uniform layer etch pattern.

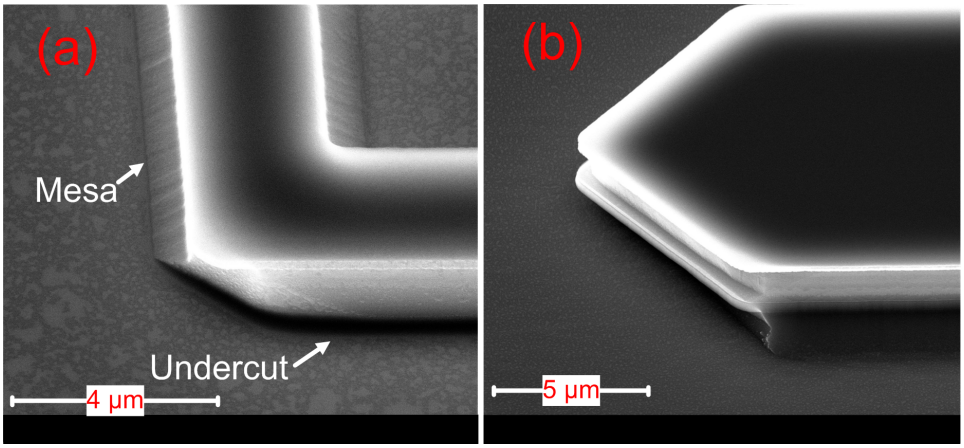


Figure 3.8: (a) effect of wet etch on 2 ridges with different orientation (b) non-uniform layer etching

The deeply etched pit is fabricated using a self-aligned process, as the ridge and the pit are defined in the same lithography layer. An SEM image of the pit is shown in Fig. 3.9.

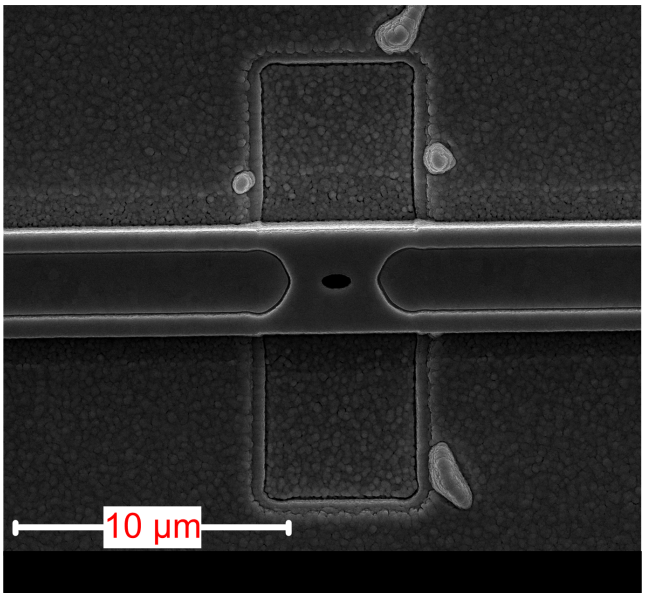


Figure 3.9: SEM image of the Pit reflector showing the pit structure and the deep etch area (rectangle)

Fig.3.9 shows a post-fabrication SEM of the 1μm wide and 1.5μm long pit with ridge oxide opening and deposited metal. The dimensions of the pit were chosen based on the lithography resolution and loss parameters. A pit smaller than 1μm wide and 1μm long is challenging to resolve, and a large pit will introduce higher losses. The rectangle shape surrounding the pit and the ridge is the deep etch region which is defined in another lithography layer as

described in Chapter 2. The process comprises two etch depths, shallow for the ridge and deep for the pit reflector. The two etch depths are illustrated in Fig. 3.10

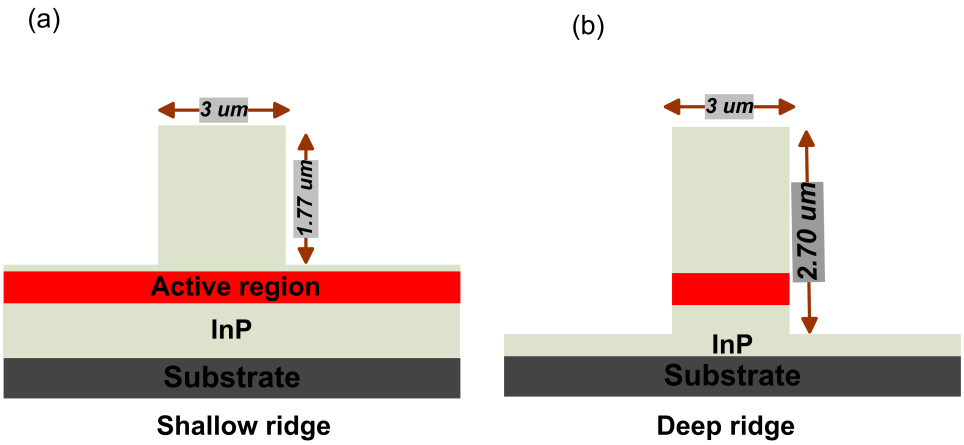


Figure 3.10: (a) shallow ridge, (b) deeply etched ridge

The shallow ridge height is 1.77 μm, and the deep region is 2.7 μm; both shallow and deep ridges have a width of 3 μm. Fig.3.11 shows a cross-section SEM image of the pit obtained by using a focus ion beam etching (FIBE), to ensure that the pit has been etched all the way through the active region. After the semiconductor etch, the pit is filled with 400 nm silicon oxide that is used as a passivation layer.

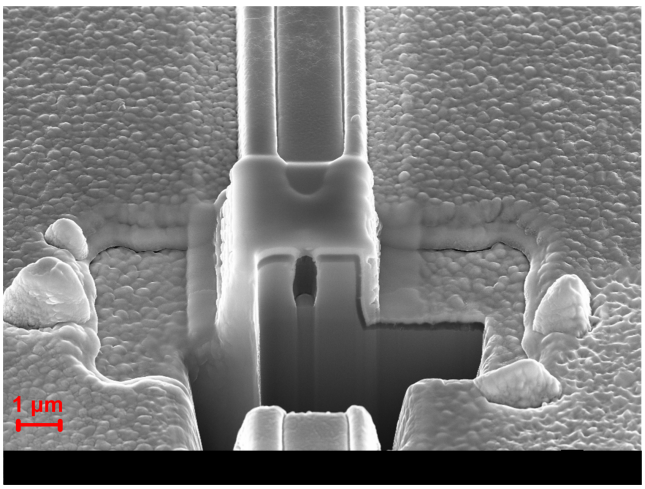


Figure 3.11: Pit cross section obtained using FIBE

To assess the performance of the pit reflector in comparison with a slot, two 1.1 mm long FP cavities were fabricated, one cavity having a slot and another with a pit. Both reflectors were placed 200 μm from the first cleaved facet and

900 μm from the second cleaved facet. The measured Light-Intensity (L-I) curve of both structures is shown in Fig. 3.12

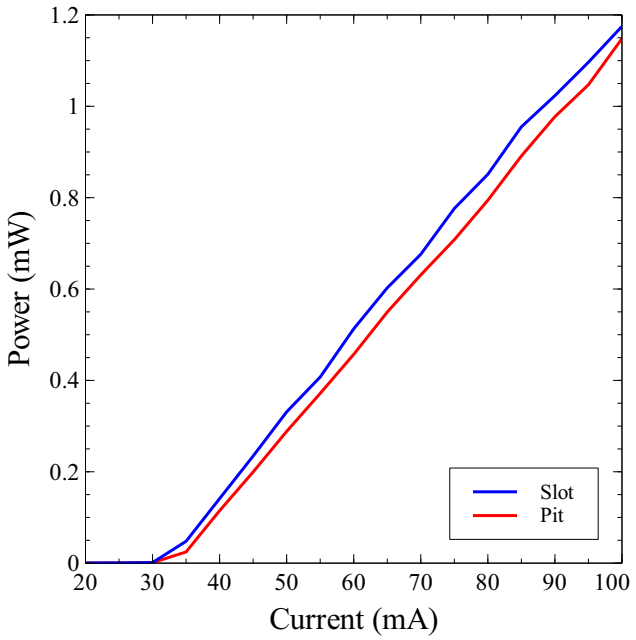


Figure 3.12: L-I curve of 2 cavities with pit(red line) , slot (blue line)

The light was coupled using a lensed fiber while sweeping the current from 0 mA to 100 mA. The pit (red line) and slot (blue line) lasers both lase at around 31 mA with almost identical slope efficiency. The spectrum taken at the lasing threshold for both cavities can be seen in Fig.3.13.

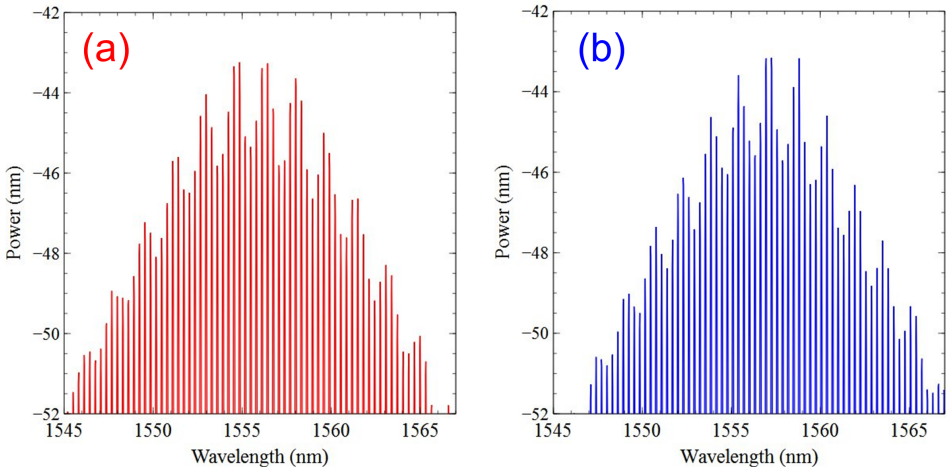


Figure 3.13: Optical spectrum showing the modulation depth cause by reflection (a) cavity with a pit (b) cavity with a slot

The localized reflections from the slot and pit cause a periodic modulation of the optical spectra. The modulation effect on the gain envelope can be clearly

seen in Fig.3.13. Both structures have a comparable spectral behaviour, and modulation depth, which suggests that the reflection of both structures is also comparable. In order to confirm that the reflections were caused by the pits and not by the rectangle deep/shallow waveguide transitions, lasers were made without pits, but with identical rectangle deep/shallow transitions, and no measurable reflections or periodic modulation were seen using the spectral analysis.

A two section laser cavity that comprises four pits was fabricated to demonstrate that the deeply pit etched reflectors works well as a single mode laser. The cavity design is shown in Fig.3.14.

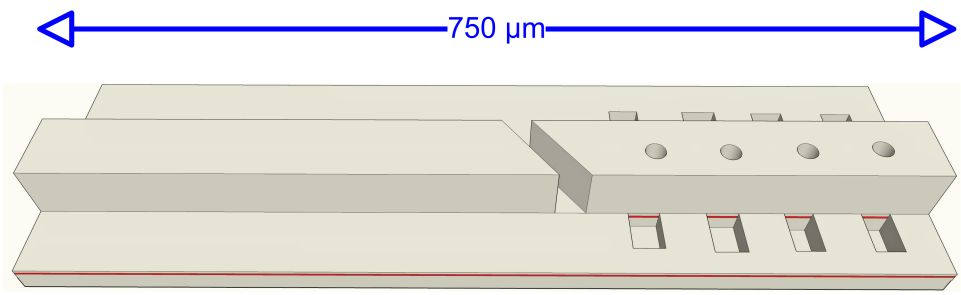


Figure 3.14: Two section laser cavity with four deeply etched pits

Fig. 3.14 show the two section laser with a total length of 750 μm and 4 pits with a pit spacing of 70 μm. A 7° angled slot was used to provide electrical isolation between the two sections. The mirror section is 350 μm long and consists of 4 pits, and the gain section was 400 μm long.

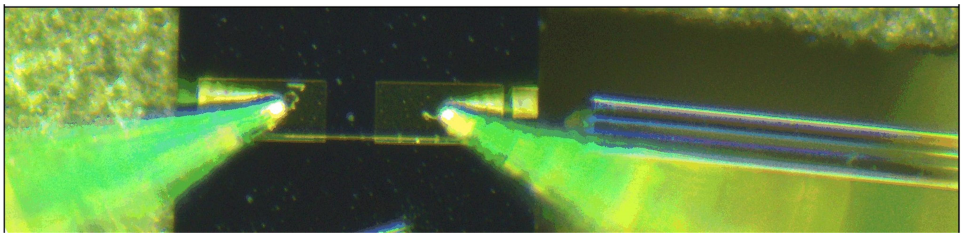


Figure 3.15: Microscope image of the Device under test and showing the two contact probes and a lensed fiber

The microscope image in Fig.3.15 shows the device under test (DUT). Two probes were used to inject current into the individual sections. The optical feedback is provided from the Air/semiconductor interface from the two uncoated cleaved facets. Therefore a lensed fiber was employed to collect the light from the right facet as shown in Fig. 3.15. The laser was mounted on a

temperature controlled brass chuck to ensure thermal stability of the DUT with varying current injection, and the temperature of the chuck was fixed at 20°C.

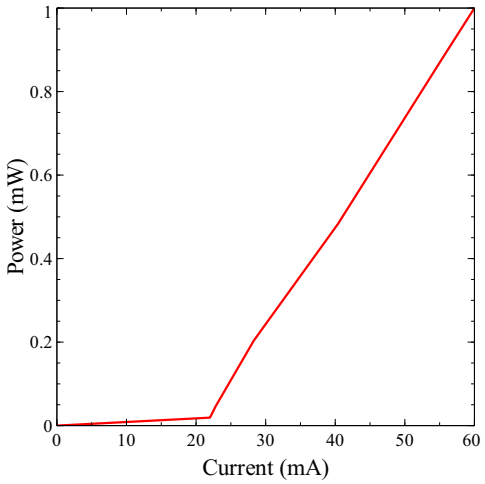


Figure 3.16: L-I curve of the DUT

Fig.3.16 shows the laser L-I curve obtained by biasing the gain section to transparency at 10 mA and sweeping the mirror section from 0 mA to 100 mA. Introducing 4 pits into the cavity increased the lasing threshold by a few milliamps in comparison with a device with no pits. Using a Fast Fourier Transform (FFT) algorithm it was possible to extract the lengths of the resonating sub-cavities in the laser caused from the pits. Fig. 3.17 (a) shows the various resonances between the facets and pits, as well as the resonance between pits. The labels L1 to L4 represents the interaction of the left facet with the various pits and R1 to R4 corresponds the interaction of the pits with the right facet. Also the full cavity and inner pits spacing S is shown.

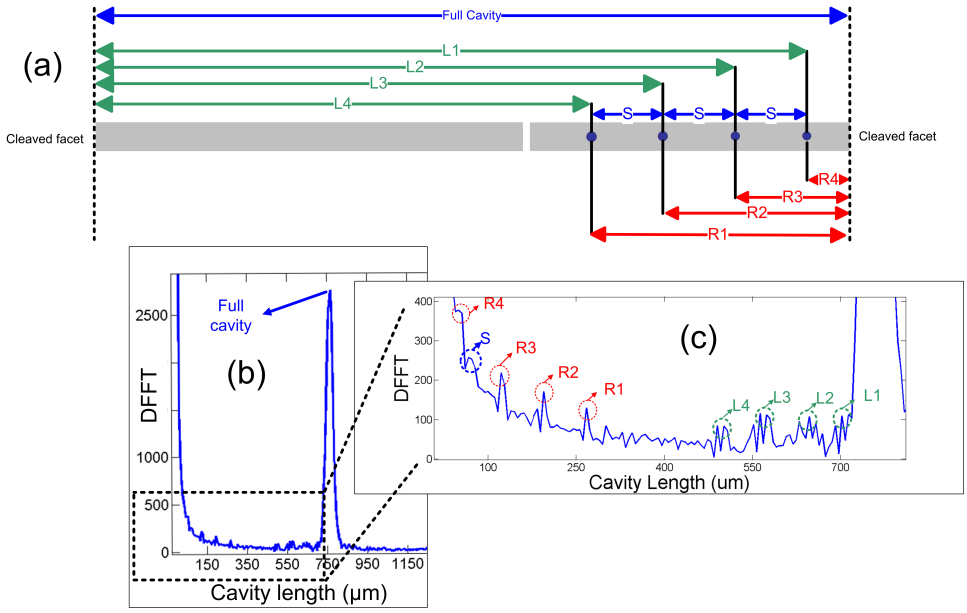


Figure 3.17: (a) Cavity resonance map between the pits and cleaved facets. (b) FFT cavity analysis of the laser spectrum (c) FFT zoom in showing Pits sub-cavities

Fig.3.17 (b) shows the full FFT spectrum that shows a peak at 750 μm, which corresponds to the spacing between the two facets. Fig.3.17(c) is a close up figure of the FFT spectrum in the region where the pits interact with each facet as well as with each other. The labels in Fig.3.17(c) correspond to the physical length of the sub-cavities shown in Fig.3.17 (a), clearly showing reflection from each of the individual pits leading to mode selectivity. The spectrum of the pit laser is shown in Fig.3.18(a) with an SMSR of approximately 40 dB and output power $>$ 2 mW. Fig.3.18(b) shows the 280 kHz laser linewidth, which is the full width at half maximum (FWHM) of the measured spectrum. The measured linewidth was obtained using a delayed self-heterodyne linewidth setup with 50 km fiber delay line in a recirculating loop configuration that has a resolution of $<$ 2 kHz [61].

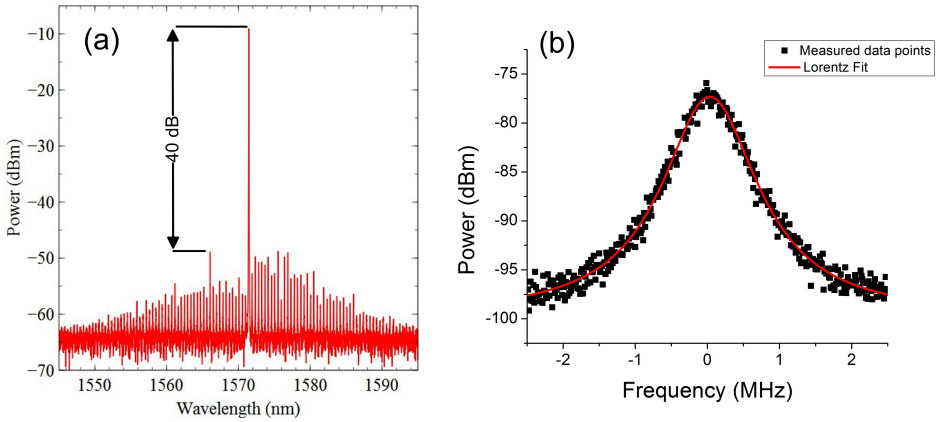


Figure 3.18: (a) laser single mode output with SMSR of 40 dB (b) 280 kHz measured linewidth and lorentz fit

The laser is tunable across 40 nm with an SMSR ranging from 30 dB to 40 dB that extends from 1540 nm to 1590 nm with a step of approximately 5 nm that corresponds to a free spectral range (FSR) of a 70 μm cavity that matches the spacing between the pits. Typically the spacing between the reflectors dominate the tuning of such lasers [34]. The FSR of the pit mirrors dominate the mode hops of the laser cavity as can be clearly seen in Fig. 3.19

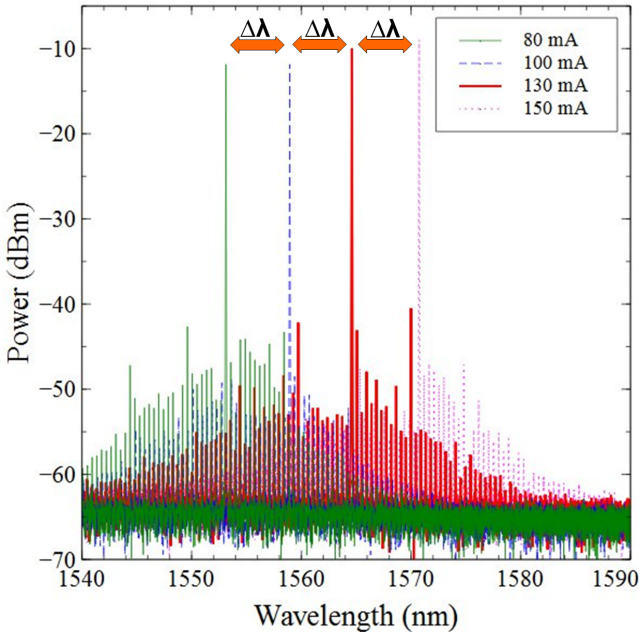


Figure 3.19: single mode tuning with relevant injected current showing 4 channels with a with $\Delta\lambda$ step of 5 nm

Fig.3.19 shows a sample of the tuning of the laser with 4 wavelength with a step of $\Delta\lambda$ which is $\approx$ 5 nm corresponding to the pit mirrors FSR. In this

example, by increasing the total injected current from 80 mA to 150 mA the laser is tuned while maintaining an SMSR between 30 and 40 dB across all wavelengths.

The full tuning map for the pit laser with the corresponding mirror and gain current is shown in Fig.3.20

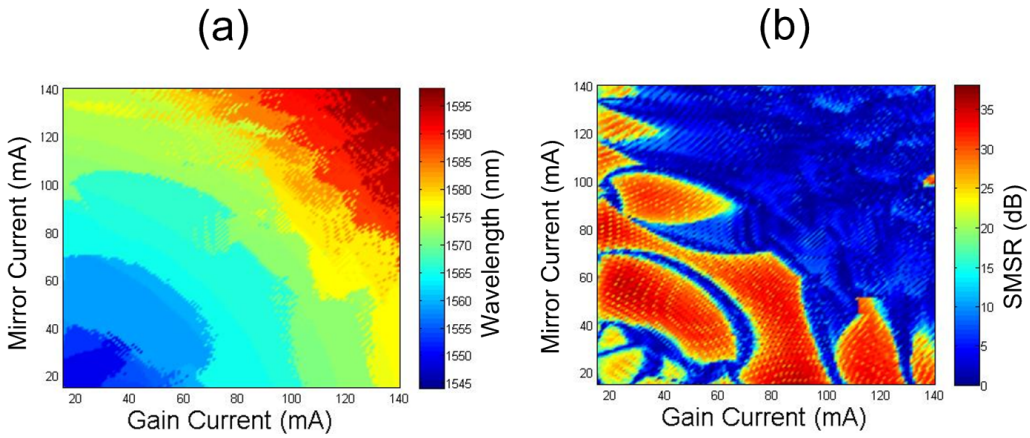


Figure 3.20: color tuning map of (a) wavelength in function of gain and mirror current (b) SMSR in function of gain and mirror current

The color map in Fig. 3.20(a) shows the wavelength region as a function of the varying current in the mirror section and the gain section. Whereas Fig. 3.20(b) shows the SMSR values as a function of the current through the gain and the mirror sections. The red areas show the region where the SMSR is >30 dB, and the blue region is where the laser operates mostly multimode. As shown in Fig. 3.20 the laser can achieve an SMSR between 30 dB and 40 dB for wavelengths extending over more than a 30 nm tuning range.

3.1.2.1 Single facet pit laser

At this stage the pit has proven to be an effective alternative to the slot in the creation of single mode lasers. The next step is to replace one of the cleaved facets with a pit mirror, to demonstrate that the device is suitable for integration. Therefore, a new laser cavity was designed.

The laser consists of 3 sections for: gain, internal mirror, and absorption. The sections are electrically isolated using two shallow slots with a 7° angle to minimize reflections. An illustration of the laser design is shown in Fig.3.21.

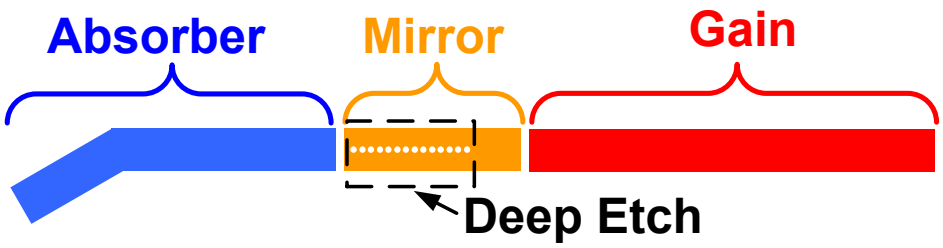


Figure 3.21: Schematic of the three section laser design that consist of an absorber, mirror and a gain section .

The gain section shown in Fig.3.21 (red) is 600 μm long, and it is positioned between the mirror and a cleaved facet. The mirror section comprises 20, 25 or 30 deeply etched pits with a periodic spacing of 6 μm between the centers of the adjacent pits. The pits are deeply etched through the quantum wells, having one deep etch region extending over the pits. Similar to a shallow slot in a SFP laser, each pit produces a small reflection estimated at approximately 1-2% which then creates multiple sub-cavities. The multiple adjacent pits then generate enough optical feedback to form a mirror. All variants of the laser worked well, however the 30-pit version generated the highest output power as well as the highest SMSR. Finally, the last part of the laser consists of a waveguide section with an angled cleaved facet (blue). As shown in Fig.3.21 this part is labeled as absorber and its mainly used as a light absorber while reverse biased. When un-biased the angled facet can be used to collect light from the laser cavity, by exploiting optical bleaching in the unpumped waveguide due to light from the laser. The angled facet significantly reduces the reflections from the semiconductor/air interface so it would not interfere with the main cavity. In this work no high reflection (HR) or anti-reflection (AR) coatings were used.

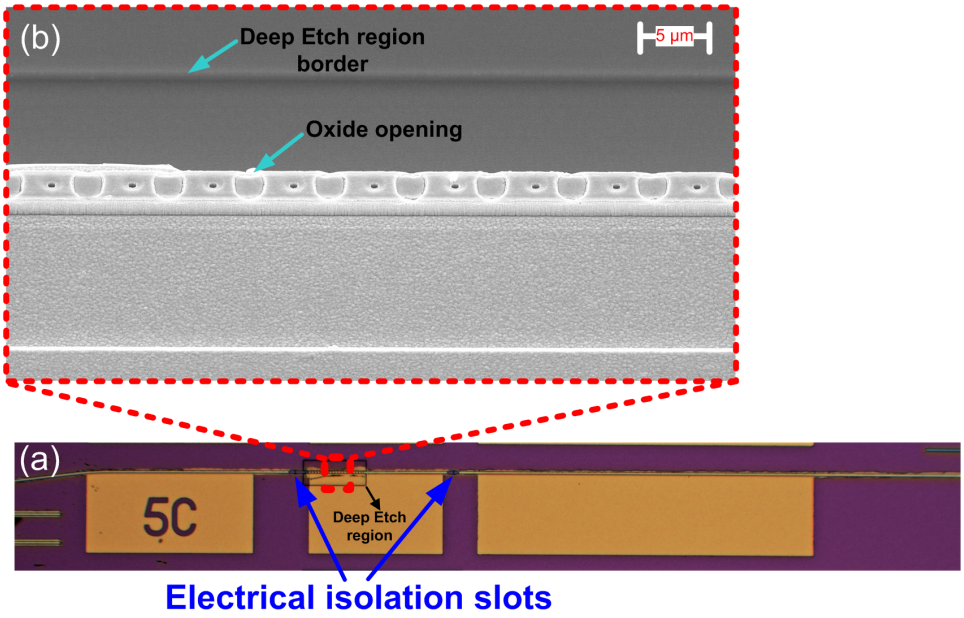


Figure 3.22: (a) microscope image, (b) SEM image of the pit mirror. Note that the larger circles between the pits are openings in the oxide to allow metal contacts with the ridge.

Fig.3.22(a) shows a microscope image of the three-section laser, and highlights the deep etch region surrounding the pits and the two isolation slots that divide the cavity into three electrically isolated sections. Fig.3.22(b) displays a scanning electron microscope (SEM) image of a slice of the pit mirror.

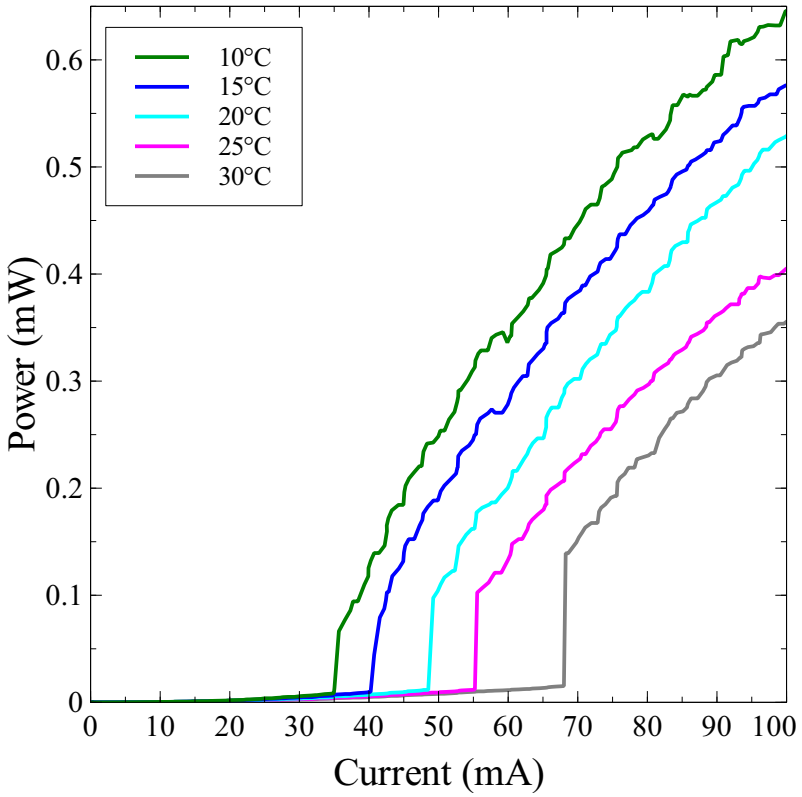


Figure 3.23: L-I plot for different temperatures.The noise in data is caused by vibrations of the lensed fibre during data collection.

The laser was mounted on a temperature controlled brass chuck, and the light was collected from the straight cleaved facet via a lensed fiber. In order to characterize the laser performance, the light-intensity (L-I) curve of the laser was taken at various temperatures as shown in Fig.3.23.

The L-I curves in Fig.3.23 show a typical threshold trend of semiconductor lasers, which cause the laser threshold current to rise exponentially with temperature. The threshold-temperature dependency is mainly due to the rise of intrinsic losses in the active region at higher temperatures, which decrease the laser internal efficiency. The plots were taken by injecting 20 mA in the mirror section and sweeping the gain from 0 to 100 mA. Moreover, in order to make sure that the mirror is solely providing optical feedback without the help of the second facet, the absorber section of the laser was reverse biased to -3V to absorb all the residual light. The laser lased in a single mode with an SMSR of 37 dB and a linewidth of 450 kHz as shown in Fig.3.24.

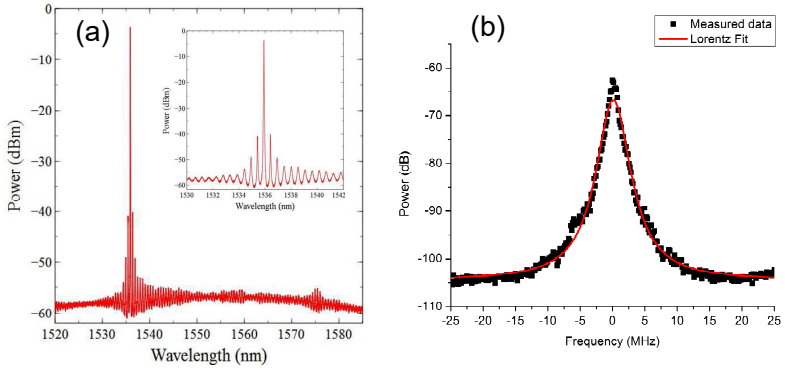


Figure 3.24: (a) spectrum with 37 dB SMSR , Inset shows a close up image of the spectrum (b) linewidth measurement with Lorentz fit.

Fig.3.24(a) shows the spectrum of the laser with peak wavelength at around 1535 nm with an SMSR of 37 dB. The inset in Fig.3.24(a) is a close up image of the single mode. Fig.3.24.(b) shows the 900 kHz full width at half maximum (FWHM) of the measured electrical spectrum, which corresponds to a 450 kHz linewidth of the laser. Moreover, to further confirm the operation of the pit mirror, a fast Fourier transform (FFT) cavity analysis on the optical spectrum was performed. Fig.3.25.(a) show the cavity analysis based on the optical spectrum at lasing threshold (shown in Fig.3.25.(b)).

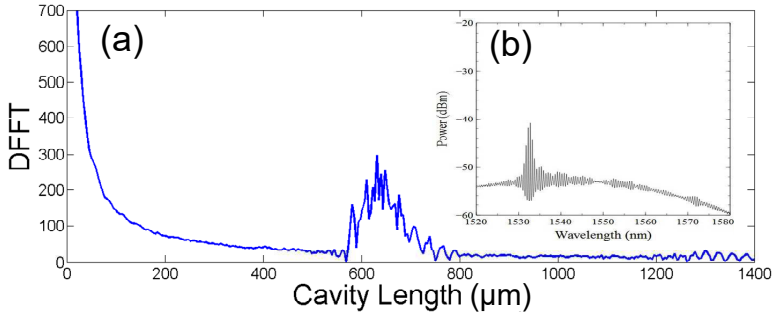


Figure 3.25: (a) the cavity FFT spectrum showing resonance only at the pit mirror location (b) laser spectrum at threshold.

The multiple peaks shown in the FFT as seen in Fig.3.25(a) represent the length of the sub-cavities created between the facet and each of the pits. No additional peaks can be seen at the full cavity length between the two facets at 1100 μm, proving that the absorbing section has fully isolated the cleaved angled facet from the lasing cavity.

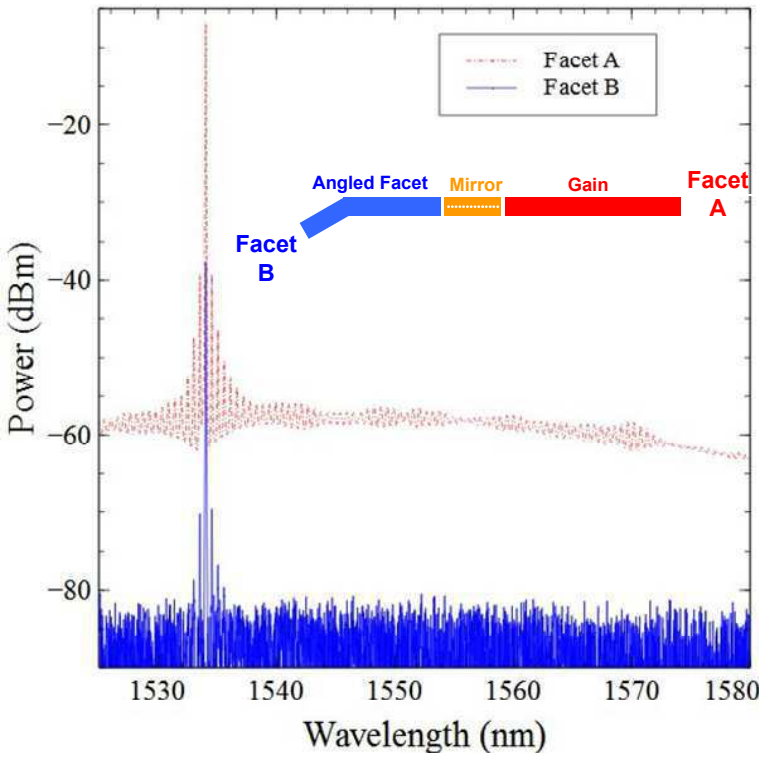


Figure 3.26: the spectrum of the laser from the straight facet (red) and angled facet (blue).

Fig.3.26 shows the overlap spectrum of the coherent outputs of the laser from both facets. The red spectrum is taken from the straight facet A, and the blue spectrum is taken from the angled facet B. The power taken from the left facet B is lower due to the low coupling efficiency between the angled facet and the lensed fiber and also due to the optical loss in this un-biased absorber section. However, the main purpose of facet B is to demonstrate that the laser can be integrated with other photonics components. Although, the demonstrated higher order DBR in this work uses a single cleaved facet, this cleaved facet can be easily replaced by a broad-band reflector such as a multimode interference reflector (MIR)[62], or a metal coated etched facet [63]. By doing so, the laser could be freely positioned anywhere on the chip to be used as a facetless laser. The single mode output can be tuned across 2.9 nm by increasing the injected current, while the SMSR is maintained above 30dB over the tuning range. An overlap of the tuning spectrum is shown in Fig.3.27.

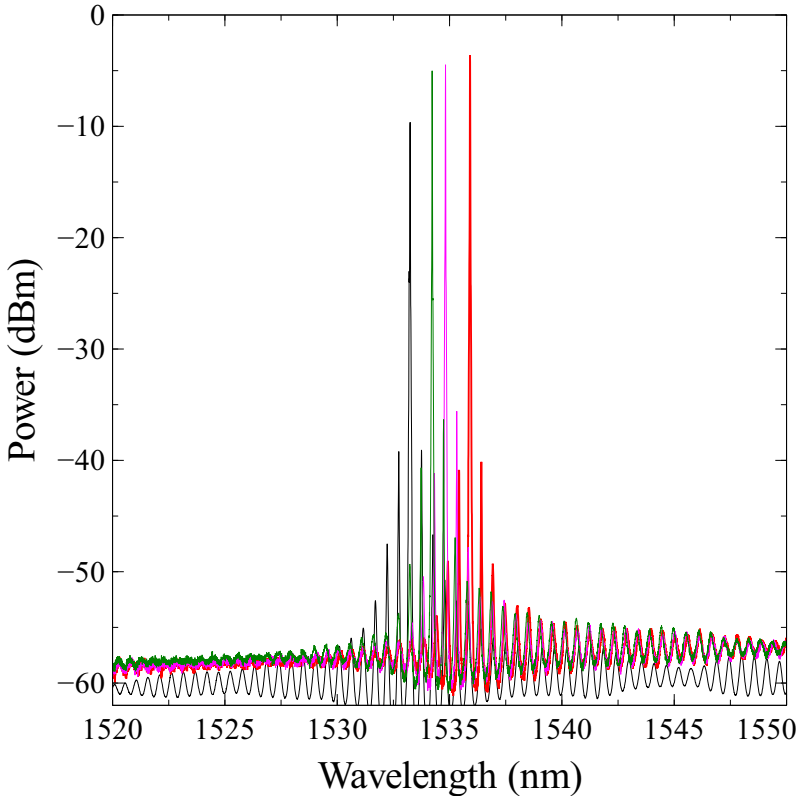


Figure 3.27: Tuning across 2.9 nm by increasing the injected current.

The wavelength selective reflection of the mirror section was modeled using transfer matrix method (TMM) technique, as described previously [28]. Each pit was taken to be a scattering point, and assumed to reflect $\sim$ 3% of intensity while inducing a 15% loss. The reflection from facet A was taken to be 30%. Facet B was presumed not to contribute to the reflection, as the reverse biased section prior to facet B absorbed all the light traveling to and from the facet. This claim is supported by the lack of a facet to facet resonance in Fig.3.25(a). The transmission matrices for each scattering section i were of the form:

$$T_{Scat} = \frac{1}{t_i}\begin{pmatrix} 1 & -r_i \\ -r_i & 1 \end{pmatrix} \tag{3.1}$$

The field inside the device propagates as $e^{j\beta L}$, where L defines the propagation length, and β is the propagation constant. The distance between the scattering points caused by the pits was taken to be 6.0 μm (the distance from the center of one pit to the next), with the group index of the material assumed to be

3.45. The transmission matrices for the propagation sections were of the form:

$$T_{Prop} = \begin{pmatrix} e^{j\beta L_i} & 0 \\ 0 & e^{-j\beta L_i} \end{pmatrix} \tag{3.2}$$

Taking products of T_{Scat} and T_{Prop}, the resonant wavelengths of the device were calculated numerically. In Fig.3.28(a), the resonance of the device is plotted on top of the measured spectrum. The positions of the lasing modes of the device were found to be accurately described by the transmission matrix model. At 1593nm, the small rise of noise far from the gain peak is matched by the increase in reflection from the pit mirror section predicted by the model. Fig.3.28(b) demonstrates how the lasing wavelength can be controlled by changing the spacing between the pits. The graph shows various pit spacing between 3 μm and 6 μm and the resulting resonant wavelengths. Based on the data provided Fig.3.28(b) designing it is possible to design a cavity with predetermined wavelength.

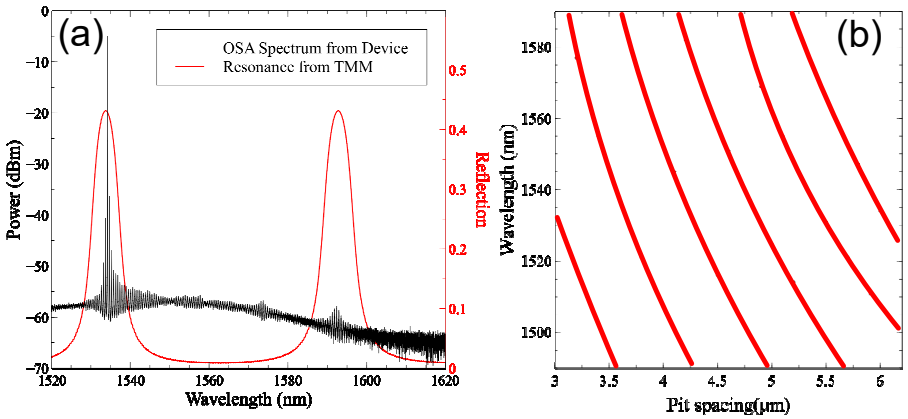


Figure 3.28: a) Simulated resonance of the laser cavity compared with the experimental spectrum of the laser (b) lasing wavelength with various pit spacing.

The pits showed a good consistency across the chip and within various fabrication runs in term of overall laser performance. Fabricated devices with the same parameters from different fabrication runs have shown similar wavelength and threshold behaviour. The reflection strength from the pit is not tunable, for example getting a reflection above 2% or 3% is not feasible due to the size of the pit in relation to ridge. Having the ability to control the reflections could be of interest, so that for example the device could be made more compact. The next section will present novel tunable reflectors based on V-notches, which can have variable reflection strengths.

3.1.3 V-notch

This subsection will present the V-notch, a geometrically controlled tunable reflector. Similar to the pit, the V-notch is deeply etched through the active region. However, due its design the reflection from the V-notch can be controlled.

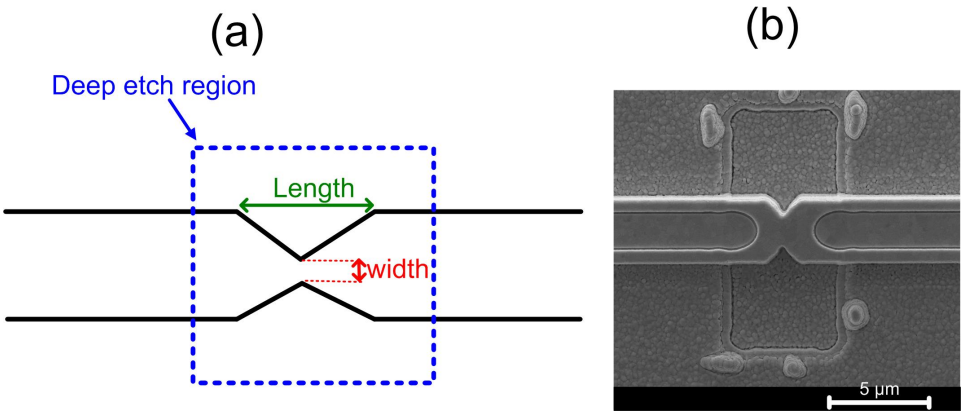


Figure 3.29: a) V-notch illustration showing the length, and width of the structure (b) SEM image of the V-notch.

Fig.3.29 (a) shows an illustration of the V-notch, where the deeply etched region is inside the blue box. The 2 dimensions labeled length and width are the parameters that define the V-notch. The reflection strength can be manipulated by changing the width. Fig.3.29 (b) shows an SEM image of a fabricated ridge with a V-notch.

Fig.3.30(a) shows an illustration of the design of the deeply etched V shape structures. The red color represents the active region, where the ridge and the cladding layers are in grey. Fig.3.30(b) shows a side view SEM image that includes the deeply etched ridge. The opening on the top of the ridge is the oxide window for the metal contact layer. The roughness on the floor is also due to the metal deposition.

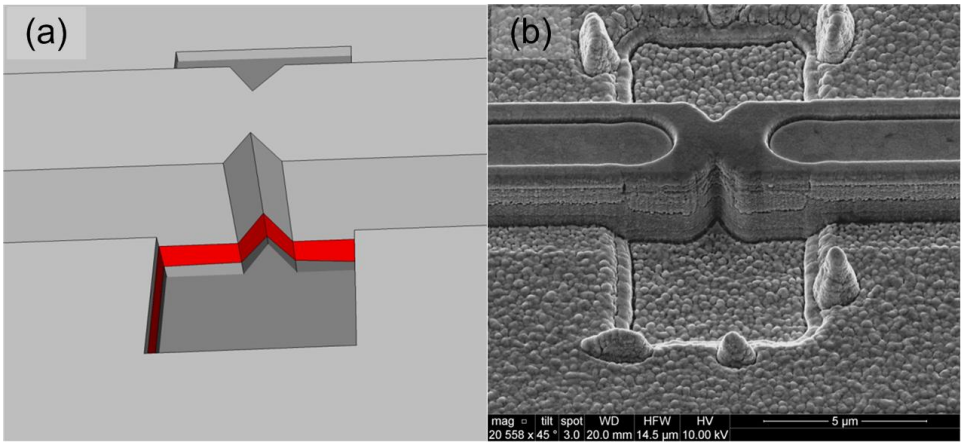


Figure 3.30: (a)Illustration of the etch depth, the red color represent the active region (b) SEM image showing the deep etch region.

Fig.3.31 shows a close up SEM image of the reflector with the dimensions of the structure.

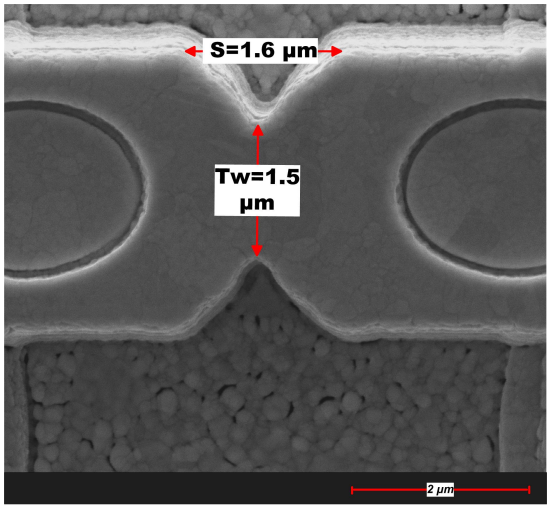


Figure 3.31: SEM image of the V-notch with dimensions.

The original width of the waveguide was 2.5 μm. Tw is the tapered width (1.2 μm) and S represents the taper length needed to form the V-notch reflector. Moreover, it is possible to include in the same cavity different V-notch reflectors with different parameters without adding any steps because S and Tw are defined in the same lithography step as the ridge. The flexibility can be considered as an advantage compared to slots, where the etch depth plays a critical role in controlling the reflections and loss. Due the intrinsic design of the slot, it is not possible to include slots with different depths on the same cavity without additional fabrication steps.

To analyse the reflections and losses of the V-notch, a 3D module of the epitaxial layers with a single V-notch was simulated using the commercial software: ModePROP from RSoft. Fig.3.32 shows the reflection, loss and transmission for the slot and for the V-notch with a ridge height of 1.8 μm. Fig.3.32(a) shows the simulation of the slot and demonstrates how the reflection is depth controlled. Fig.3.32(b) shows the V-notch simulation and how in contrast the reflection is lithographically controlled by varying the taper width Tw from 0.5 μm to 2.5 μm.

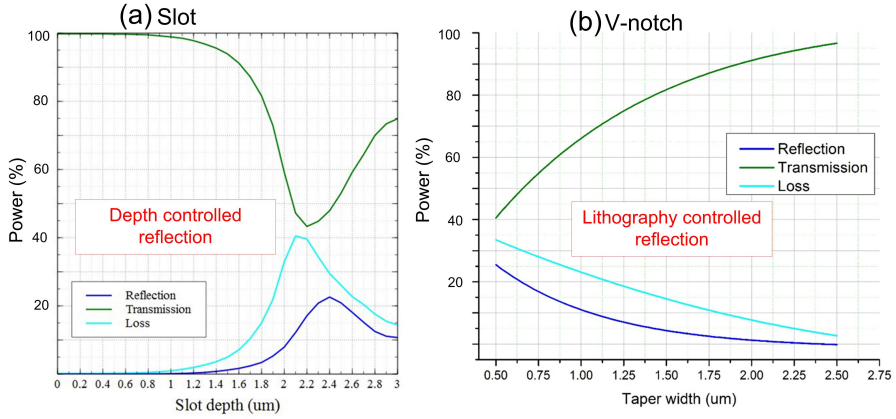


Figure 3.32: Simulation results of reflection, loss and transmission for (a) slot depth variation, (b) V-notch taper width variation.

In Fig.3.32(b), the simulation shows a linear relation between loss and reflection governed by the taper width. An increase in reflection will also result in an increase in the loss and consequently reduce the transmission. A trade-off between reflection and loss is observed.

To verify the operation of the V-notch reflectors, three FP laser cavities were fabricated. All three FP lasers had the same length of 1.1 mm but each included a single V-notch with a different taper width Tw. The simulation graph in Fig.3.33(a) shows the reflection curve (blue line), and Fig.3.33(b1),(b2) and (b3) shows the experimental spectral data from the V-notches with taper widths 0.75 μm, 1.2 μm and 1.7 μm respectively. Fig.3.33(c1),(c2) and (c3) show the simulated reflection of the V-notch at the corresponding reflection power for each taper width. The simulated reflection does not take gain into account. Hence the flat response. The periodic modulation depth of the optical spectra caused by the V-notch increases with the decrease of the taper width. The experimental data agrees well with the

simulation, which confirms that the reflection strength increases with a decrease in taper width.

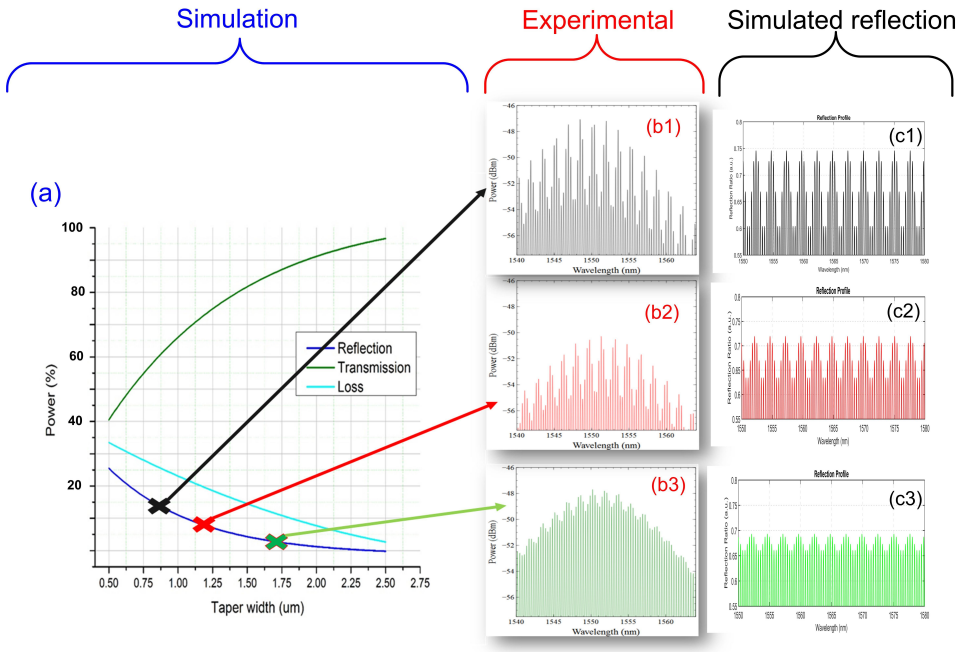


Figure 3.33: (a) V-notch simulation results showing reflection(blue), loss(cyan) and transmission(green), (b1) to (b3) experimental spectrum at various V-notch taper width, (c1) to (c3) simulated reflection spectrum at various V-notch taper width.

The deep etched V-notch is not depth sensitive, however the deep etch also serves to obtain a strong reflection. Moreover, Fig.3.33 shows a trade-off between reflection and transmission, which means the V-notch number and dimension should be taken into consideration when designing a laser cavity. The next subsection demonstrates a single facet laser cavity that consists of 4 V-notch reflectors monolithically integrated with a multimode interference reflector (MIR) used to replace a cleaved facet. MIRs have been developed to allow mid-chip integration of mirrors to replace cleaved facets [62]. This makes them a valuable integration tool and a potentially important building block for InP-based Photonic integrated circuits (PICs). The active MIR has a length of 25 μm and width of 5 μm, and uses the same epitaxy as the laser, thus avoiding the need for epitaxial regrowth [31].

3.1.3.1 single facet V-notch lasers

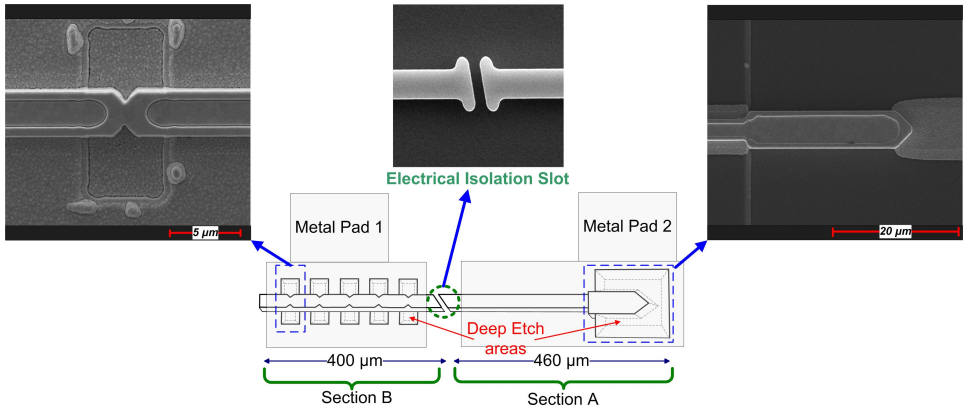


Figure 3.34: Illustration of the two-section Laser cavity design along with SEM images of the V-notch, isolation slot and MIR.

The schematic in Fig.3.34 shows the two section laser design, along with scanning electron microscope (SEM) images of the V-notch reflector on the top left and MIR on the top right. The total length of the cavity is 880 μm. The laser consists of two sections (A and B) separated by an angled slot to provide electrical isolation between the two contact pads. Section A of the laser has a length of 460 μm and it is made up of an MIR and a waveguide section. The structure uses a deep etch that extends through the active region and lower cladding to ensure strong light confinement, which maximizes the reflected power back into the cavity. The design of the MIR is similar to a 1×2 multimode interference coupler terminated with a reflector made up of 45 $^\circ$ angled mirrors. The incident light is reflected at the angled facet and back into the waveguide due to total internal reflection. The active MIR design and fabrication process is similar to the reflector reported in [31]. Although theoretically the MIR should reflect back nearly 100% of the light, it has been shown that it suffers from more loss than expected.

Nonetheless, when optimized, it is still a convenient solution to replace cleaved facets because it allows a flexible positioning of the laser on the chip. Section B of the laser consists of the wavelength selective mirror. This section is 400 μm long and contains five 80 μm equally spaced V-shaped partial reflectors. The reflected light resonates between the V-notch structures and with both the MIR and the cleaved facet, creating a coupled cavity laser. The reflectors are deeply etched through the quantum wells in order to ensure effective and reproducible reflections. The reflectors were etched in the same process as the MIR, so no additional processing was required.

The laser was mounted on a brass chuck that was temperature controlled using a thermal electric cooler (TEC). A lensed fiber was used on the cleaved facet side to collect the light and inspect the spectrum and optical power. Two separate current sources were utilized to inject current into the laser. Fig.3.35 shows the optical spectrum of the laser, with a single mode emission at 1557.5nm and an SMSR of 37 dB. The free spectral range of the V shape reflectors can be visibly distinguished on the lasing output. The measured spacing of 4.6nm between the main mode and the adjacent side modes corresponds to an 80μm cavity length which is the spacing between the V-notch structures.

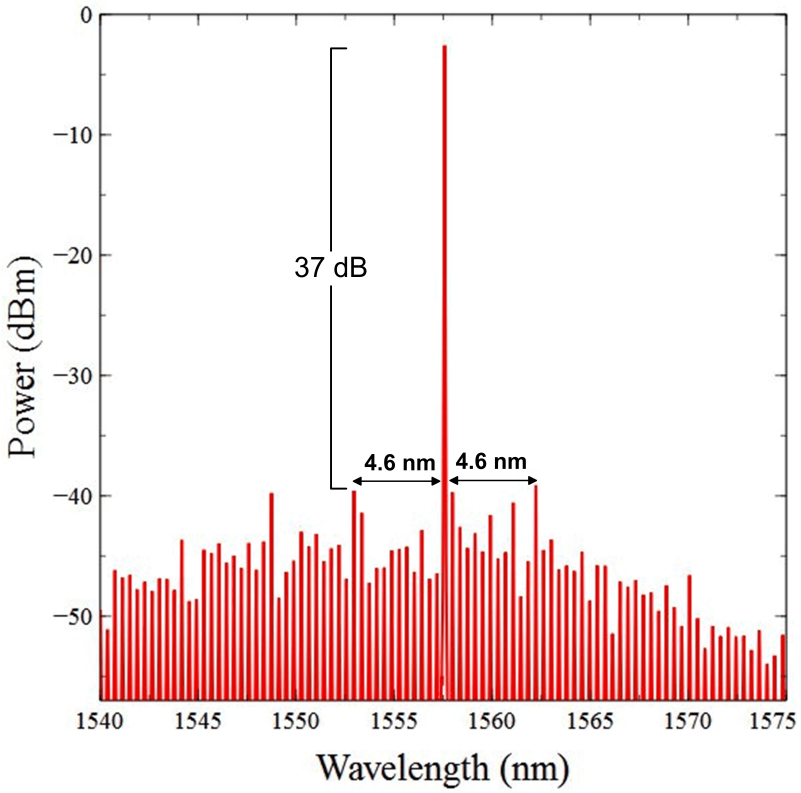


Figure 3.35: Laser optical output with 37 dB SMSR and the mode FSR based on the V-notches spacing

By employing the fast Fourier transform (FFT) algorithm described previously, it was possible to extract the effective lengths of the coupled cavities from the optical spectrum of the laser at threshold. As Fig.3.36 shows, the FFT analysis of the optical spectrum agreed with the effective physical length of the coupled cavities.

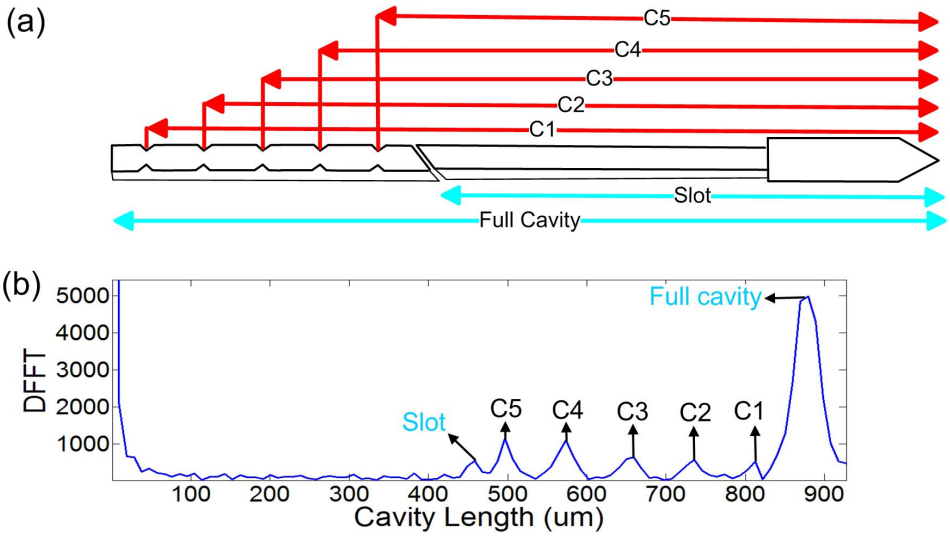


Figure 3.36: (a)Laser design with highlighted cavities, (b) FFT analysis showing the full cavity and sub-cavities created from reflections

The FFT analysis shows the actual cavities effective lengths based on the FSR of the laser modes. The five peaks in Fig.3.36(b) labeled from C1 to C5 correspond to the physical lengths shown on the laser design in Fig.3.36(a). The large reflection peak on the right of C1 represents the full laser cavity length extending from the MIR to the cleaved facet. Whereas the small peak just before C5 is the small unintentional reflection caused by the isolation slot.

The single mode output can be continuously tuned thermally with small changes in applied bias, or it can be discretely tuned using larger bias steps, which result in mode hopping. Fig.3.37 shows the 2 tuning options. The thermal tuning led to a red shift around 20 pm /1 mA covering 1.5 nm before hopping to the next mode as shown in Fig.3.37(a). Whereas, Fig.3.37(b) shows the wide tuning range of the laser that can cover around 12.5 nm.

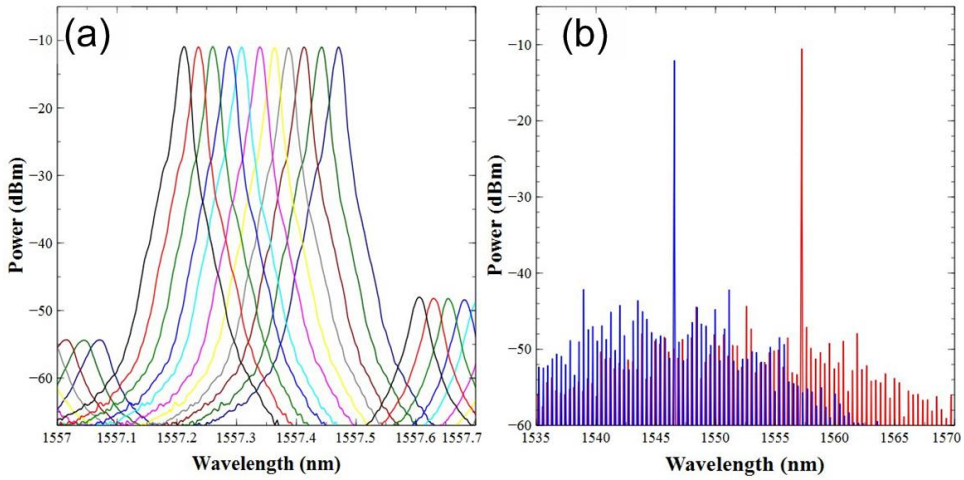


Figure 3.37: Tuning by increasing the injected current(a) Fine tuning,(b) wide tuning.

Summary

The new reflection structures: the pit and the V-notch overcame the slot limitation by showing that they can create small reflections without accurate depth control. Moreover, they also eliminate the need to use chemical etching, which allows cavities to be designed with different orientations without worrying about the etch profile. Also, both structures are compatible with deep etch ridges. Using these novel structures it's possible to increase the yield of the fabricated devices and reduce fabrication complexity. The next section will discuss the comb filtering setup and experiment and look into if cavities with pits and V-notches will improve the SMSR of the filtered comb.

3.1.4 Comb de-multiplexing and linear cavities Q-factor

This section will discuss the comb de-multiplexing experimental setup and present a sample of the results, showing the spectrum of the comb sweeping across the slave lasers. Fig.3.38 show the experimental setup used in this work to perform the injection locking experiment.

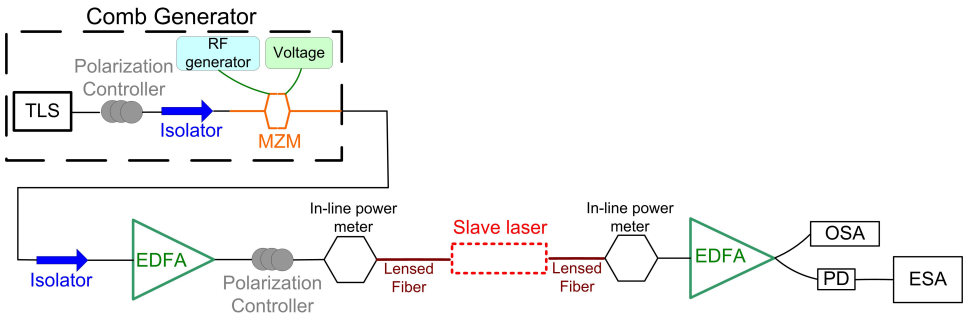


Figure 3.38: Experimental setup of the injection locking experiment

A coherent comb was generated by modulating a MZM with a sine wave as shown in the dashed box in Fig.3.38. A tunable laser source (TLS) is fed into the Mach Zehnder modulator (MZM) via a polarization controller (PC) and an isolator. The MZM is connected to an RF generator and to a power supply for a DC bias. The RF generator controls the comb spacing, whereas the power supply controls the bias point of the MZM, which gives the ability to control the flatness of the lines and to suppress the carrier if needed.

The generated comb is then coupled to an erbium doped fiber amplifier (EDFA) via an optical isolator. The EDFA, designed to operate in both the C and L bands is used to boost the signal. The second isolator is used to prevent the backward amplified spontaneous emission (ASE) of the EDFA from coupling into the MZM. Next, the output of the EDFA is connected to a polarisation controller (PC) and in-line power meter before being coupled to the slave laser via a lensed fibre. The output of the slave laser is coupled to another lensed fibre and then to a second in-line power meter. The in-line power meters are used to monitor the power in real time while the experiment is running to observe any drift in the coupling power. Next the output of the in-line power meter is connected to another EDFA. Finally, the EDFA output is connected to an optical spectrum analyzer (OSA) and electrical spectrum analyzer (ESA) via a high speed photo-diode (PD).

An example of a comb filtering sweep in shown in Fig.3.39.

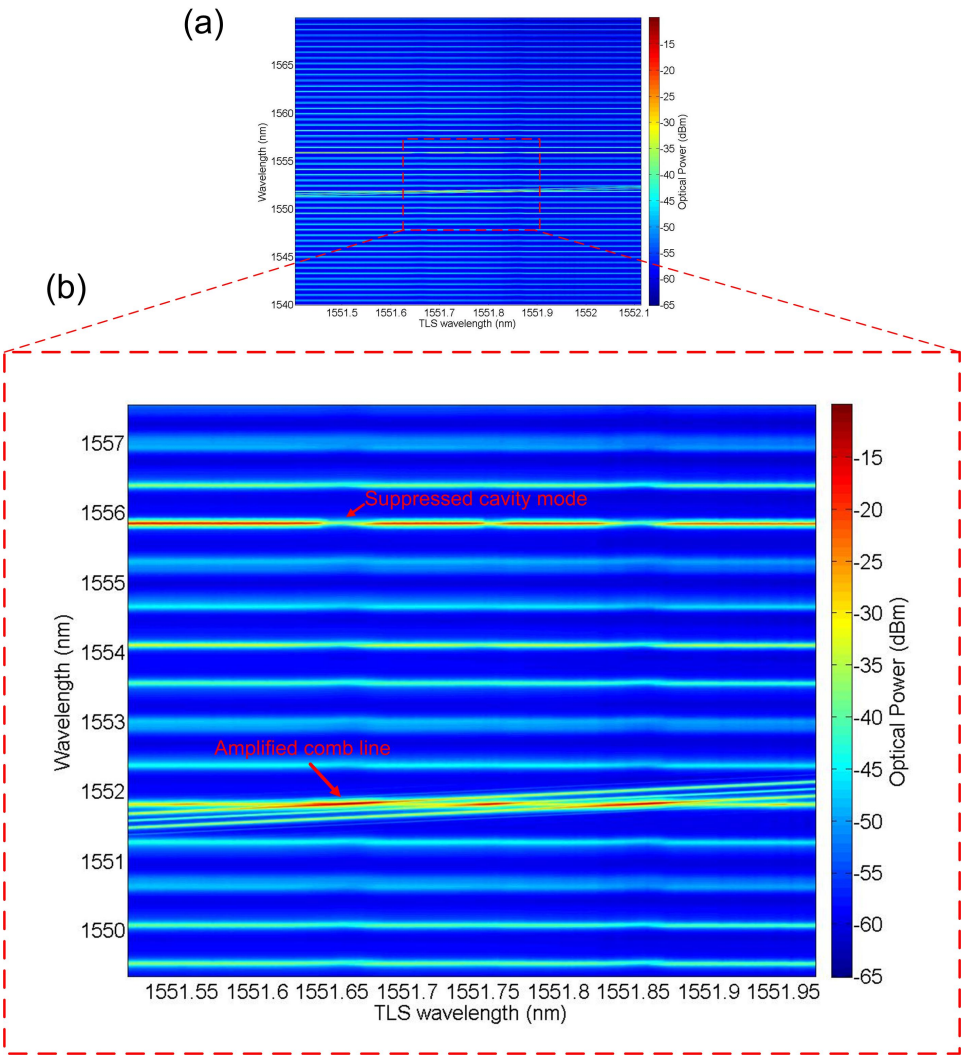


Figure 3.39: (a) wide optical spectrum sweep of the comb lines (b) close up to the locking region showing the amplified comb line and the suppressed cavity modes of the SFP

Fig.3.39 (a) shows a cascaded optical spectrum taken using an OSA. The spectrum shows the results of sweeping 3 comb lines spaced at 10 GHz while the slave laser is biased above threshold. The X axis represent the tunable laser source wavelength that controls the comb wavelength, while the Y axis represents the optical spectrum taken from the OSA at the output of the slave laser. The colour map represent the optical power from the injection locked slave SFP laser.

Fig.3.39 (b) is a close up of the locking region where it shows the 3 comb lines sequentially amplified while suppressing the main cavity mode. Fig.3.40 shows the optical spectrum of the free running slave and the 3 filtered comb lines.

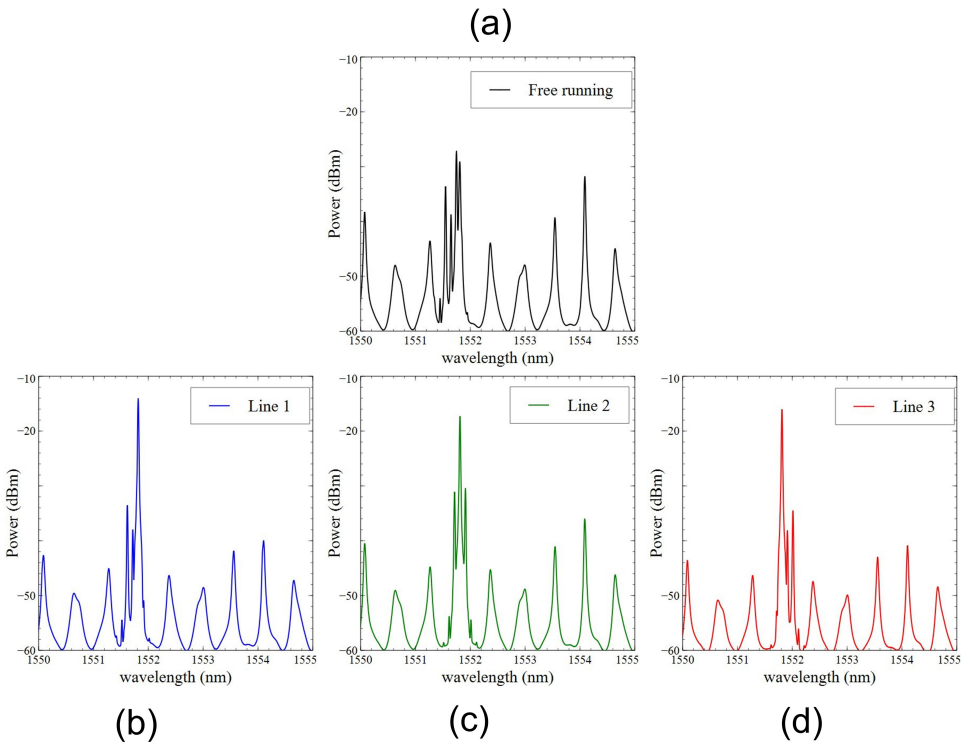


Figure 3.40: (a) free running SFP laser (b) locking of the first comb line (c) locking of the second comb line (d) locking of the third comb line

Fig.3.40 (a) shows the optical spectrum of the free running slave laser just before being injection locked. While Fig.3.40 (b), (c) and (d) shows the 3 comb lines injection locked, and the slave laser mode suppressed. The SMSR of the lines did not exceed 20 dB. It is also important to note that increasing the comb spacing to 20 GHz resulted in a similar SMSR performance.

The SMSR obtained while performing the comb filtering experiment with the slave laser cavity based on pits, V-notches and slots did not exceed 21 dB. Although the pit and V-notch cavities overcame the limitations of the slot, for comb filtering the outcome was the same. Therefore, there is another challenge that limits the SMSR of the filtered comb. One way to assess the performance of the filter to externally injected light is to look at the cavity quality factor (Q-factor). Another issue with the linear cavities that externally injected non-resonant light passes through the cavity and resonant light also passes through with amplification. This effect negatively effects the SMSR of the filtered comb line.

The next section will discuss the overall performance of the linear cavities as coherent comb filters and their limitations based on their Q-factor.

3.1.4.1 Filtering performance analysis and Q-factor

When it comes to using the PIC for Coherent WDM and advanced modulation formats, the obtained SMSR is insufficient. We believe that the main reason for the poor SMSR in those linear cavities is not related to the SMSR of the slave laser itself but rather to its Q-factor that determines the cavity response to externally injected light. The obtained SMSR of the filtered comb lines is mainly due to the selective amplification from the injection locking with poor suppression of the unwanted comb lines. Using a theoretical model to simulate the effect of the Q-factor on the SMSR of an externally injected comb it is possible to track the suppression ratio of the unwanted comb lines. Fig.3.41 shows a simple FP model injected with 3 comb lines.



Figure 3.41: FP cavity with intput and output comb lines showing the SMSR

The Q-factor of the FP cavity, shown in Fig.3.41 is determined by the internal losses and the reflection of mirror 1 and 2. The suppression ratio of the unwanted comb lines (red lines) when they are not in resonance with the FP cavity modes is directly related to the Q-factor of the cavity. Fig.3.42 shows the simulated spectrum and the SMSR of the cavity.

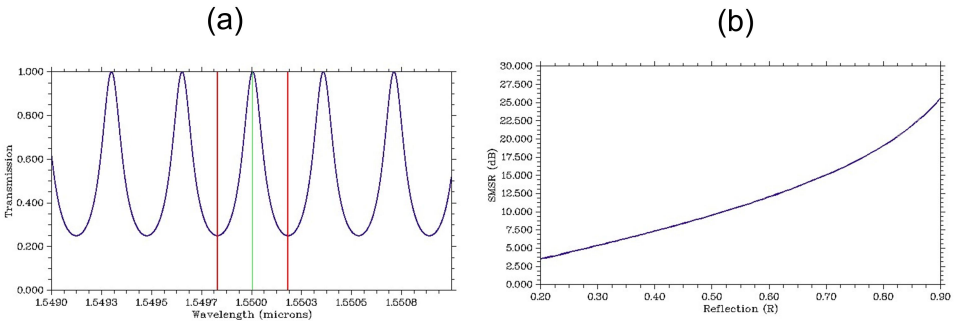
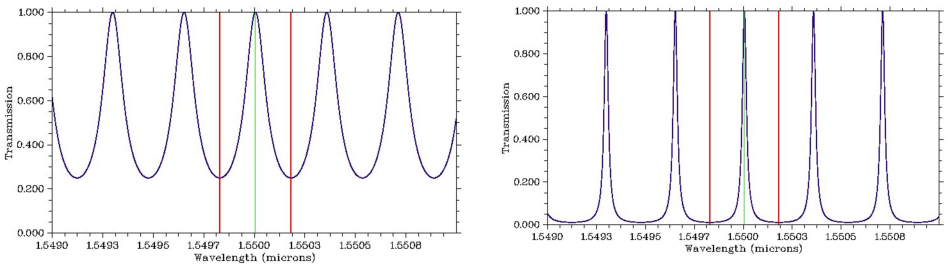


Figure 3.42: (a) simulated spectrum of FP cavity with injected comb lines (b) Comb lines SMSR versus mirrors reflectivity, showing that the higher the reflectivity the higher the SMSR and the Q-factor

Fig.3.42 (a) shows a simulated spectrum of the FP cavity with mirror reflectivities similar to cleaved facets at approximately 33%. The suppression

ratio of the comb lines that fall outside the resonance (red lines) is only 6 dB. By increasing the mirrors reflectivity will result in an increase in the Q-factor consequently improving the SMSR as shown in Fig.3.42 (b).

A comparison between the simulated spectrum of 2 cavities with different mirror reflectivities is shown in Fig.3.43



(a) Mirrors 33 %, SMSR 6 dB (b) Mirrors 80 %, SMSR 19 dB

Figure 3.43: Simulation of 3 comb lines injected into a FP cavities with different mirror reflectivity and their SMSR: (a) mirrors with 33% reflection (b) mirrors with 80% reflection

Fig.3.43 (a) and (b) shows the effects of the Q-factor on the injected comb lines. For example, increasing the mirror reflectivity to 80% increases the SMSR to 19 dB. Based on the simulations above, in order to get the intended cavity Q-factor for efficient filtering, the mirrors reflectivity should be dramatically increased. One way to increase the reflection without affecting the spectrum bandwidth is to use highly reflective (HR) coating on both facets. However, the intended devices for this project are meant to be single facet or facetless to make them suitable for integration, therefore HR coating is not an option. A laser design that is well known for its high Q-factor is the ring laser. They also have the advantage of being completely facetless with no need to use cleaved facets or mirrors to lase. Also in the ring, non-resonant light passes through, but the resonant light can be dropped into a different output waveguide, which eliminates the direct coupling problem with linear cavities. The next chapter will investigate and discuss the fabrication of high Q-factor active ring lasers and their potential use as a coherent comb filter.

Chapter 4

Active rings

4.1 Ring resonators

Active micro-ring resonators have potential interest for photonics integrated circuits as they do not require cleaved facets and provide their own gain [64, 65, 66, 67, 68, 69, 70, 71, 72]. Ring resonators have been employed in WDM and dense WDM systems to de-multiplex closely spaced channels, and have been widely employed as add-drop filters. For closely spaced channel filtering, a sharp response is essential to avoid cross talk between neighbouring channel and maintain a acceptable SMSR. Therefore, the ring cavities have to be designed with a high Q-factor, which determines the filter response.

In order to obtain a high Q-factor ring, the cavity loss has to be minimized. In a racetrack ring configuration as shown in Fig.4.1, two main parameters govern the cavity losses: the waveguide losses and the coupling losses.

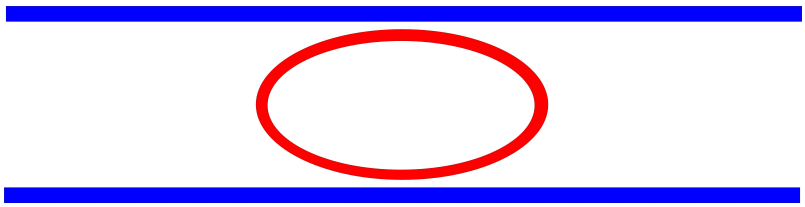


Figure 4.1: Schematic of a racetrack ring resonator

The next 2 subsections will discuss the various approaches taken to optimise the ring cavity losses from the bends and the couplers.

4.1.1 Bends

Low loss bends are critical elements in the PIC. They have to exhibit low loss and the same time be compact enough to efficiently use the space on high density PICs. One way to reduce the loss of the InP based waveguide is to improve the mode mismatch between the straight waveguide and the bent waveguide [73]. The mode mismatch occurs due to the fact that the mode shape in the straight waveguide has a different shape to the mode in the curved waveguide, and this results in optical loss due to radiation loss. Creating a continuous transition from the straight and curved waveguides will allow a smooth transition of the mode. In this work, the bends were designed to have a trapezoidal continuous curvature; more details about the curvature theory and design can be found in [74, 75]. Fig.4.2 show an illustration of a series of fabricated bends.

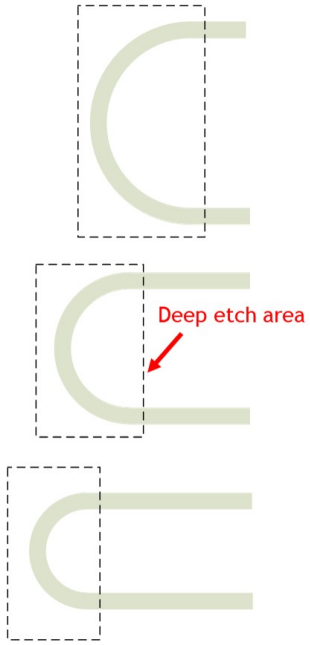


Figure 4.2: waveguide bends with various bend radius and deep etch area

Bent FP lasers with identical total length and different radius of curvature were fabricated. Fig.4.3 show the L-I plot of waveguides with various bend radius.

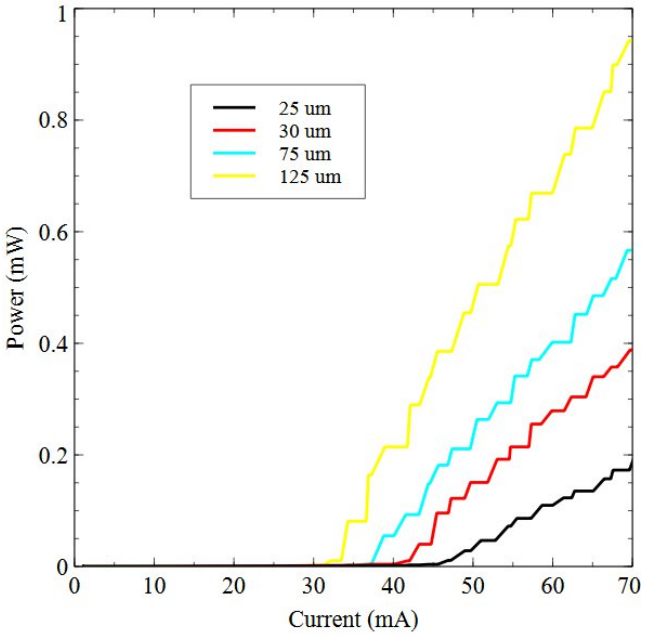


Figure 4.3: L-I plot of bends with radius of: 25μm, 30μm, 75μm and 125μm

The L-I plot shows a linear inverse relation between the bend radius and loss (the irregularities in the L-I plots are due to vibrations in the lensed fiber and delays in data collection from the software). The sharp bend exhibits more loss as expected. A bend with 125μm radius has a lasing threshold of 34 mA, whereas the 25μm bend has a threshold of 45 mA. In the ring laser design a trade-off between the ring size and the losses will take place. In this work, the 75μm bend has been chosen, because it provides low loss while keeping the ring relatively compact

At this stage the waveguide bends were fabricated and characterized. The next major loss factor is from the couplers. The next subsection will investigate various couplers in order to find the optimal one for a ring laser.

4.1.2 Ring couplers

In this work various ring coupler were investigated. The coupling ratio between the ring and waveguide and the loss induced from the coupler are the critical parameters that will determine the suitability of the coupler to create a high Q-factor ring cavity. Other factors such as the coupler footprint will also be considered, as it directly affects the ring size. Moreover, this subsection will elaborate on the advantages and disadvantages of the each of the couplers.

4.1.2.1 MMI couplers

MMI couplers are well established components. They operate based on the principle of mode self imaging across the waveguide [48]. Fig.4.4 (a) shows a schematic of a 2x2 MMI coupler and Fig.4.4 (a) shows a simulation of 2x2 MMI coupler.

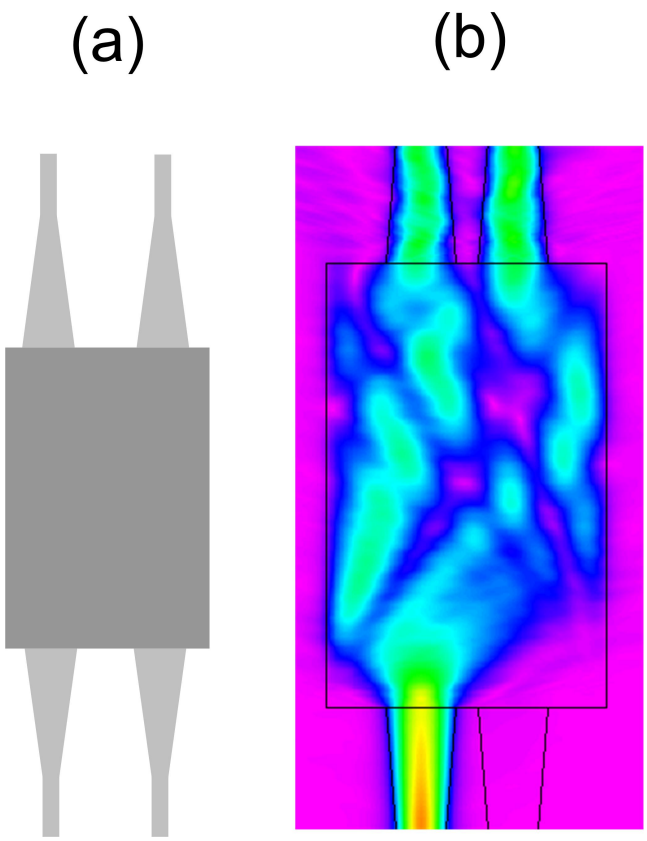


Figure 4.4: (a) schematic of a 2x2 MMI coupler, (b) Simulation of 2x2 MMI coupler

The MMI coupler was simulated using BeamProp from RSoft. The optimized dimension of the MMI is 240 μm in length and 14 μm in width. The input and output coupler were tapered from 3.5 μm to 2.5 μm over 100 μm in order to minimize the coupling losses. The separation between the input/output waveguides is 1.1 μm, corresponding to a centre to centre distance of 4.4 μm between the waveguides. A tunable single mode laser cavity based and two 1x2 MMI couplers is presented in Appendix A. An SEM of a ring laser using an MMI is shown in Fig.4.5

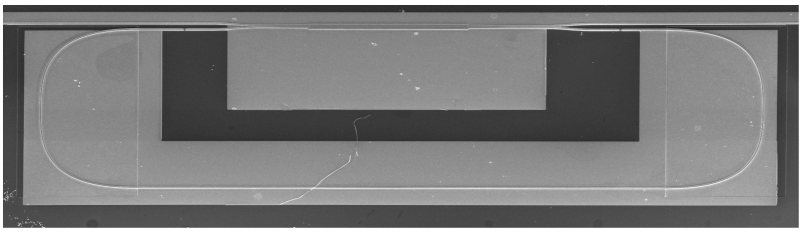


Figure 4.5: SEM of a fabricated ring resonator with MMI coupler

The MMI coupler splits the light equally at each of the outputs, therefore the ring leaks half of its power on each round trip, which reduces the ring Q-factor significantly. Moreover, the insertion loss of the MMI also adds to the overall cavity loss. As a consequence, the MMI was found to be unsuitable for creating a passive high Q-factor cavity. Therefore, a coupler that is more flexible in term of coupling ratio is required in order to keep most of the light inside the ring. Half wave couplers are one option that can be designed in a way to break the symmetric 50:50 coupling ratio, which will be discussed next.

4.1.2.2 Half wave couplers (HWC)

Half wave couplers (HWC) do not operate on the principle of self imaging. They operate as directional couplers with an intermediate section [76]. Fig.4.6 shows the simulation of a 2x2 HWC.

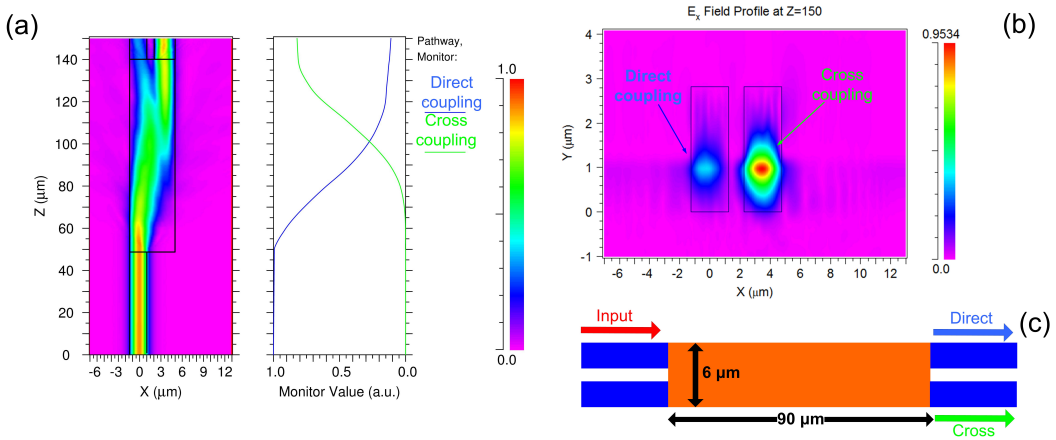


Figure 4.6: (a)Simulation of 2x2 HWC with direct and cross coupling power evolution, (b) mode shape at the output waveguides, (c) schematic with dimensions of a 2x2 HWC

Fig.4.6 (a) shows the the beam propagation simulation of a HWC showing the direct and cross coupling propagation. While Fig.4.6 (b) shows the near field mode shape at the ouptut waveguide for both direct and cross coupling.

Fig.4.6 (c) provides a schematic of the 2x2 HWC with dimensions. A ring laser cavity with a half wave coupler that exhibits a strong single mode operation was fabricated and demonstrated in Appendix B Fig.4.7 shows an illustration a HWC and the coupling variations in fuction of coupler length.

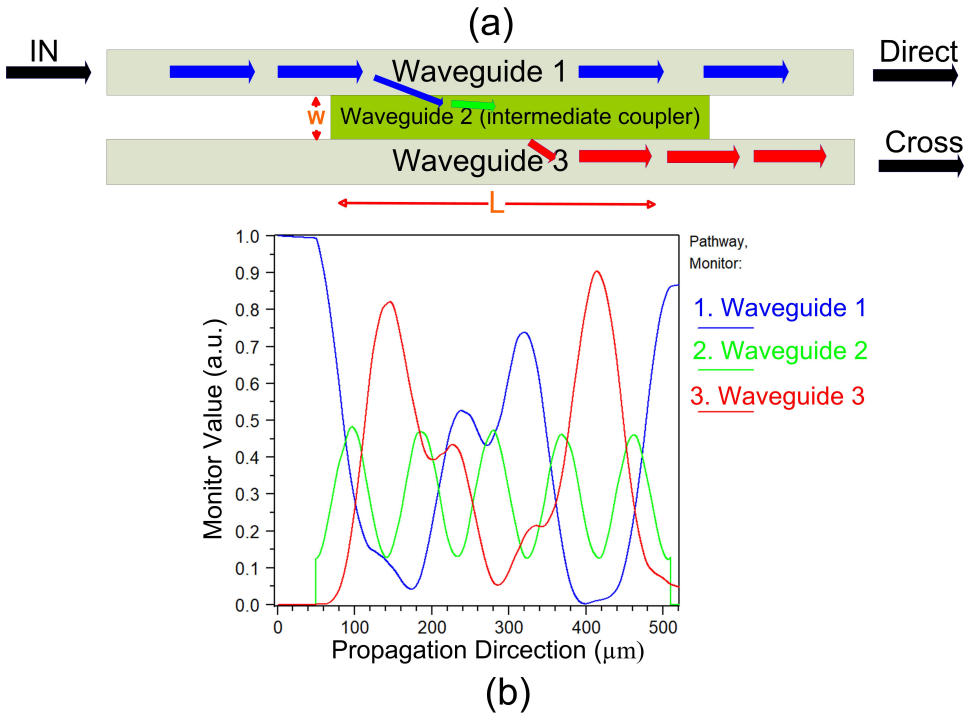


Figure 4.7: (a) illustration of the HWC operation (b) coupling ratio versus HWC length

The illustration in Fig.4.7 (a) shows the HWC length L which represent the total length of the coupler, the width W is the intermediate waveguide width. Both L and W govern the coupling ratio of the coupler. The light coupled from waveguide 1 couples into Waveguide 3 via the intermediate section waveguide 2. In order to better understand the coupling dynamics of the HWC, a power monitor is used in the simulation to show the coupling variation as a function of the coupler length as presented in Fig.4.7 (b).

Fig.4.7 (a) and (b) share the same color codes. In this scenario, light is injected into waveguide 1 and its power represents the direct coupling shown in blue. When the light couples into the intermediate section waveguide 2, the power is represented in green, while the light in waveguide 3 (cross coupling) is shown in red. Based on the simulation, it's possible to determine the desired coupling ratio of the HWC by choosing the appropriate length. In the example presented in Fig.4.7 (b), a HWC with 85% direct coupling and 4% cross

coupling is simulated. However, the power in the intermediate section waveguide 2 always has a minimum power loss of 11%, which means in the case of the of a ring laser with 2 HWC's a 22 % power penalty is introduced. The power loss due to the intermediate section and the insertion losses of the coupler make the HWC unsuitable for passive high Q rings. Fig.4.8 shows an SEM of the fabricated ring with a HWC.



Figure 4.8: SEM of the fabricated ring resonator with HWC

In comparison to the MMI, the HWC allows for a flexible coupling ratio that can be achieved by choosing the right coupling length. Moreover, in term of coupler foot print the HWC can be designed to have much narrow width than the MMI (6μm for the HWC and 14μm for the MMI). However, in order to get the desired coupling ratio the length of the HWC has to be approximately 450μm, which is very similar to the MMI overall length with the input and outputs tapers. In conclusion, although the HWC is more flexible than the MMI the losses introduced by the HWC does not make it suitable for high Q passive ring, and the length of the coupler makes it challenging to create compact rings.

At this stage the research looked into directional couplers. Due to their intrinsic properties, directional couplers are well known for their low loss, and their flexibility in terms of coupling ratio [77].

4.1.2.3 Directional couplers

Directional couplers are well established devices in fiber optic and integrated optics. Directional couplers operate on the principle of evanescent field coupling of two modes propagating in the same direction from 2 separate waveguides [78]. The coupling strength is governed by the length and gap of the 2 waveguide in the coupling region.

A directional coupler was designed to have a 1 μm gap so that it could be fabricated with standard contact lithography. Fig.4.9 show a schematic of a directional coupler that consist of 2 waveguides and a coupling gap.

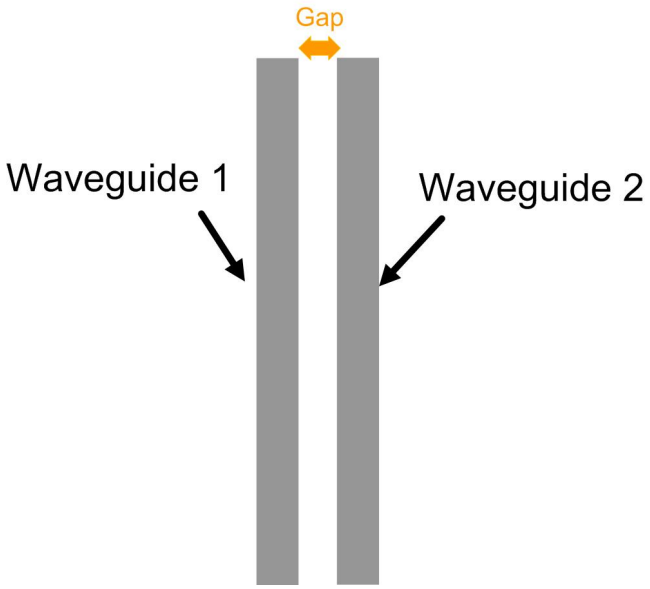


Figure 4.9: directional coupler schematic showing the 2 waveguides and the gap

Fig.4.10 show the simulation result of a directional coupler that consist of two 2.5 μm wide ridges with a 1 μm gap.

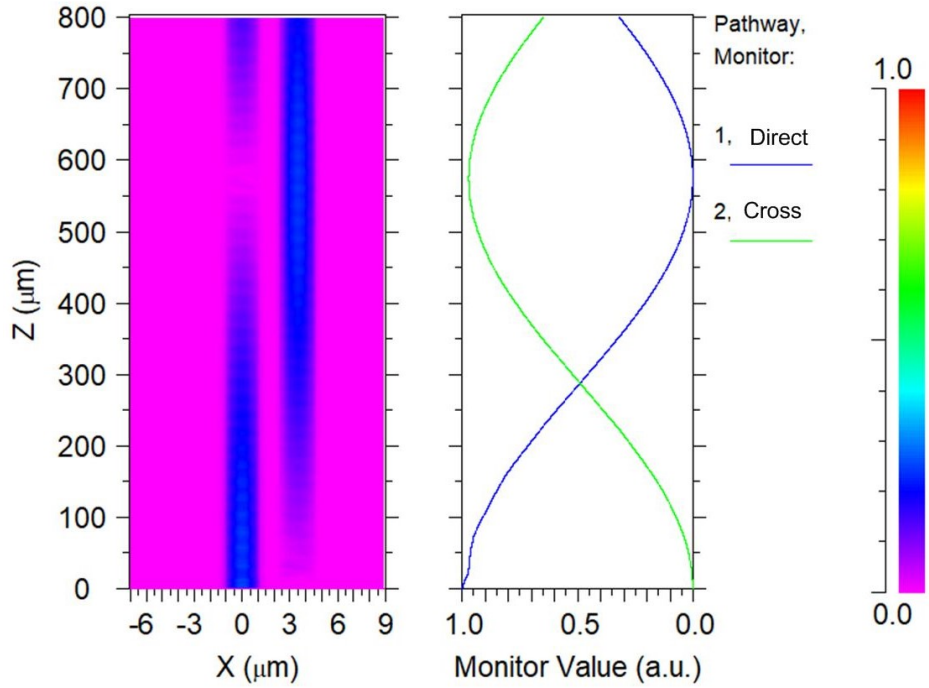


Figure 4.10: Directional coupler simulation and power ratio of the direct and cross coupling

Fig.4.10 (left) shows a directional coupler with a total length of 800 μm. Whereas, the right graph shows the coupler ratio versus length of direct and cross coupling. Based on the simulations a relatively short and low loss coupler can theoretically be designed.

An SEM image of a fabricated ring laser with a directional coupler is shown in Fig.4.11

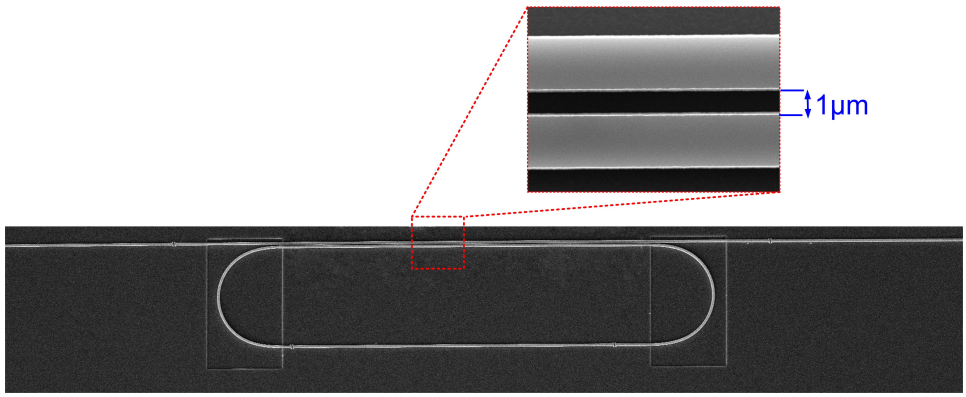


Figure 4.11: SEM of the fabricated ring resonator with directional coupler with 1μm gap

The close up image in Fig.4.11 shows the well defined 1 μm gap between the

waveguides. The rectangular shape around the bends are deep etch areas. These are used to enable low loss high curvature waveguide bends using a deep etched waveguide. The directional coupler allow a flexible control over the coupling ratio between ring and waveguide and exhibits a very low loss. With small coupling, they were be made as short as 100 μm. Therefore, directional couplers are the perfect candidate for high Q rings. As the main application of the ring is comb filtering and amplification, another waveguide for the dropped channel is required. Therefore a set of rings in a racetrack configuration was fabricated as shown in the microscope image Fig.4.12

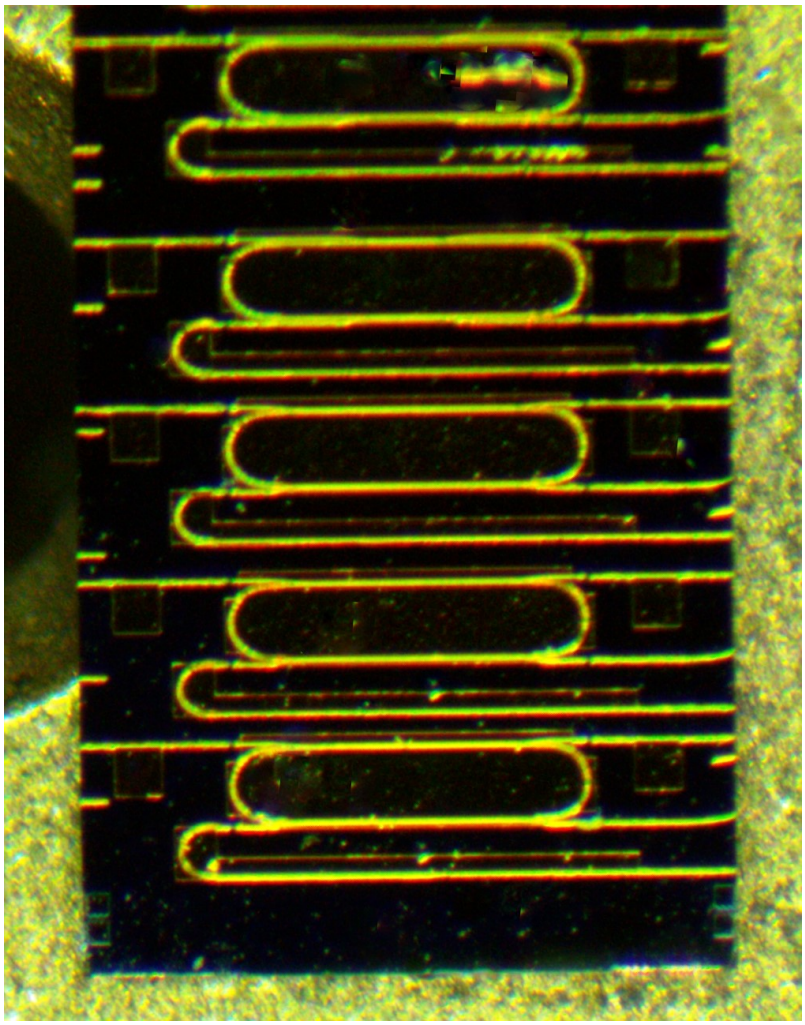


Figure 4.12: Microscope image of the fabricated ring resonators

Fig.4.12 shows a set of racetrack rings with different coupler lengths, and 75μm radius bends. The rings are electrically isolated, so that they can be pumped separately. The illustration in Fig.4.13 shows in details the ring design.

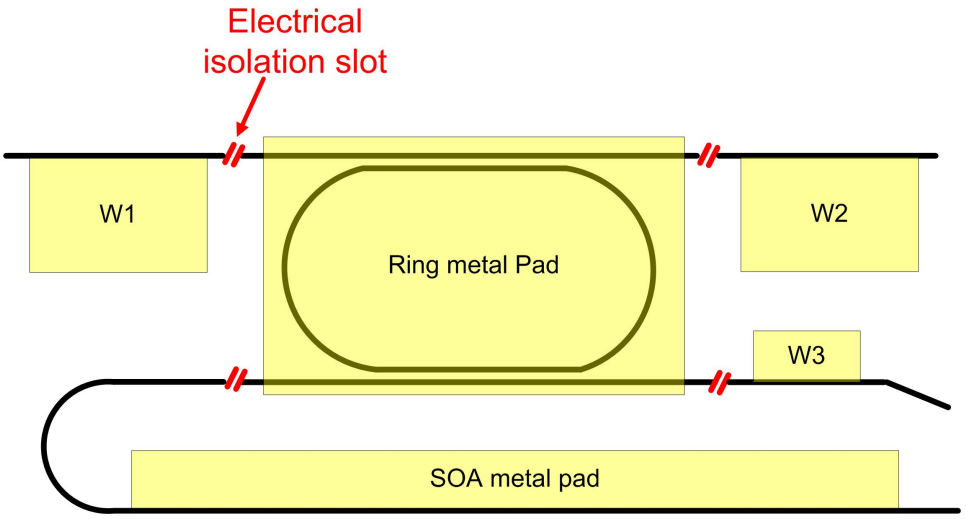


Figure 4.13: schematic of the ring resonator design showing the isolation slots and the metal pads

As in Fig.4.13 the full device is divided by 4 isolation slots into 5 sections. The waveguide sections W1, W2 are used to inject light in and couple light out, whereas W3 is used as an absorber. The ring has its own metal pad and the long waveguide section at the bottom is used as an SOA.

Various techniques are used to measure the Q-factor of a cavity [79, 80]. A straight forward experimental method to measure the ring Q-factor is report in [64]. This method consists of injecting an external finely tunable laser into the cavity and measuring the ON-OFF ratio of the wavelength and the full width at half maximum (FWHM) from the drop port, as shown in the illustration in Fig.4.14 .

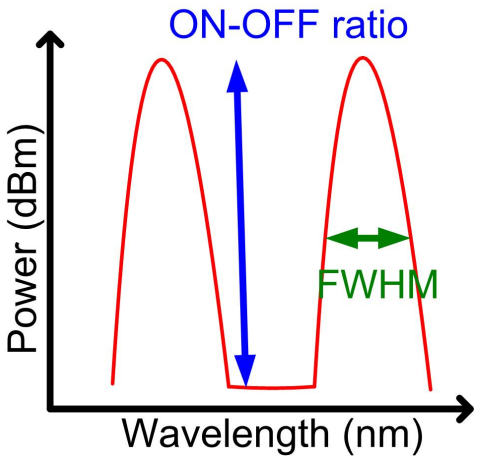


Figure 4.14: illustration of the Q factor measurement using the ON-OFF ratio and FWHM

A cavity with high Q-factor should have a high ON-OFF ratio and a narrow FWHM. In order to choose the suitable ring to perform comb filtering the Q-factor measurement reported in [64] was applied to rings with various coupling ratios. Fig.4.15 shows the experimental setup used to measure the optical response of the ring resonator to externally injected light.

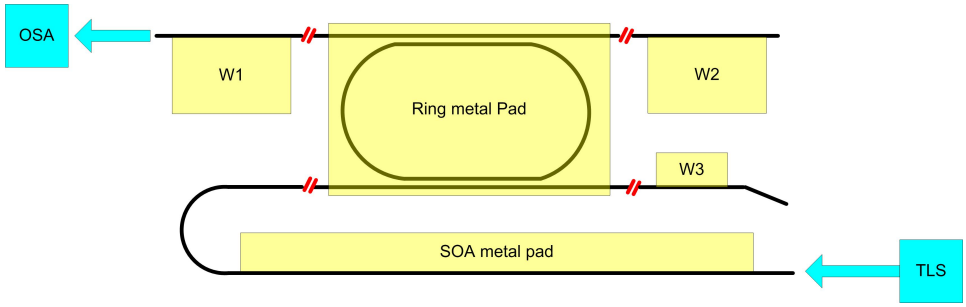


Figure 4.15: Schematic of the experimental setup used to characterize the rings optical response

A tunable laser source (TLS) is injected through a lensed fiber into the PIC and swept over wavelength. The output was coupled via another lensed fibre and measured with an OSA from the drop port of the ring as shown in Fig.4.15. During the test the ring was biased at the lasing threshold. Fig.4.16 shows the resulting Q-factor measurements of the 2 rings with various directional coupler lengths.

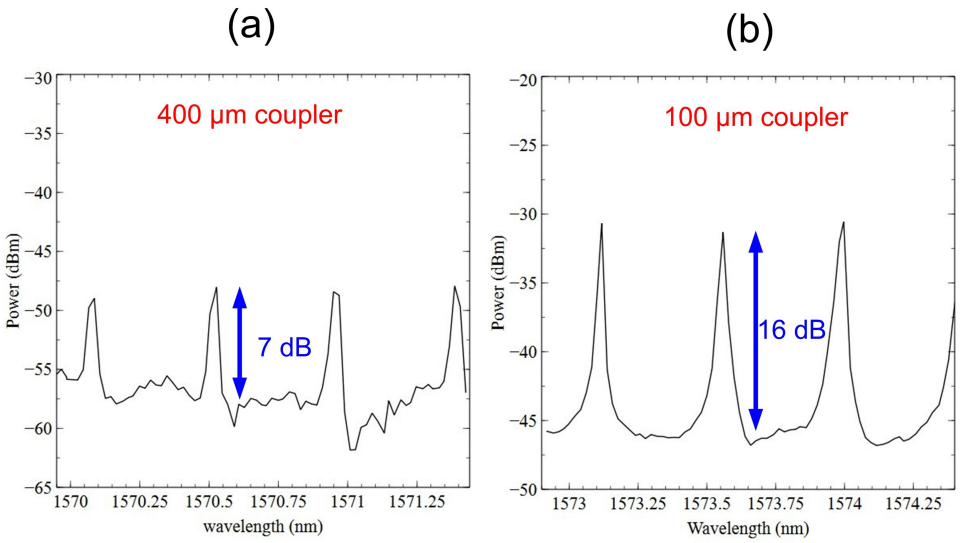


Figure 4.16: (a) optical response of a ring with 400μm coupler, (b) ring with 100 μm coupler

Fig.4.16 (a) and (b) show the optical response of rings with 2 different

directional coupler lengths of 400 μm and 100 μm respectively. The results show the cavity response in term of the suppression to externally injected light. The ring with the shorter coupler showed a superior filter response with a suppression of 16 dB compared to 7 dB suppression for the ring with the long coupler. The ring with the shorter coupler and an estimated cross-coupling of less than 10% exhibited higher SMSR than the long coupler with estimated cross-coupling of 25%. Based on the coupling ratio, the ring with the shorter coupler would exhibit a higher Q-factor due to the fact that more light is trapped inside the ring, which also explains the higher SMSR. At this stage, the ring with the 100 μm coupler was found to be more suitable for comb filtering due to it's high side mode suppression characteristic and will be investigated further in the next section.

Moreover, in order to verify the facet-less operation of the ring laser the optical spectrum and the corresponding FFT of the cavity were measured as shown in Fig.4.17

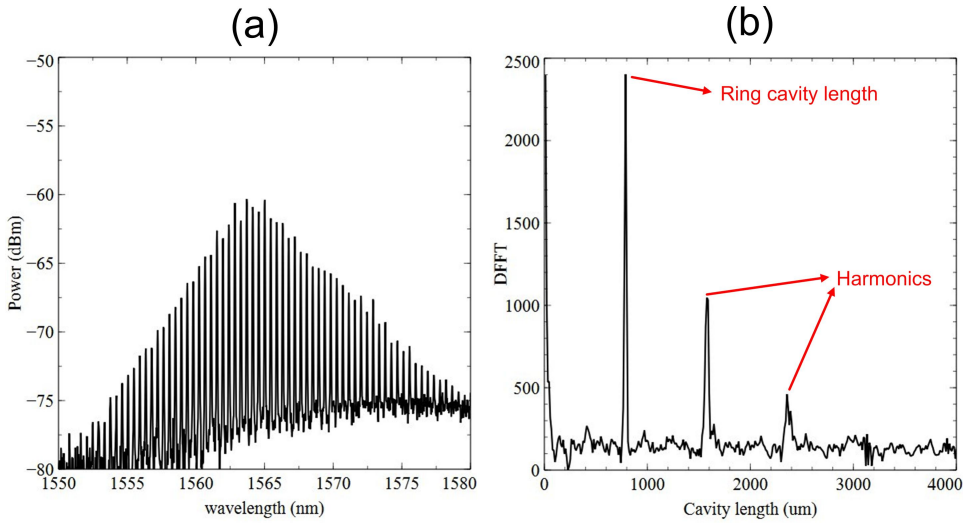


Figure 4.17: (a) optical spectrum of the ring, (b) FFT of the spectrum showing the ring cavity and its harmonics

Fig.4.17 (a) shows the optical spectrum of the ring laser with only the ring metal pad and the SOA pad biased. The resulting FFT spectrum in Fig.4.17 (b) shows the existence of only the ring modes represented by the first peak. The other 2 peaks are the higher order harmonics generated from the FFT algorithm.

The DC in this work is surprisingly not highly sensitive to fabrication and quite repeatable in comparison with passive DC's made with high resolution

lithography. The DC in this case is relatively long (100 um) with a wide gap (1.4 um) in compare to high resolution DC where they can be a only couple of microns long with a gap of only hundreds of nanometre. These small design tolerances make them more sensitive to small fabrication variations.

4.1.3 Coherent comb filtering and selective amplification via injection locking

The experimental setup for the coherent comb filtering experiment is shown in Fig.4.18

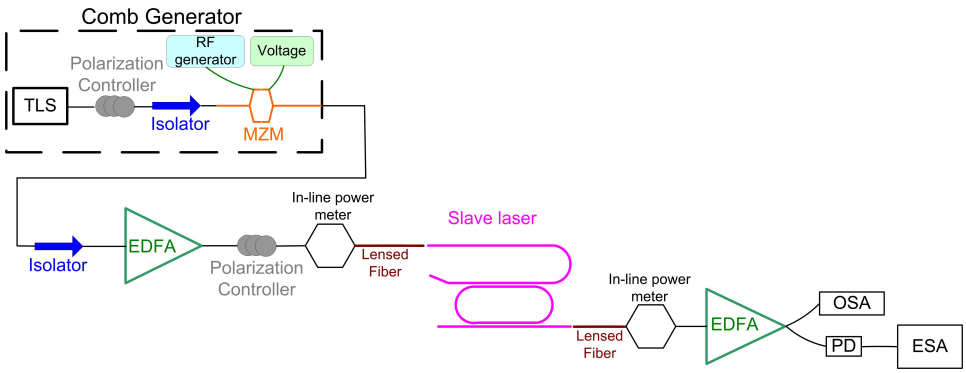


Figure 4.18: Experimental setup for the measurement of the comb filtering and selective amplification

The experimental setup is similar to the setup reported and described in Fig.3.38 of the previous chapter. However, for this experiment the ring laser is the slave laser, which is injection locked. The microscope image in Fig.4.19 shows the device under test with the 2 lensed fibres and probes.

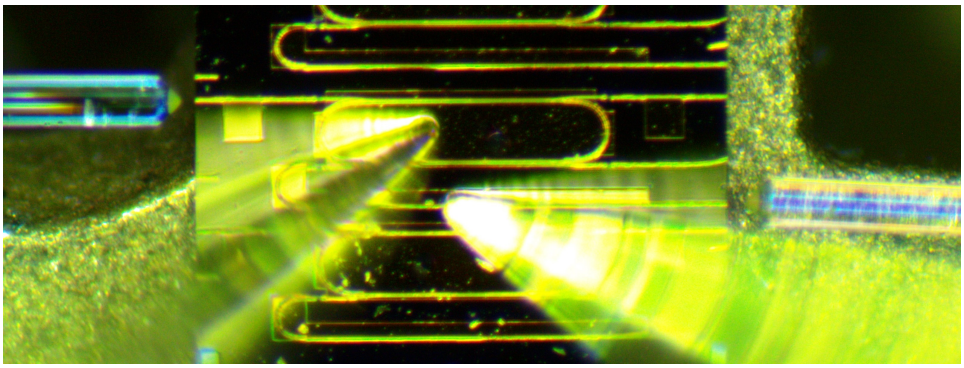


Figure 4.19: Microscope image of the ring resonator under test

The lensed fibre on the right is used to inject the coherent comb into the ring,

while the lensed fibre on the left collects the filtered comb from the drop port of the ring laser. The injected comb optical spectrum is shown in Fig.4.20.

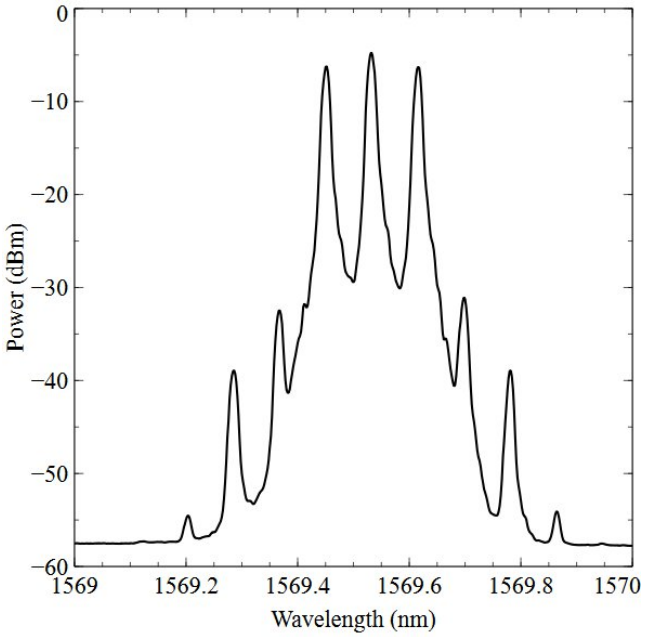


Figure 4.20: The injected 3 comb lines spaced at 10 GHz

The coherent comb lines in Fig.4.20 are spaced at 10 GHz. The successful injection locking of the comb lines was confirmed using both the optical spectrum and the RF spectrum. Fig.4.21 show an example of a free running ring laser just before the locking of one of the comb lines and then the locking of each of the 3 comb lines.

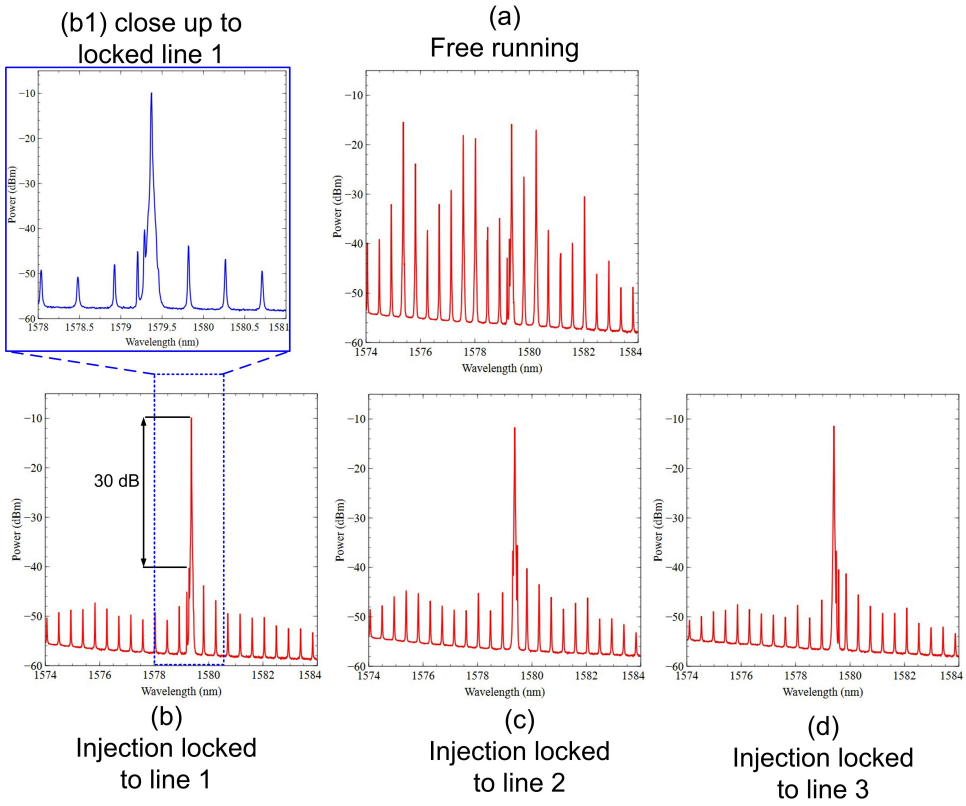


Figure 4.21: 10 GHz comb filtering : (a) free running ring laser, (b) filtering of the first comb line (c) filtering of the second comb line (d) filtering of the third comb line, (b1) a close up image to locked line 1

Fig.4.21 (a) shows the spectrum of the free running laser just before being injection locked to the 3 comb lines spaced at 10 GHz. Fig.4.21 (b), (c) and (d) show the spectrum after locking to each of the comb lines with the SMSR reaching up to 30 dB. When injection locked the ring modes are greatly suppressed while at the same time the desired comb line is selectively amplified. The filtering experiment was also performed on 20 GHz spaced comb lines as shown in Fig.4.22.

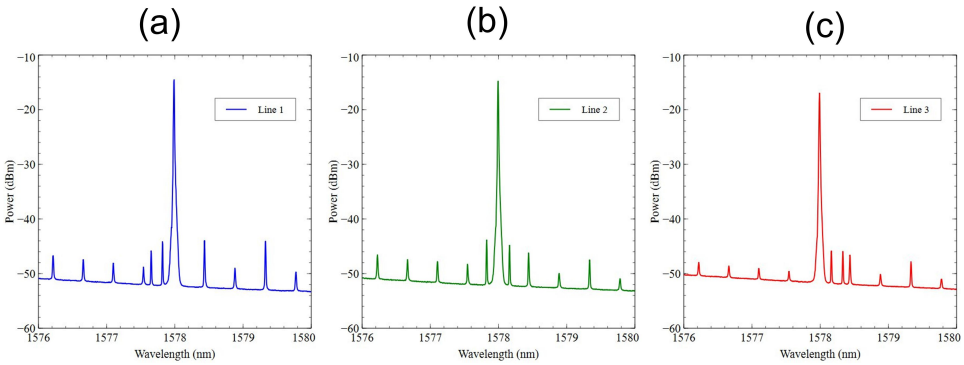


Figure 4.22: 20 GHz comb filtering: (a) line 1 filtered , (b) line 2 filtered (c) line 3 filtered

Fig.4.22 (a) to (c) shows three comb lines spaced at 20 GHz injection locked with a minimum SMSR of 29 dB for all three lines.

In order to further verify the injection locking, an ESA was used to take measurements while performing the injection locking experiment. Fig.4.23 show the ESA sweep trace.

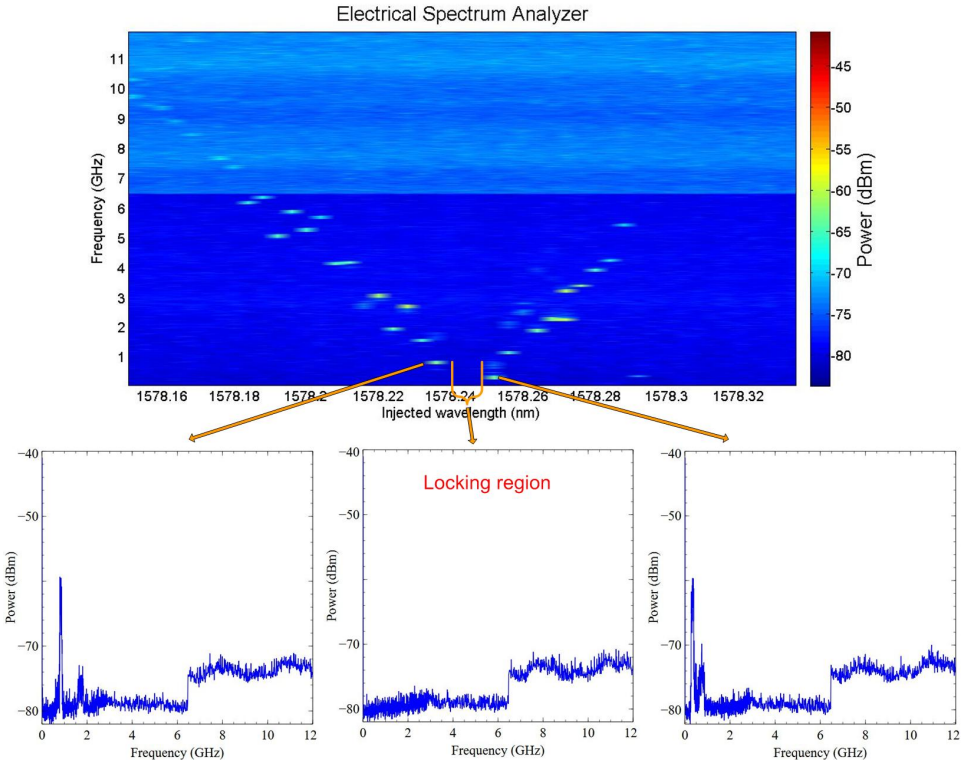


Figure 4.23: ESA sweep spectrum showing the comb line being locked and unlocked from the ring mode

The V shape on the ESA sweep shows initially from left to right the beating

frequency decreasing due to the approach of the comb line to one of the ring modes. The beating keeps decreasing until the modes are locked, which is seen as the quiet region where no beating occurs, as shown in Fig.4.23. When the mode comes out of locking, the beating appears again and its frequency increases as the comb line moves away from the ring mode.

Another important characteristic of the comb filtering and selective amplification is the tunability of the filtering. The tunability is achieved by sweeping and locking the comb lines to various ring modes. Fig.4.24 shows the resulting sweep of the comb.

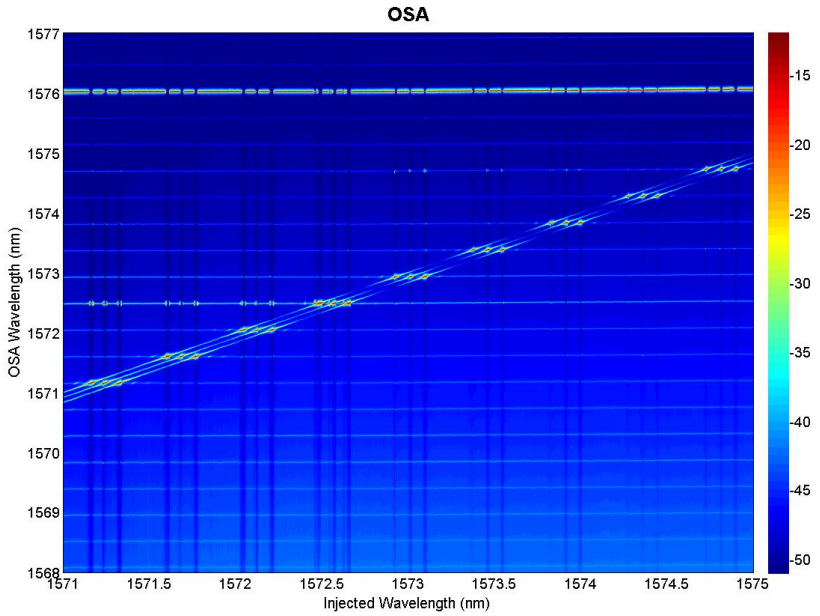


Figure 4.24: Optical spectrum resulting from the sweep of the comb over 4 nm and locking to different ring modes

Sweeping the comb from 1571 nm to 1575 nm resulted in locking of the comb lines to 9 different ring modes as shown in Fig.4.24. In this experiment the master laser (comb) is being swept and the slave laser (ring) is fixed.

In summary the ring laser with directional coupler was successfully used as a facet-less slave laser to filter 10 GHz comb lines and the design demonstrated a tunability across 4 nm locking to 9 ring modes. The relatively short length (100 μm) of the directional coupler allows the future optimization of the design in terms of the foot print of a larger PIC.

Chapter 5

Conclusion and Future Work

Coherent optical combs (COC) have shown great potential in revolutionizing high capacity systems and enable terabits communications [81, 82]. The recent advances in optical comb generation allow the creation of tens and even hundreds of lines with narrow linewidth which can be used to transmit data. Moreover, flatness across wide bandwidth has been reported with the ability to control the central wavelength [83]. By exploiting the coherency of the combs, GHz spaced lines can be used to create terabits super channels [84], such in coherent WDM [85] and Nyquist-WDM signals [86]. This allows a more efficient use of the system bandwidth because it eliminates the need of guard bands. Moreover, COC can be used in elastic networks [87, 88], which exploit the comb lines to create a flexible network. The flexibility is achieved by choosing the number of lines modulated and the modulation format applied to each individual line. Currently, the aforementioned communication systems use discreet components, which make the system bulky, with high cost and power efficiency. Monolithically integrating all the discreet components on a single PIC that act as a COC based transceiver will present a great benefit in term of cost, power efficiency and compactness. Moreover, COC based transceivers monolithically integrated on a PIC offer a very promising solution to use the current fiber optic infrastructure in a more efficient manner in comparison to WDM networks.

One of the main issues in dealing with <50 GHz spaced COC for optical communications is the de-multiplexing of the closely spaced individual comb lines. In standard networks AWGs are used, however at reduced spacing the AWG grows exponentially in size and have fabrication limitations. This

research looked particularity into 20 GHz and less spaced comb de-multiplexing by using injection locked lasers to filter and selectively amplify single comb lines. The first generation of injection locked lasers, the SFP laser suffered from 2 main downsides:

1) Low fabrication yield due to slot high depth sensitivity.

2) Poor SMSR of the filtered comb.

Two deeply etched structures, the pit and the V-notch were successfully developed to overcome the slot sensitivity to depth. In order to demonstrate the efficiency of the pit and V-notch various tunable single mode laser cavities were fabricated using those novel structures. However, although the pit and V-notch solved the fabrication yield issue of the slot, they did not improve the filtering performance, and the SMSR of the filtered comb did not improve in comparison to the original SFP lasers.

A theoretical analysis determined that linear cavities do not make efficient filters due to their low Q-factor and they allow externally injected non resonant light to pass through the cavity. As a result, the research looked into active ring lasers as comb filters, due to their high Q-factor and facetless operation. In order to ensure a high Q-factor :

1) Ring bends were optimized to reduce light round trip loss.

2) various couplers such MMIs, HWCs, and directional couplers were investigated to find the suitable low loss coupler.

Eventually, the directional coupler proved to be the most suitable coupler. By injecting comb lines with spacing of 10 GHz and 20 GHz a SMSR up 30 dB was successfully demonstrated. The injection locking was confirmed optically by looking at the suppression of the unwanted comb lines and the suppression of the ring modes. Furthermore, the locking was also verified electrically by observing quiet regions on the ESA.

To summarize, a regrowth-free, facetless comb de-multiplexer fabricated using standard lithography based on active ring laser was successfully demonstrated.

5.1 Future Work

The future work of this work is divided into 2 stages.

The first stage :

-To reduce the foot print of the ring, to reduce the overall size of the PIC :This could be achieved by further reducing the ring bends radius. In this work, the bend radius used was 75 μm. But, by further improving the fabrication process to achieve a smoother side walls and with further optimization to the bend designs, the bend radius could be reduced.

-To further improve the SMSR of the filtered comb lines : In theory, the SMSR of the comb demultiplexing will improve with higher cavity Q ring laser designs. This could be achieved by reducing the overall losses in the cavity from the waveguides, bends and the coupler. Waveguide losses could be improved with smoother side walls, while the bends will require both smooth side walls and optimized bend designs. Investigating lower coupling ratios from the DC to keep most of the light in the ring, could also potentially improve the Q-factor of the cavity.

-To investigate comb filtering with spacing less than 10 GHz : This work studied comb filtering with spacing from 10GHz and above. Investigating even narrower spacing could allow more efficient use of the bandwidth.

The second stage:

-Integrate a coherent comb generator with single ring laser : An integrated comb generator has been already demonstrated in the Integrated photonic group [15]. The next step is to integrate a ring resonator with the comb generator and investigate on chip filtering. The thermal effects and the interaction between the comb generator and the filter should be investigated and managed.

-Integrate a coherent comb generator with multiple ring lasers.

-Design and fabricate the full Co-WDM PIC that comprise an integrated coherent comb generator, three ring lasers acting as comb filters and finally EAM modulators to modulate the individual comb lines before coupling all combined signals to a lensed fiber via a star coupler.

Appendix A

Mach Zehnder interfermeter laser

A Mach Zehnder interferometer (MZI) is used to create a tunable single mode laser. The MZI laser cavity consists of two 1x2 multimode interference (MMI) couplers used to split/combine two asymmetric pathways resonating between the two cleaved facets. The MZI operation is achieved by exploiting the relative path length differences of the light travelling in the two asymmetric pathways. The constructive and destructive wavelength dependent interference creates a response similar to a filter allowing only the constructively interfered modes to lase. Moreover, only the mode that coincides with the gain peak of the laser material will dominate the transmission, leading to single mode operation.

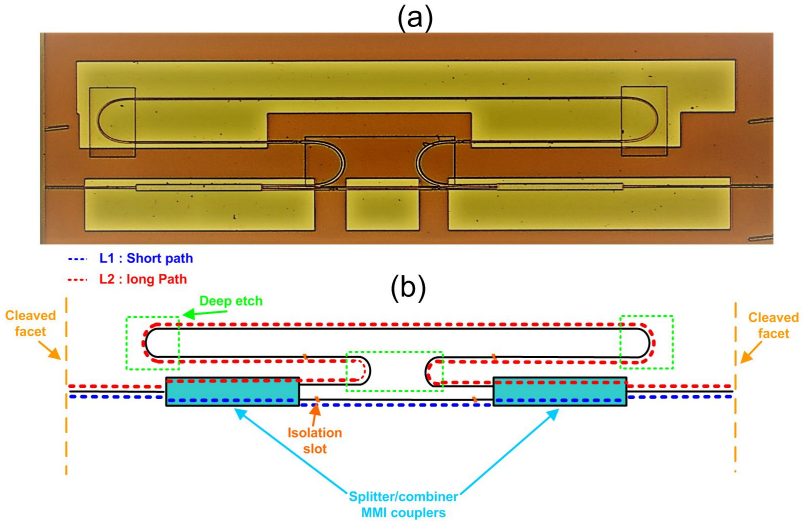


Figure A.1: (a) Microscope image of the MZI laser consisting of 2 MMI's and asymmetric arms (b) design illustration of the MZI laser cavity.

A microscope image of the device is shown in Fig.A.1(a) showing the 4-section laser with the separate metal pads. Fig.A.1(b) shows an illustration of the design, which includes: the deeply etched area inside the green squares, the isolation slots and the MMIs used to split and combine the light. The short and long paths of the MZI (L1 and L2) are illustrated as the blue and red dotted lines respectively with a ΔL of $\approx$ 2 mm. The interference occurs when both cavities with the relative phase difference are combined at the MMIs. Moreover, deeply etched, high curvature bends were used to significantly reduce the footprint of the device which is 400 μm $\times$ 1300 μm. The green squares in Fig.A.1(b) represent the deeply etched regions used to minimize the bending loss by increasing the refractive index contrast, and thus ensuring stronger mode confinement. The laser was divided into 4 sections, each with a separate metal pad. The different sections were separated using an isolation slot with a 7° angle to reduce unwanted reflections. The MMI couplers are critical components in the MZI cavity, as high loss couplers will significantly effect the laser performance in term of output power, SMSR, and linewidth. Therefore, the MMI coupler was simulated using a 3D model of the epitaxial material used to fabricate the laser to ensure optimal performance. The MMI dimensions and input/output waveguides were calculated and optimized using the commercial software BeamProp from Rsoft, which employs the well-established beam propagation method. 80 μm long tapered waveguides were used at the input and the output of the coupler to optimize the power coupling. The waveguides were tapered from 2.5 μm to 3.5 μm. The length and the width of the MMI couplers was 240 μm and 14 μm respectively. Fig.A.2(a) shows the simulation model of the 1$\times$2 MMI and the relevant dimensions are presented in FigA.2(b) along with a microscope image of the coupler FigA.2(c).

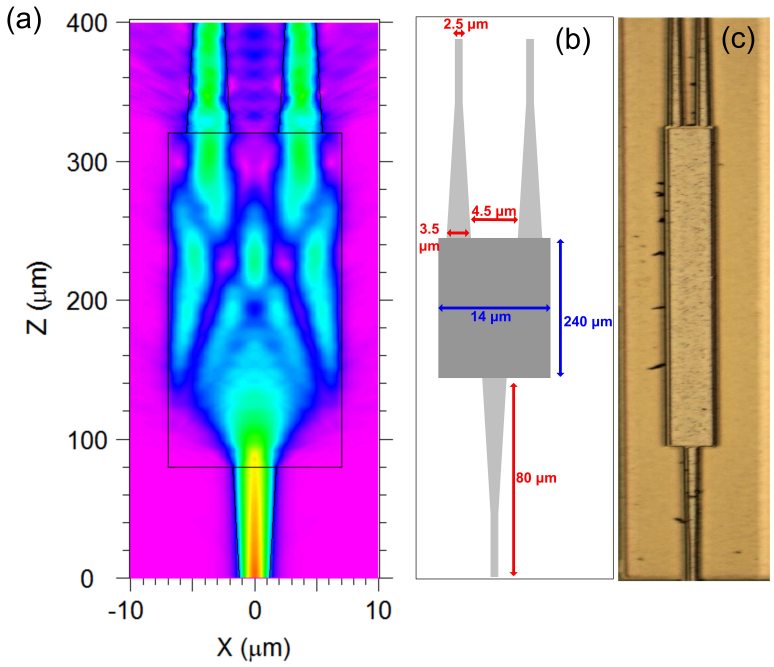


Figure A.2: (a) Simulation of the 1x2 MMI coupler (b) MMI dimensions (c) 1×2 MMI microscope image.

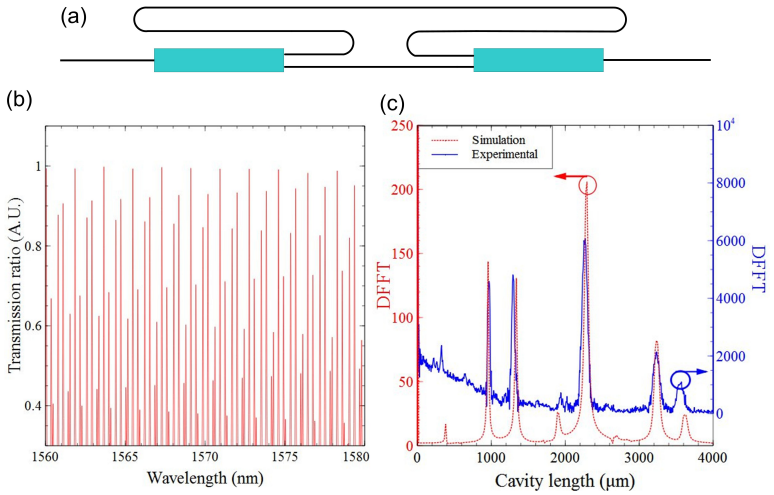


Figure A.3: (a) MZI path ways illustration (b) simulated optical transmission spectrum of the MZI cavity (c) FFT cavity analysis

A theoretical model using the scattering matrix method (SMM) [28] was developed to simulate the cavity design shown in Fig.A.3(a). The model takes into consideration the resonance between the 2 cleaved facets and the phase difference between the MZI arms. A detailed description of the SMM technique used can be found in [89]. The simulated optical spectrum in Fig.A.3(b) shows the transmission as a function of the wavelength across 20 nm generated using

the SMM technique. The MZI cavity results in a free spectral range of ∼1.5 nm, which is sufficient for strong single mode operation when the gain is centred at a resonance. The blue line in Fig.A.3(c) shows the experimental fast Fourier transform (FFT) cavity analysis extracted from the near threshold optical spectrum of the laser. The peaks represent the short and long path length of the laser and the corresponding coupled cavities resulting from the interaction of the 2 cleaved facets and the MZI arms. Furthermore, the red dotted line in Fig.A.3(b) shows the FFT cavity analysis of the theoretical optical resonance model, which shows excellent agreement with the experimental data. This suggests that the developed theoretical model can be used to predict the behaviour of such cavities for further optimization and analysis purposes.

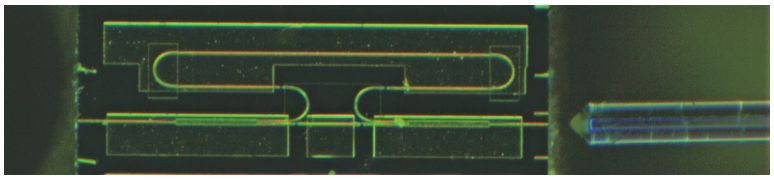


Figure A.4: Microscope image of the DUT.

Four individual probes were used to inject current into the device under test (DUT). The light was coupled into a lensed fiber from one of the two cleaved facets as shown in Fig.A.4. An output power >1mW was measured at multiple wavelengths. The DUT was placed on a temperature controlled brass chuck with a fixed temperature of 20°C. The collected light was then connected to an inline power meter and then to an optical spectrum analyzer (OSA) via the lensed fiber. The single mode operation of the MZI laser can be seen in Fig.A.5.

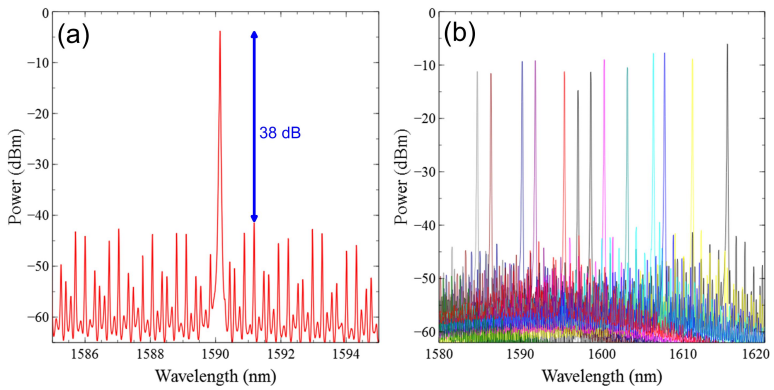


Figure A.5: (a) SMSR of 38 dB (b) tuning over 30 nm.

The laser achieves an SMSR of 38 dB as shown in Fig.A.5(a). Moreover, the laser is tunable from 1584 nm 1615 nm covering 30 nm across the L-band.

The tuning was achieved by increasing the injected current into the MZI, and an SMSR between 33 dB and 38 dB was maintained across the tuning range. The tuning is achieved by increasing the injection current which cause a slight change in the refractive index of the material. A further increase in the current gave rise to thermal effects which caused a red shift to the resonating cavity modes allowing a wide tuning range.

The MZI laser linewidth was measured using a delayed self-heterodyne setup employing 50 km fiber delay line in a recirculating loop configuration.

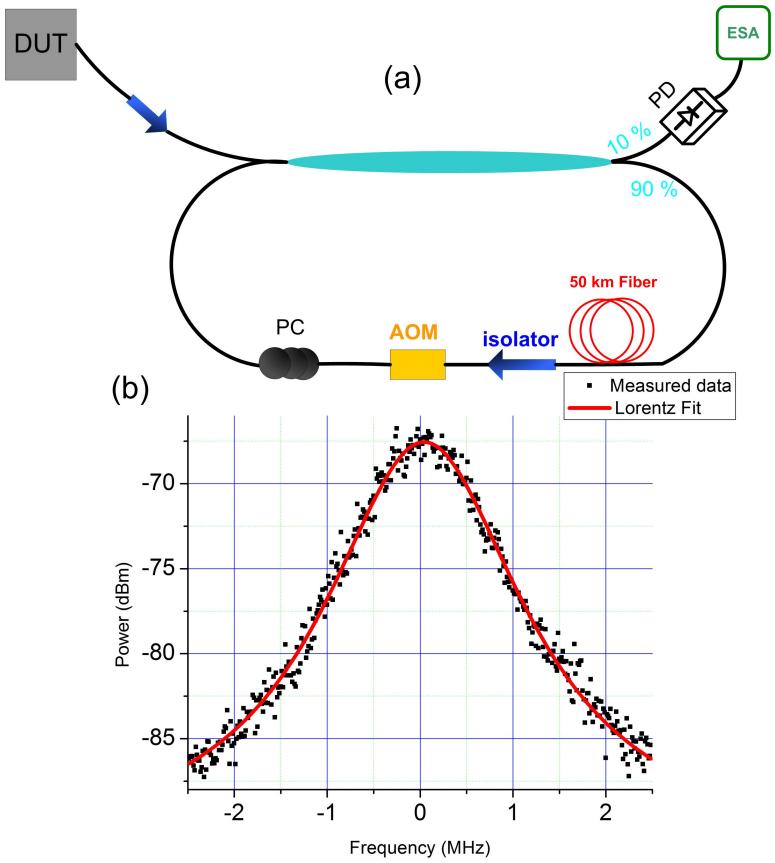


Figure A.6: (a) Re-circulating loop linewidth measurement setup (b) 500 kHz linewidth of the MZI laser.

The experimental setup used to measure the linewidth is shown in Fig.A.6(a). A 90/10 coupler was used to split the light output. The 90% portion of the light propagates through the re-circulating loop mirror. The loop comprises a 50 km single mode fibre delay line, followed by a >30 dB optical isolator. Next an 80 MHz acousto-optic modulator is used to frequency shift the signal before going into a Polarization controller. The shifted signal from the loop is recombined with the original signal and is measured by a 10 MHz-1GHz

photodiode (PD) with a wavelength range of 850 nm to 1650 nm. Finally, a 22 GHz electrical spectrum analyser (ESA) was used to detect the beat signal. Fig.A.6 (b) shows the 1 MHz beat signal which corresponds to a 500 kHz Laser linewidth.

Appendix B

Single mode laser based on coupled cavities of an active ring laser and Fabry Perot

Another approach to creating a tunable single mode laser is by using the effect of coupled cavities between an active ring laser and a Fabry perot. The ring acts as a mode selector and amplifies the resonant mode.

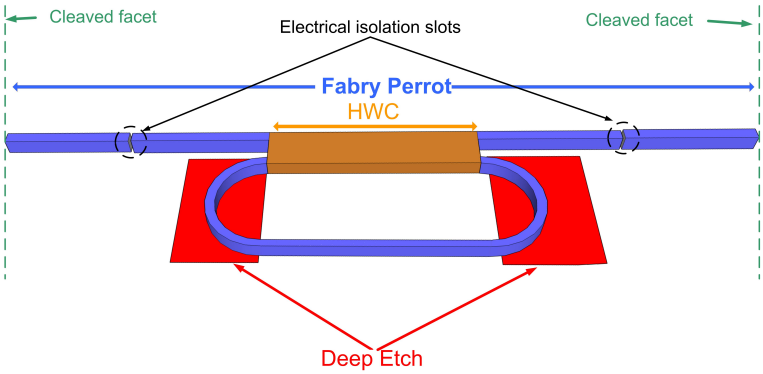


Figure B.1: illustration of the laser cavity design showing the Fabry Pérot and ring cavity.

Fig.B.1 shows an illustration of the laser cavity design. The cavity consist of a 1000 μm long Fabry Pérot (FP) laser and a ring laser coupled via a 90 μm x 6 μm (length x width) HWC. The red area in Fig.B.1 represents the deep etch region used to increase the optical mode confinement to reduce the loss at the bends. The effective ring radius was chosen to be 50 μm to reduce the ring size and maintain a relatively large FSR. Moreover, the ring bends were designed

to be trapezoidal in order to further reduce the bending loss. More detailed information about the bends characteristic and optimization can be found in [74, 75]. The cavity is divided into three sections via two angled isolation slots as shown in Fig.B.1 to improve the wavelength tuning and optimize the SMSR. The HWC was designed and optimized using the commercial software BeamPROP from RSoft. The splitting ratio of the coupler is 10:80, in which 80% of the light is cross coupled and 10% is straight coupled. The remaining power is lost, which is considered acceptable in the PIC, since the HWC is significantly smaller than either a MMI or a directional coupler.

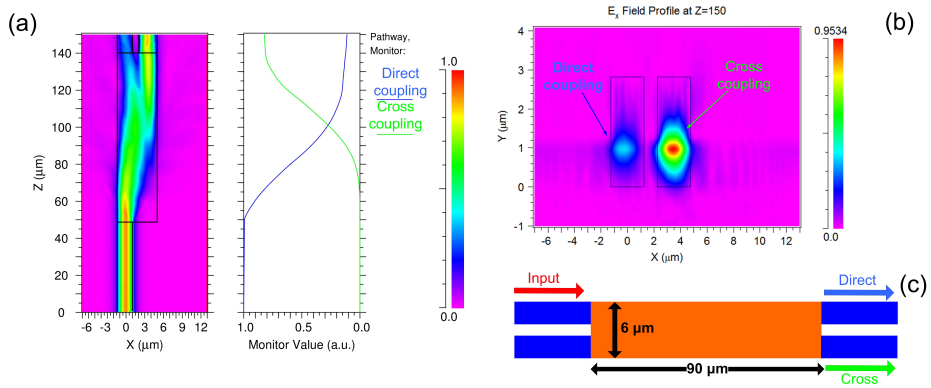


Figure B.2: (a) simulation of the HWC showing the direct and cross power coupling ratios (b) the modes intensity at the 2 output waveguides, (c) illustration showing HWC dimensions and outputs

The simulation of the HWC is shown Fig.B.2 (a) where a power monitor shows the evolution of coupling along the length of the coupler. The green line and the blue line represent the cross and the direct coupling respectively. The observed residual loss of around 10% can be optimized by increasing the length and width of the coupler. However, this size increase will consequently reduce the longitudinal mode spacing which can limit the SMSR of the laser. A series of cavities using various couplers lengths and widths were fabricated and tested, with the 90 μm x 6 μm HWC showing the highest SMSR. The reported HWC was also optimized to be compatible with UV contact lithography with a width of 6 μm and input/output waveguide width of 2.5 μm spaced at 1 μm. Fig.B.2 (b) shows the mode field shape, diameter and intensity just at the HWC outputs for cross and direct coupling. The cross-coupling power is visibly stronger as expected from 80:10 coupling ratio. Fig.B.2(c) show the illustration of the HWC with its dimension along with the direct and cross outputs. A microscope and SEM image of the cavity and the

coupler are shown in Fig.B.3.

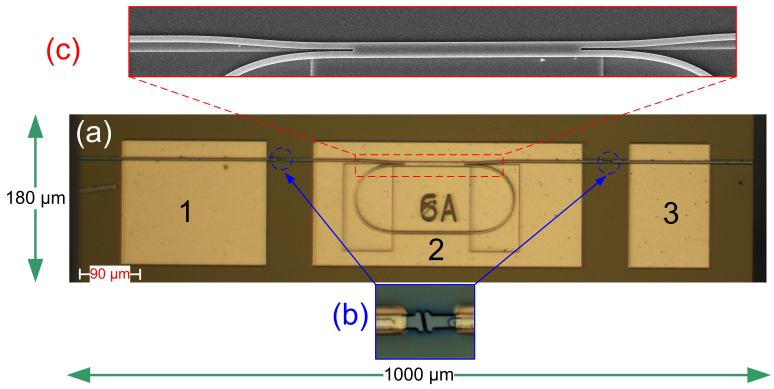


Figure B.3: (a) Microscope image of the laser cavity, (b) a close up image of the isolation slot,(c) SEM image of the HWC

Fig.B.3(a) show a microscope image of the 3-section laser cavity. Three separate metal pads were used to bias the laser. The sections are isolated using a 7°, 1 μm wide angled shallow slot (1.75 μm deep) etched to just above the active region to minimize reflections Fig.B.3(b).

The laser was mounted on a temperature controlled brass chuck with a fixed temperature of 15°C . A lensed fiber at one of the cleaved facets was used to collect the light. At the lensed fiber output, a power meter and an optical spectrum analyzer were used to measure the laser power and spectrum respectively.

To test the ring coupled HWC operation and to ensure it is lasing solely without the need of cleaved facets, the ring pad 2 (Fig.B.3 (a)) was biased at 100 mA, while pad 1 was set at a reverse bias of -3V to act as light absorber to eliminate any interaction with the left cleaved facet. Pad 3 was then left unbiased to allow light to couple out into a lensed fiber. The optical spectrum taken using the Ando AQ6317 optical spectrum analyzer (resolution of 0.01 nm) is shown in Fig.B.4.

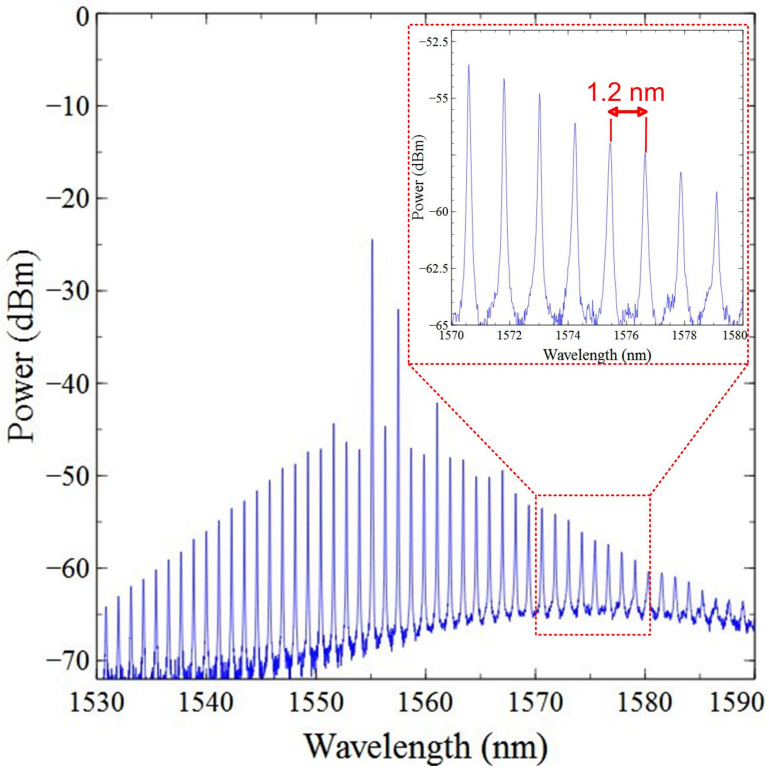


Figure B.4: Spectrum with only ring pad is biased (at 70 mA), inset showing ring FSR

Fig.B.4 shows the spectrum collected from the right facet while only the ring pad was biased. The inset figure shows that the FSR is 1.2 nm which correspond to ring cavity length. The lasing threshold of the ring was measured at approximately 70 mA, and this high lasing threshold is due to the low Q of the ring caused by the 80% cross coupling of the HWC. It is worth noting, that the deep to shallow transitions were measured in separate Fabry Perot structures, where no modulation in the optical spectra was seen. Thus, any reflections from these transitions are negligible in their effect on the optical spectra.

Fig.B.5(a) shows the laser spectrum with an SMSR of 41 dB with all 3 pads biased. Moreover, Fig.B.5(b) shows the laser light-intensity (L-I) plot with a lasing threshold of around 24 mA. The L-I plot measurement was taken by biasing pads 1 and 3 as shown in Fig.B.3 (a) at 15 mA each and sweeping the current applied to the ring (pad 2) from 0 mA to 60 mA

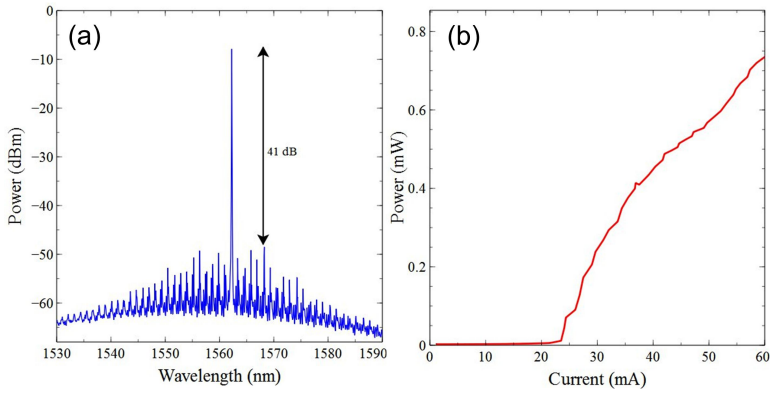


Figure B.5: (a) Single mode with a SMSR of 41 dB (Ring Biased at 100 mA, Pad 1 and Pad 2 at 10 mA)(b) L-I plot of the laser cavity

Taking into consideration that the laser cavity is active: the low (10%) through coupling at the ring is easily compensated by the gain in the ring, such that the ring is able to lase on its own (as seen in Fig.B.4). At, or near this lasing condition, the ring acts as a very strong high-Q mode filter acting on the Fabry-Perot portion of the laser, while providing significant gain at the resonant condition of the Fabry Pérot and ring. This strong filtering is made possible due to frequency selective gain in the ring. For passive filters, a high through coupling is required to enable a good filter, and this design is therefore more often used. Such as design, with a higher though coupling would still result in a good mode filter, but would provide significantly less gain for the laser. Thus, our choice of coupler (low through coupling and high cross coupling) utilizes both the filtering and gain properties of the ring section resulting in a better compound laser with better SMSR than the opposite coupler (high through coupling and low cross coupling). The concept of controlling the Q cavity of an active ring by increasing the gain has been studied and demonstrated in active-passive waveguides such as in [64], where an SOA was used to compensate the loss of the ring, drastically increase the Q-factor and enhance the filter capabilities of the ring.

Fig.B.6 shows the 400 kHz measured linewidth (blue dots) and its Lorentzian fit (red line) of the single mode, shown in Fig.B.5(a).

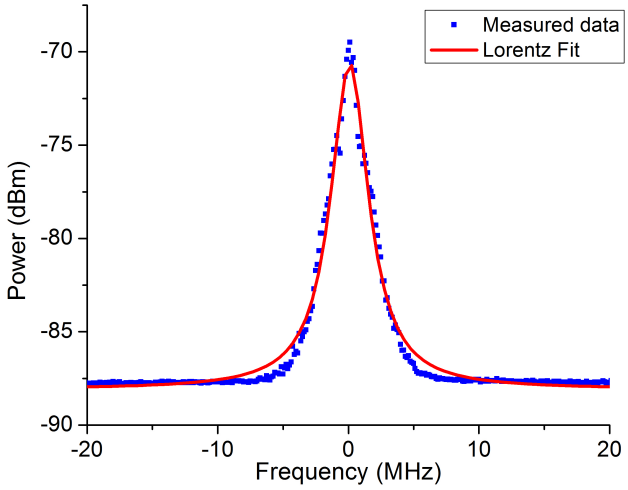


Figure B.6: Measured 400 kHz laser linewidth (blue dots) of the spectrum in Fig.5 with same operation conditions, and the corresponding Lorentzian fit (red line)

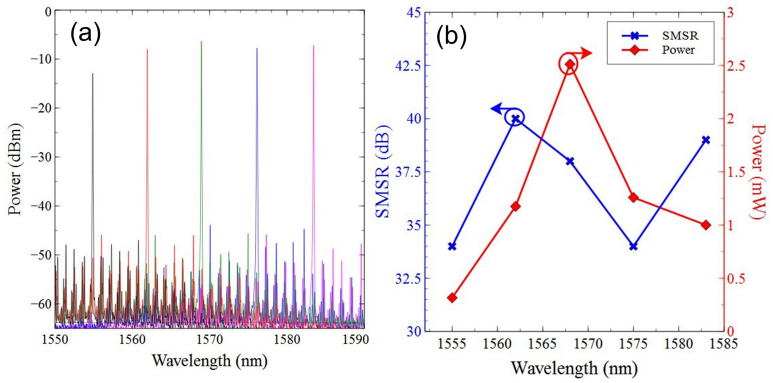


Figure B.7: (a) Laser tunability across 5 channels (b) Power and SMSR performance for each of the channels

The cavity can be tuned over 24 nm by changing the injection current through the ring, achieving 5 tunable channels with 6 nm spacing. Fig.B.7(a) shows the overlap spectrum of the various wavelengths extending from 1555 nm to 1584 nm. The performance of the individual channels in term of SMSR and power can be seen in Fig.B.7(b). The laser achieves a good SMSR across all channels that varies between 34 dB and 41 dB. Moreover, power up to 2.5 mW was coupled via the lensed fiber, with most channels having $>$ 1 mW output. It is important to mention, that to simplify the overall laser fabrication and processing, no high reflection (HR) coating was used on any of the facets. Fig.B.8 shows the simulated, near threshold spectrum of the laser with

relevant spacing. The 6nm FSR of the compound laser is caused by the resonance between the ring and the Fabry Perot sections of the laser.

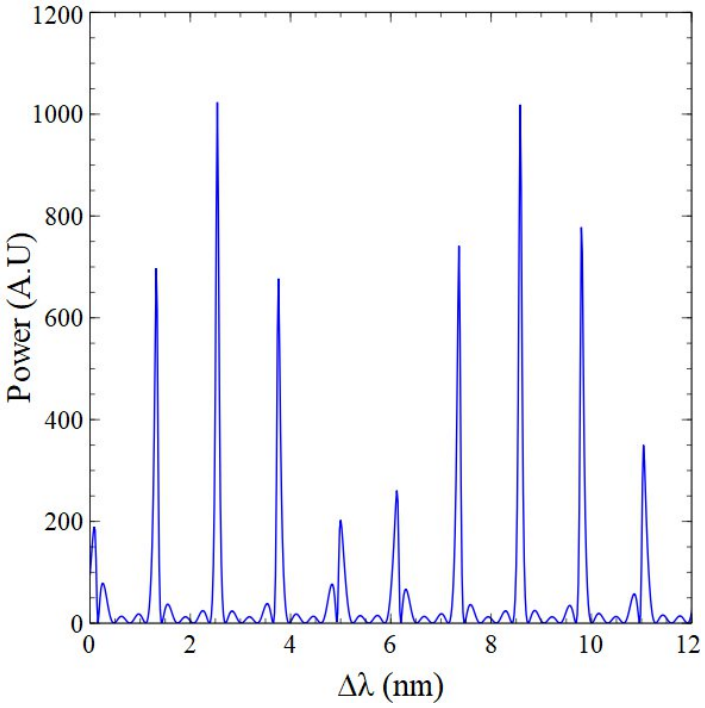


Figure B.8: Simulation of the compound laser resonance of the ring and Fabry Perot cavities, with 6 nm spacing between main peaks

The compound semiconductor laser presented has the advantage of combining a relatively small foot print and a sub-MHz linewidth. In comparison with similar designs, the laser covers a wide tuning range across 24 nm, whereas the cavities in [41, 90] for example offer a finer tuning of only a few nanometers. Other designs, such as the slotted Fabry Perot cavities have a narrow linewidth that can reach tens of kHz and wide tuning range, however these laser cavities can extend over 2 mm in length.

B. Single mode laser based on coupled cavities of an active ring laser and Fabry Perot

References

[1] B. Mukherjee, *Optical WDM networks*. Springer Science & Business Media, 2006.

[2] A. Banerjee, Y. Park, F. Clarke, H. Song, S. Yang, G. Kramer, K. Kim, and B. Mukherjee, "Wavelength-division-multiplexed passive optical network (wdm-pon) technologies for broadband access: a review," *Journal of optical networking*, vol. 4, no. 11, pp. 737–758, 2005.

[3] P. J. Winzer and R.-J. Essiambre, "Advanced modulation formats for high-capacity optical transport networks," *Journal of Lightwave Technology*, vol. 24, no. 12, pp. 4711–4728, 2006.

[4] P. J. Winzer, "High-spectral-efficiency optical modulation formats," *Journal of Lightwave Technology*, vol. 30, no. 24, pp. 3824–3835, 2012.

[5] A. D. Ellis, F. C. G. Gunning, and T. Healy, "Coherent wdm: The achievement of high information spectral density through phase control within thetransmitter," in *Optical Fiber Communication Conference*, p. OThR4, Optical Society of America, 2006.

[6] T. Udem, R. Holzwarth, and T. W. Hänsch, "Optical frequency metrology," *Nature*, vol. 416, no. 6877, p. 233, 2002.

[7] M. J. Thorpe, D. Balslev-Clausen, M. S. Kirchner, and J. Ye, "Cavity-enhanced optical frequency comb spectroscopy: application to human breath analysis," *Optics Express*, vol. 16, no. 4, pp. 2387–2397, 2008.

[8] R. Holzwarth, T. Udem, T. W. Hänsch, J. Knight, W. Wadsworth, and P. S. J. Russell, "Optical frequency synthesizer for precision spectroscopy," *Physical review letters*, vol. 85, no. 11, p. 2264, 2000.

[9] T. Bajraszewski, M. Wojtkowski, M. Szkulmowski, A. Szkulmowska, R. Huber, and A. Kowalczyk, "Improved spectral optical coherence tomography using optical frequency comb," *Optics express*, vol. 16, no. 6, pp. 4163–4176, 2008.

[10] X. Yi, N. K. Fontaine, R. P. Scott, and S. B. Yoo, "Tb/s coherent optical ofdm systems enabled by optical frequency combs," *Journal of Lightwave Technology*, vol. 28, no. 14, pp. 2054–2061, 2010.

[11] H. Sanjoh, E. Yamada, and Y. Yoshikuni, "Optical orthogonal frequency division multiplexing using frequency/time domain filtering for high spectral efficiency up to 1 bit/s/hz," in *Optical Fiber Communication Conference*, p. ThD1, Optical Society of America, 2002.

[12] W. Shieh, H. Bao, and Y. Tang, "Coherent optical ofdm: theory and design," *Optics express*, vol. 16, no. 2, pp. 841–859, 2008.

[13] P. Del'Haye, A. Schliesser, O. Arcizet, T. Wilken, R. Holzwarth, and T. J. Kippenberg, "Optical frequency comb generation from a monolithic microresonator," *Nature*, vol. 450, no. 7173, p. 1214, 2007.

[14] A. Martinez, C. Calò, R. Rosales, R. Watts, K. Merghem, A. Accard, F. Lelarge, L. Barry, and A. Ramdane, "Quantum dot mode locked lasers for coherent frequency comb generation," in *Quantum Sensing and Nanophotonic Devices XI*, vol. 8993, p. 89930A, International Society for Optics and Photonics, 2014.

[15] J. Alexander, P. Morrissey, H. Yang, M. Yang, P. Marraccini, B. Corbett, and F. Peters, "Monolithically integrated low linewidth comb source using gain switched slotted fabry-perot lasers," *Optics express*, vol. 24, no. 8, pp. 7960–7965, 2016.

[16] A. D. Ellis and F. G. Gunning, "Spectral density enhancement using coherent wdm," *IEEE Photonics Technology Letters*, vol. 17, no. 2, pp. 504–506, 2005.

[17] F. G. Gunning, T. Healy, and A. Ellis, "298 gbit/s coherent wdm transmission over 80 km of smf at 1 bit/s/hz spectral efficiency," in *Optical Communication, 2005. ECOC 2005. 31st European Conference on*, vol. 3, pp. 445–446, IET, 2005.

[18] F. G. Gunning, T. Healy, R. Manning, and A. Ellis, "Multi-banded coherent wdm transmission," in *Optical Communication, 2005. ECOC 2005. 31st European Conference on*, vol. 6, pp. 23–24, IET, 2005.

[19] J. E. Whiteaway, G. H. Thompson, and T. Bricheno, "Optical comb filter," Oct. 9 2001. US Patent 6,301,409.

[20] S. Huang, Y. Hua, and L. Li, "Optical comb filter," Feb. 9 2017. US Patent App. 15/303,524.

[21] C.-L. Lee, R.-K. Lee, and Y.-M. Kao, "Design of multichannel dwdm fiber bragg grating filters by lagrange multiplier constrained optimization," *Optics express*, vol. 14, no. 23, pp. 11002–11011, 2006.

[22] H. Singh and M. Zippin, "Apodized fiber bragg gratings for dwdm applications using uniform phase mask," in *Optical Communication, 1998. 24th European Conference on*, vol. 1, pp. 189–190, IEEE, 1998.

[23] M. Kuznetsov, N. M. Froberg, S. R. Henion, and K. A. Rauschenbach, "Power penalty for optical signals due to dispersion slope in wdm filter cascades," *IEEE Photonics Technology Letters*, vol. 11, no. 11, pp. 1411–1413, 1999.

[24] K. Okamoto, K. Syuto, H. Takahashi, and Y. Ohmori, "Fabrication of 128-channel arrayed-waveguide grating multiplexer with 25 ghz channel spacing," *Electronics Letters*, vol. 32, no. 16, pp. 1474–1476, 1996.

[25] A. Srivastava, Y. Sun, J. Sulhoff, C. Wolf, M. Zirngibl, R. Monnard, A. Chraplyvy, A. Abramov, R. Espindola, T. A. Strasser, *et al.*, "1tb/s transmission of 100 wdm 10 gb/s channels over 400 km of true wavetmfiber," in *Optical Fiber Communication Conference*, p. PD10, Optical Society of America, 1998.

[26] R. Nagarajan, M. Kato, J. Pleumeekers, P. Evans, S. Corzine, S. Hurtt, A. Dentai, S. Murthy, M. Missey, R. Muthiah, *et al.*, "Inp photonic integrated circuits," *IEEE Journal of Selected Topics in Quantum Electronics*, vol. 16, no. 5, pp. 1113–1125, 2010.

[27] D. F. Welch, F. A. Kish, S. Melle, R. Nagarajan, M. Kato, C. H. Joyner, J. L. Pleumeekers, R. P. Schneider, J. Back, A. G. Dentai, *et al.*, "Large-scale inp photonic integrated circuits: Enabling efficient scaling of optical transport networks," *IEEE Journal of Selected Topics in Quantum Electronics*, vol. 13, no. 1, pp. 22–31, 2007.

[28] L. A. Coldren, S. W. Corzine, and M. L. Mashanovitch, *Diode lasers and photonic integrated circuits*, vol. 218. John Wiley & Sons, 2012.

[29] G. Gilardi and M. K. Smit, "Generic inp-based integration technology: Present and prospects (invited review)," *Progress In Electromagnetics Research*, vol. 147, pp. 23–35, 2014.

[30] M. Smit, X. Leijtens, H. Ambrosius, E. Bente, J. Van der Tol, B. Smalbrugge, T. De Vries, E.-J. Geluk, J. Bolk, R. Van Veldhoven, *et al.*, "An introduction to inp-based generic integration technology," *Semiconductor Science and Technology*, vol. 29, no. 8, p. 083001, 2014.

[31] P. E. Morrissey, N. Kelly, M. Dernaika, L. Caro, H. Yang, and F. H. Peters, "Coupled cavity single-mode laser based on regrowth-free integrated mmi reflectors," *IEEE Photonics Technol. Lett*, vol. 28, no. 12, pp. 1313–1316, 2016.

[32] D. Byrne, W. Guo, Q. Lu, and J. Donegan, "A tunable semiconductor lased based on etched slots suitable for monolithic integration," in *Advances in Optical and Photonic Devices*, InTech, 2010.

[33] J. Jin, L. Wang, T. Yu, Y. Wang, and J.-J. He, "Widely wavelength switchable v-coupled-cavity semiconductor laser with 40 db side-mode suppression ratio," *Optics letters*, vol. 36, no. 21, pp. 4230–4232, 2011.

[34] D. C. Byrne, J. P. Engelstaedter, W.-H. Guo, Q. Y. Lu, B. Corbett, B. Roycroft, J. O'Callaghan, F. Peters, and J. F. Donegan, "Discretely tunable semiconductor lasers suitable for photonic integration," *IEEE Journal of Selected Topics in Quantum Electronics*, vol. 15, no. 3, pp. 482–487, 2009.

[35] L. Wu, Z. Hu, X. Liao, and J.-J. He, "Half-wave-coupled ring-fp laser with 50-channel 100-ghz-spaced wavelength tuning," *IEEE Photonics Journal*, vol. 6, no. 4, pp. 1–8, 2014.

[36] M. Nawrocka, Q. Lu, W.-H. Guo, A. Abdullaev, F. Bello, J. O'Callaghan, T. Cathcart, and J. F. Donegan, "Widely tunable six-section semiconductor laser based on etched slots," *Optics express*, vol. 22, no. 16, pp. 18949–18957, 2014.

[37] P. Ramaswamy, B. Roycroft, J. OCallaghan, C. Janer, F. Peters, and B. Corbett, "Wavelength agile slotted fabry-pérot lasers," in

Semiconductor Laser Conference (ISLC), 2014 International, pp. 102–103, IEEE, 2014.

[38] L. Caro, M. Dernaika, N. P. Kelly, P. E. Morrissey, J. K. Alexander, and F. H. Peters, "An integration-friendly regrowth-free tunable laser," *IEEE Photonics Technology Letters*, vol. 30, no. 3, pp. 270–272, 2018.

[39] R. Phelan, B. Kelly, D. Jones, C. Herbert, J. O'Carroll, M. Rensing, B. Cai, A. Kaszubowska-Anandarajah, P. Perry, J. Stopford, *et al.*, "Discrete mode laser diodes with ultra narrow linewidth emission< 3khz," in *Optical Fiber Communication Conference*, p. OThK5, Optical Society of America, 2008.

[40] C. Guignard, J. Patchell, D. Jones, B. Kelly, L. P. Barry, P. Besnard, *et al.*, "Ultra-narrow (sub-mhz) linewidth emission from discrete mode laser diodes," in *The European Conference on Lasers and Electro-Optics*, p. CB12_2, Optical Society of America, 2007.

[41] Y. Wang, Y. Yang, S. Zhang, L. Wang, and J.-J. He, "Narrow linewidth single-mode slotted fabry–pérot laser using deep etched trenches," *IEEE Photonics Technology Letters*, vol. 24, no. 14, pp. 1233–1235, 2012.

[42] R. Lang, "Injection locking properties of a semiconductor laser," *IEEE Journal of Quantum Electronics*, vol. 18, no. 6, pp. 976–983, 1982.

[43] L. Thévenaz, S. Le Floch, D. Alasia, and J. Troger, "Novel schemes for optical signal generation using laser injection locking with application to brillouin sensing," *Measurement Science and Technology*, vol. 15, no. 8, p. 1519, 2004.

[44] J. Wang, M. Haldar, L. Li, and F. Mendis, "Enhancement of modulation bandwidth of laser diodes by injection locking," *IEEE Photonics Technology Letters*, vol. 8, no. 1, pp. 34–36, 1996.

[45] M. S. Taubman, T. L. Myers, B. D. Cannon, and R. M. Williams, "Stabilization, injection and control of quantum cascade lasers, and their application to chemical sensing in the infrared," *Spectrochimica Acta Part A: Molecular and Biomolecular Spectroscopy*, vol. 60, no. 14, pp. 3457–3468, 2004.

[46] W. Hung, C. K. Chan, L. K. Chen, and F. Tong, "An optical network unit for wdm access networks with downstream dpsk and upstream

re-modulated ook data using injection-locked fp laser," in *Optical Fiber Communication Conference*, p. TuR2, Optical Society of America, 2003.

[47] M.-C. Cheng, C.-T. Tsai, and G.-R. Lin, "Master-to-slave injection-locked wrc-fpld pair with 16 dwdm-pon channels for 16-qam ofdm transmission," in *Optical Fiber Communications Conference and Exhibition (OFC), 2014*, pp. 1–3, IEEE, 2014.

[48] M. Bachmann, P. A. Besse, and H. Melchior, "General self-imaging properties in n× n multimode interference couplers including phase relations," *Applied optics*, vol. 33, no. 18, pp. 3905–3911, 1994.

[49] W. Cotter, P. Morrissey, D. Goulding, B. Roycroft, Y. Hua, J. O'Callaghan, B. Corbett, and F. H. Peters, "Coherent comb generation using integrated slotted fabry-perot semiconductor lasers," in *Photonics Conference (IPC), 2012 IEEE*, pp. 848–849, IEEE, 2012.

[50] W. Cotter, D. Goulding, B. Roycroft, J. O'Callaghan, B. Corbett, and F. H. Peters, "Investigation of active filter using injection-locked slotted fabry–perot semiconductor laser," *Applied optics*, vol. 51, no. 30, pp. 7357–7361, 2012.

[51] N. P. Kelly, L. Caro, M. Dernaika, and F. H. Peters, "Regrowth-free integration of injection locked slotted laser with an electroabsorption modulator," *Optics Express*, vol. 25, no. 4, pp. 4054–4060, 2017.

[52] J. Zhao, K. Shi, Y. Yu, and L. P. Barry, "Theoretical analysis of tunable three-section slotted fabry–perot lasers based on time-domain traveling-wave model," *IEEE Journal of Selected Topics in Quantum Electronics*, vol. 19, no. 5, pp. 1–8, 2013.

[53] Q. Lu, W. Guo, R. Phelan, D. Byrne, J. Donegan, P. Lambkin, and B. Corbett, "Analysis of slot characteristics in slotted single-mode semiconductor lasers using the 2-d scattering matrix method," *IEEE photonics technology letters*, vol. 18, no. 24, pp. 2605–2607, 2006.

[54] B. Corbett, C. Percival, and P. Lambkin, "Multiwavelength array of single-frequency stabilized fabry-perot lasers," *IEEE journal of quantum electronics*, vol. 41, no. 4, pp. 490–494, 2005.

[55] R. Phelan, W.-H. Guo, Q. Lu, D. Byrne, B. Roycroft, P. Lambkin, B. Corbett, F. Smyth, L. P. Barry, B. Kelly, *et al.*, "A novel two-section tunable discrete mode fabry-perot laser exhibiting nanosecond

wavelength switching," *IEEE Journal of Quantum Electronics*, vol. 44, no. 4, pp. 331–337, 2008.

[56] N. Siwak, X. Fan, and R. Ghodssi, "Fabrication challenges for indium phosphide microsystems," *Journal of Micromechanics and Microengineering*, vol. 25, no. 4, p. 043001, 2015.

[57] D. Cuypers, S. De Gendt, S. Arnauts, K. Paulussen, and D. van Dorp, "Wet chemical etching of inp for cleaning applications i. an oxide formation/oxide dissolution model," *ECS Journal of Solid State Science and Technology*, vol. 2, no. 4, pp. P185–P189, 2013.

[58] J. J. Kelly and H. G. Philipsen, "Anisotropy in the wet-etching of semiconductors," *Current opinion in solid state and materials science*, vol. 9, no. 1-2, pp. 84–90, 2005.

[59] S. Adachi and H. Kawaguchi, "Chemical etching characteristics of (001) inp," *Journal of The Electrochemical Society*, vol. 128, no. 6, pp. 1342–1349, 1981.

[60] A. Stano, "Chemical etching characteristics of ingaas/inp and inalas/inp heterostructures," *Journal of the Electrochemical Society*, vol. 134, no. 2, pp. 448–452, 1987.

[61] H. Tsuchida, "Simple technique for improving the resolution of the delayed self-heterodyne method," *Optics letters*, vol. 15, no. 11, pp. 640–642, 1990.

[62] E. Kleijn, M. K. Smit, and X. J. Leijtens, "Multimode interference reflectors: a new class of components for photonic integrated circuits," *Journal of Lightwave Technology*, vol. 31, no. 18, pp. 3055–3063, 2013.

[63] N. P. Kelly, M. Dernaika, L. Caro, P. E. Morrissey, A. H. Perrott, J. K. Alexander, and F. H. Peters, "Regrowth-free single mode laser based on dual port multimode interference reflector," *IEEE Photonics Technology Letters*, vol. 29, no. 3, pp. 279–282, 2017.

[64] D. G. Rabus, M. Hamacher, U. Troppenz, and H. Heidrich, "Optical filters based on ring resonators with integrated semiconductor optical amplifiers in gainasp-inp," *IEEE Journal of Selected Topics in Quantum Electronics*, vol. 8, no. 6, pp. 1405–1411, 2002.

[65] M. Hamacher, U. Troppenz, H. Heidrich, and D. G. Rabus, "Active ring resonators based on gainasp/inp," in *Laser Diodes, Optoelectronic Devices, and Heterogenous Integration*, vol. 4947, pp. 212–223, International Society for Optics and Photonics, 2003.

[66] D. G. Rabus and M. Hamacher, "Mmi-coupled ring resonators in gainasp-inp," *IEEE Photonics Technology Letters*, vol. 13, no. 8, pp. 812–814, 2001.

[67] S. Xie, J. Guo, K. Guan, L. Mao, W. Guo, L. Qi, and X. Li, "Design and realization of inp/algainas multiple quantum well ring laser," *Transactions of Tianjin University*, vol. 20, no. 6, pp. 402–406, 2014.

[68] G. Griffel, J. H. Abeles, R. J. Menna, A. M. Braun, J. C. Connolly, and M. King, "Low-threshold ingaasp ring lasers fabricated using bi-level dry etching," *IEEE Photonics Technology Letters*, vol. 12, no. 2, pp. 146–148, 2000.

[69] M. Sorel, G. Giuliani, A. Scire, R. Miglierina, S. Donati, and P. Laybourn, "Operating regimes of gaas-algaas semiconductor ring lasers: experiment and model," *IEEE Journal of Quantum Electronics*, vol. 39, no. 10, pp. 1187–1195, 2003.

[70] S. Furst, S. Yu, and M. Sorel, "Fast and digitally wavelength-tunable semiconductor ring laser using a monolithically integrated distributed bragg reflector," *IEEE Photon. Technol. Lett*, vol. 20, no. 23, pp. 1926–1928, 2008.

[71] D. G. Rabus, Z. Bian, and A. Shakouri, "Ring resonator lasers using passive waveguides and integrated semiconductor optical amplifiers," *IEEE Journal of Selected Topics in Quantum Electronics*, vol. 13, no. 5, pp. 1249–1256, 2007.

[72] R. Grover, T. A. Ibrahim, L.-C. Kuo, T.-N. Ding, S. Kanakaraju, L. C. Calhoun, and P.-T. Ho, "Ultracompact single-mode gainasp-inp microracetrack resonators," in *Integrated Photonics Research*, p. ITuE5, Optical Society of America, 2003.

[73] P. Bienstman, E. Six, A. Roelens, M. Vanwolleghem, and R. Baets, "Calculation of bending losses in dielectric waveguides using eigenmode expansion and perfectly matched layers," *IEEE Photonics technology letters*, vol. 14, no. 2, pp. 164–166, 2002.

[74] R. N. Sheehan, S. Horne, and F. H. Peters, "The design of low-loss curved waveguides," *Optical and quantum electronics*, vol. 40, no. 14-15, pp. 1211–1218, 2008.

[75] R. N. Sheehan and F. H. Peters, "Bends in the plane with variable curvature," 2016.

[76] J.-J. He and D. Liu, "Wavelength switchable semiconductor laser using half-wave v-coupled cavities," *Optics express*, vol. 16, no. 6, pp. 3896–3911, 2008.

[77] M. W. Pruessner, K. Amarnath, M. Datta, D. P. Kelly, S. Kanakaraju, P.-T. Ho, and R. Ghodssi, "Inp-based optical waveguide mems switches with evanescent coupling mechanism," *Journal of Microelectromechanical Systems*, vol. 14, no. 5, pp. 1070–1081, 2005.

[78] M. Barnoski, *Introduction to integrated optics*. Springer Science & Business Media, 2012.

[79] M. L. Gorodetsky, A. A. Savchenkov, and V. S. Ilchenko, "Ultimate q of optical microsphere resonators," *Optics letters*, vol. 21, no. 7, pp. 453–455, 1996.

[80] D. Hofstetter and R. L. Thornton, "Measurement of the q factor of semiconductor laser cavities by fourier analysis of the emission spectrum," in *Fabrication, Testing, Reliability, and Applications of Semiconductor Lasers III*, vol. 3285, pp. 66–78, International Society for Optics and Photonics, 1998.

[81] D. Hillerkuss, R. Schmogrow, T. Schellinger, M. Jordan, M. Winter, G. Huber, T. Vallaitis, R. Bonk, P. Kleinow, F. Frey, *et al.*, "26 tbit s- 1 line-rate super-channel transmission utilizing all-optical fast fourier transform processing," *Nature photonics*, vol. 5, no. 6, p. 364, 2011.

[82] J. Pfeifle, M. Lauermann, D. Wegner, V. Brasch, T. Herr, K. Hartinger, J. Li, D. Hillerkuss, R. Schmogrow, R. Holzwarth, *et al.*, "Coherent data transmission with microresonator kerr frequency combs," *arXiv preprint ArXiv:1307.1037*, 2013.

[83] C. Weimann, P. Schindler, R. Palmer, S. Wolf, D. Bekele, D. Korn, J. Pfeifle, S. Koeber, R. Schmogrow, L. Alloatti, *et al.*, "Silicon-organic hybrid (soh) frequency comb sources for terabit/s data transmission," *Optics express*, vol. 22, no. 3, pp. 3629–3637, 2014.

[84] M. Mazur, A. Lorences-Riesgo, J. Schroeder, P. Andrekson, and M. Karlsson, "10 tb/s pm-64qam self-homodyne comb-based superchannel transmission with 4% shared pilot tone overhead," *Journal of Lightwave Technology*, 2018.

[85] V. Ataie, E. Temprana, L. Liu, E. Myslivets, B. P.-P. Kuo, N. Alic, and S. Radic, "Ultrahigh count coherent wdm channels transmission using optical parametric comb-based frequency synthesizer," *Journal of Lightwave Technology*, vol. 33, no. 3, pp. 694–699, 2015.

[86] J. Pfeifle, V. Vujicic, R. T. Watts, P. C. Schindler, C. Weimann, R. Zhou, W. Freude, L. P. Barry, and C. Koos, "Flexible terabit/s nyquist-wdm super-channels using a gain-switched comb source," *Optics express*, vol. 23, no. 2, pp. 724–738, 2015.

[87] O. Gerstel, M. Jinno, A. Lord, and S. B. Yoo, "Elastic optical networking: A new dawn for the optical layer?," *IEEE Communications Magazine*, vol. 50, no. 2, 2012.

[88] M. D. G. Pascual, R. Zhou, F. Smyth, P. M. Anandarajah, and L. P. Barry, "Software reconfigurable highly flexible gain switched optical frequency comb source," *Optics express*, vol. 23, no. 18, pp. 23225–23235, 2015.

[89] L. Caro, N. P. Kelly, M. Dernaika, M. Shayesteh, P. E. Morrissey, J. K. Alexander, and F. H. Peters, "A facetless regrowth-free single mode laser based on mmi couplers," *Optics & Laser Technology*, vol. 94, pp. 159–164, 2017.

[90] L. Wu, Y. Wang, T. Yu, L. Wang, and J.-J. He, "Wavelength switchable semiconductor laser based on half-wave coupled fabry–pérot and rectangular ring resonators," *IEEE Photonics Technology Letters*, vol. 24, no. 12, pp. 991–993, 2012.